Title
Multidimensional Ultrafast Spectroscopy of Photosynthetic Pigment-Protein Complexes

Author
De Re, Eleonora

Publication Date
2014

Peer reviewed|Thesis/dissertation

Multidimensional Ultrafast Spectroscopy of Photosynthetic Pigment-Protein Complexes

by

Eleonora De Re

A dissertation submitted in partial satisfaction of the
requirements for the degree of

Doctor of Philosophy

in

Applied Science & Technology

in the

Graduate Division

of the

University of California, Berkeley

Committee in charge:

Professor Graham R. Fleming, Chair
Professor Krishna K. Niyogi
Professor David T. Attwood

Spring 2014

Multidimensional Ultrafast Spectroscopy of Photosynthetic Pigment-Protein Complexes

Abstract

Multidimensional Ultrafast Spectroscopy of Photosynthetic Pigment-Protein Complexes

by

Eleonora De Re

Doctor of Philosophy in Applied Science & Technology

University of California, Berkeley

Professor Graham R. Fleming, Chair

This dissertation presents the application of ultrafast spectroscopy to the investigation of pigment-protein complexes (PPCs) involved in energy transfer and energy dissipation in photosynthetic organisms. PPCs are the building blocks of all photosynthetic organisms, and within individual pigment-protein complexes, energy transfer dynamics occur over fast timescales and broad spectral regions. Chapter 1 gives an introduction to the capability of photosynthetic organisms to absorb light energy, funnel this energy to a location for charge separation, and perform charge separation with subsequent conversion into chemical energy. All of these functions need to be performed efficiently under different light conditions. This chapter also includes a discussion of the different light harvesting strategies that various photosynthetic organisms have evolved. Lastly, this chapter discusses the application of ultrafast spectroscopy as an excellent tool to study the dynamics of PPCs. The three experimental techniques used in this dissertation are introduced in this chapter.

Chapters 2 and 3 present the application of two ultrafast spectroscopic techniques, two dimensional electronic spectroscopy and transient absorption spectroscopy, to the investigation of the structure-function relationship of photosynthetic pigment-protein complexes. Chapter 2 is an investigation of the photophysics of the two forms of the Orange Carotenoid Protein, involved in excess energy dissipation in cyanobacteria. Ultrafast spectroscopy allows us to understand how a conformational change that modifies pigment-protein interactions is able to generate a different biological function. Chapter 3 presents degenerate and non-degenerate two dimensional electronic spectroscopy experiments to investigate the energy transfer dynamics and couplings in the bacterial reaction center, which is the location of charge separation.

Chapter 4 investigates a PPC involved in excess energy dissipation in green algae, LhcSR. Fluorescence lifetime spectroscopy is used to investigate the excited state properties of LhcSR, which plays a role as light harvester, pH sensor and quencher in algae. The results allow us to identify two conformations, a light harvesting one and a quenching one. Transient absorption spectroscopy is used to investigate the energy transfer pathways involved in quenching in the two different conformations. Finally, Chapter 5 presents conclusions and extensions to future work, in order to improve our understanding of the energy transfer dynamics in natural photosynthetic systems.

To my parents

Acknowledgements

There are many people that I am indebted to for their support throughout these five years. I would like to acknowledge first my advisor, Professor Graham Fleming, for inspiring me to take a big picture approach to science, and not start with the small details, and for valuing the importance of scientific independence and self-assessment. These are skills and values which will always accompany me in my future career. A sincere thank you goes to my collaborators over the years, for the stimulating scientific discussions and the great samples that they have prepared for me. I am grateful for funding from the Department of Energy.

One of the best things about grad school is the amazing people that you get to meet. I have had the fortune to not only meet inspiring coworkers, but a few people that I am lucky enough to call friends. A special thank you goes to Julia Zaks, who was the first person to be there for me, with wise words and encouragement, and true friendship. To Gabriela Schlau-Cohen, who has been a terrific mentor, lab partner, and friend. And to Emily Jane Sylak-Glassman, who has been my grad school companion for these past five years, and who has always had a smile and an encouragement for me even outside of work. A big thank you goes to all the Flemingos that have been great coworkers and work friends over these past years. I cannot list everyone, as in five years I've had the luck to overlap with a lot of amazing people, but I have learnt something from each one of them.

A thank you goes to my non-grad school friends. No matter how geographically far they have been, they have believed in me and motivated me to believe in myself, and have been present for me when I needed them.

None of this would have been possible without the constant support that my parents have given me. This thesis is dedicated to them, as a thank you for always encouraging me to do what I love and to believe in myself. Niente di tutto ciò sarebbe stato possible senza il costante supporto, morale ed emotivo, dei miei genitori, che nonostante la lontananza geografica sono sempre stati i primi ad essere presenti, per consolare e per celebrare. Questa tesi e' dedicata a loro, come ringraziamento per il loro costante incoraggiamento a fare quel che amo e a credere in me stessa.

Contents

Chapter 1

Introduction

Contents

Photosynthesis starts with the absorption of solar radiation, followed by conversion of the corresponding light energy into chemical energy used for production of biomass. This conversion is essential for survival of the photosynthetic organisms, and needs to be performed with high efficiency under a variety of light conditions. Light absorption occurs in the peripheral antenna complexes and excitation energy is transferred to a central location, the reaction center, where a charge separation event occurs, producing chemical energy (see Fig. 1.1). This chemical energy drives downstream photochemistry and eventually production of biomass.

In order to perform this energy conversion efficiently under different light conditions, all photosynthetic organisms need to regulate the light that reaches the reaction center. A variety of mechanisms contribute to this regulation, collectively known under the word photoprotection. One type of photoprotection mechanism is the de-excitation of singlet excited states in antenna complexes, known as non photochemical quenching (NPQ) [1, 2]. NPQ is comprised of a variety of processes happening on a large range of timescales, from femtoseconds up to seconds and minutes. In this thesis, I will focus on NPQ processes that turn on and off rapidly, referred to in the literature as 'flexible NPQ' [2]. Different photosynthetic organisms possess

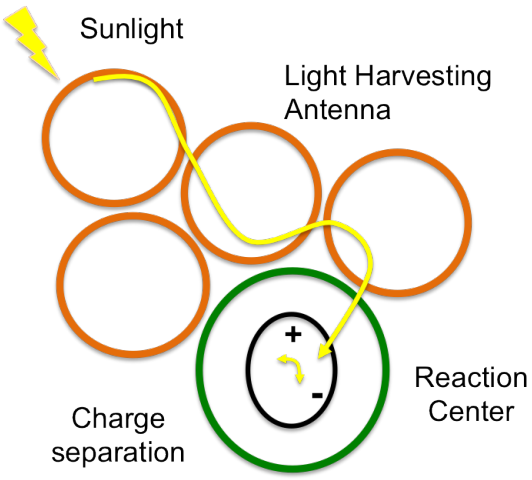

Figure 1.1: Schematic of a generic photosynthetic apparatus, highlighting absorption of sunlight in the antenna complex (orange and green circles), transfer of energy through the antenna to the reaction center (black oval), location of charge separation.

different light harvesting systems, and therefore have evolved different ways of rapidly dissipating excess excitation energy. Section 1.2 will describe different photoprotection strategies in more detail.

Our aim is to understand the governing principles underlying natural photosynthesis in order to apply them to, for example:

- Engineer better artificial devices
- Improve crop yields, for example increasing their adaptability to adverse environments
- Envision better biofuel feedstocks that rely on natural photosynthesis

1.1 Pigment Protein Complexes

Light absorption, energy transfer of the absorbed energy and charge separation events are carried out by specialized proteins, Pigment-Protein Complexes (PPCs). PPCs are collections of pigments held together by a protein matrix such as to produce a specific function. Many PPCs are transmembrane proteins, embedded in a membrane known as the thylakoid membrane. 80% of the thylakoid is occupied by PPCs [3], which are organized in specific complexes (photosystems) to carry out their functions of energy collection and translocation to the reaction center, a PPC itself. Non-transmembrane PPCs are also found playing important roles in photosynthetic systems (i.e. the cyanobacterial PPC we will talk about in Chapter 2).

The properties of PPCs are not just the sum of their components. The particular arrangement of the pigments (distances, interactions between the pigments, relative orientation) and their interactions with the protein matrix determines their specific function. PPCs are densely

packed, with dimensions of a few nm. This dense packing causes strong electrostatic interactions which alter the energetic properties of the PPC from the linear sum of those of their components, tuning them to produce broad absorption spectra and ultrafast energy transfer.

1.1.1 Chlorophylls and carotenoids

Pigments are the components responsible for light absorption, therefore are fundamental for the functioning of all photosynthetic systems. The most common pigments found in PPCs are chlorophylls and carotenoids. Here we will give a brief overview of their main spectroscopic properties to ease the interpretation of the experimental results in the subsequent chapters.

Chlorophylls (Chls) are the most abundant light-harvesting pigments found in nature. They are responsible for the green coloring of plants, as their main absorption lies in the red (around 660 nm) (see Fig. 1.2) [4]. A structural variant of Chls are Bacteriochlorophylls (BChl), found in anoxygenic bacterial systems. We will encounter BChls when we discuss the bacterial reaction center in Chapter 3. The transitions observed in the absorption spectra are HOMO $\rightarrow$ LUMO transitions. In our measurements, we will be mostly investigating the Q_x and Q_y transitions of Chl *a* or BChl.

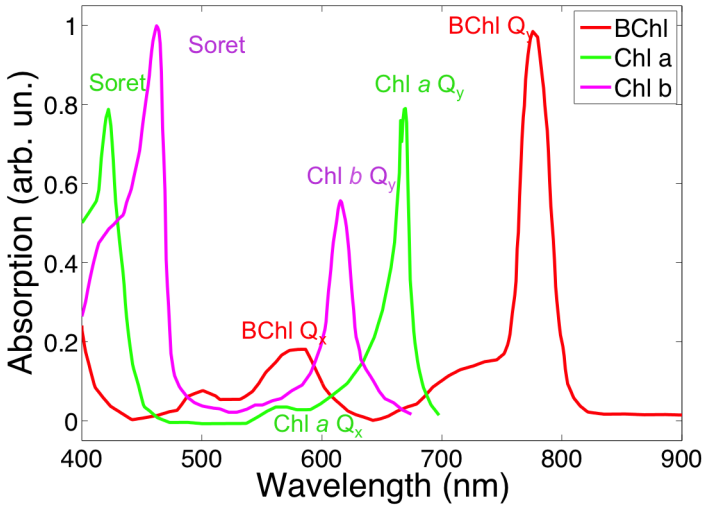

Figure 1.2: Linear absorption spectrum of Chl *a*, Chl *b* and BChl. The main transitions are labeled and described in the text.

Carotenoids play a critical role in photosynthesis [5, 6]. In particular, they have a role in light harvesting, having absorption spectra complementary to that of chlorophylls, thus increasing the effective utilization of the solar spectrum by photosynthetic systems. They play an important structural role, since they are often bound with chlorophylls to light-harvesting PPCs. They are also necessary in photoprotection, by quenching Chl triplets and singlet oxygen and by safely dissipating excess absorbed energy as heat.

Carotenoids are linear conjugated polyenes, whose photophysical properties are governed by the C_{2h}-like symmetry of their conjugated chain (Fig. 1.3 (a) shows the structure

of the carotenoid zeaxanthin, which plays an important role in photoprotection in plants) [6]. Despite decades of theoretical and experimental work, the precise electronic structure of carotenoids remains elusive. Their basic electronic structure derives from their C_{2h} point group symmetry (refer to Fig. 1.3 (c)). Their ground state, commonly referred to as S_0, is of Ag^- symmetry. The first excited state, S_1, is of the same symmetry ($2Ag^-$), therefore the transition between the ground state and the first excited state is optically forbidden. The second excited state S_2 is of $1Bu^+$ symmetry, and the transition between S_0 and S_2 is strongly optically allowed; the linear absorption spectrum of carotenoids is typically dominated by this transition, which has a maximum in the region 400 - 500 nm, depending on the length of the conjugated chain (Fig. 1.3 (b) reports the linear absorption spectrum of zeaxanthin). Upon excitation of the $S_0 \rightarrow S_2$ transition, the population relaxes quickly to S_1, on a timescale of less than a few hundred femtoseconds. S_1 then relaxes to the ground state on a 10 - 100 ps timescale [6]. It is important to notice that the energy of the electronic states and their lifetime are highly dependent on the structure of the carotenoid itself (length of the conjugated chain and end groups) and on its interactions with the environment (solvent or protein).

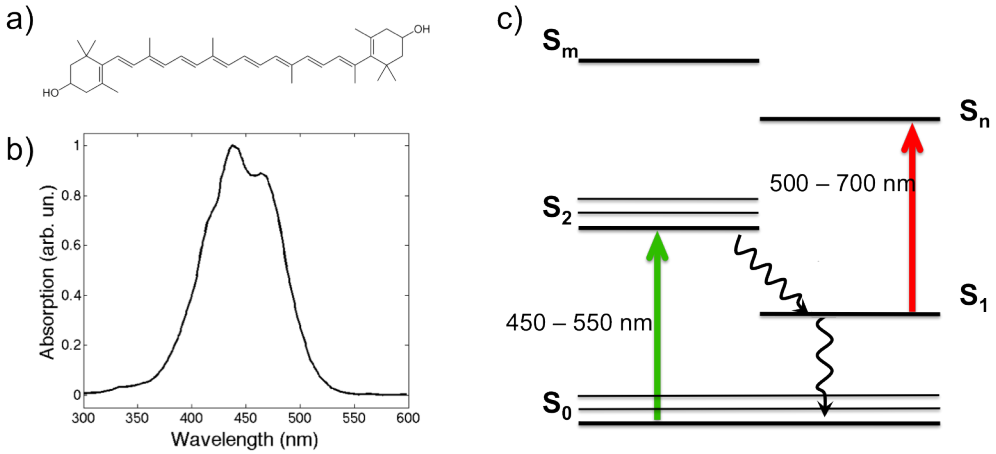

Figure 1.3: (a) Structure of the carotenoid zeaxanthin, which plays an important role in photoprotection (see text). (b) Linear absorption spectrum of zeaxanthin. (c) General energy level structure of carotenoids.

1.2 Photoprotection mechanisms

All photosynthetic organisms need to be able to regulate the amount of light absorbed in order to efficiently perform photosynthesis under a variety of light conditions [7, 8, 9]. Light available to the organism in fact changes vastly and rapidly in time and space due to season, time of day, weather, shading by clouds and other effects. The light response curve in Fig. 1.4 shows the amount of energy assimilated versus light intensity. At low light intensities, typical of a cloudy day (200 μmol photons/m^{2}s), all the light is used for productive photosynthesis (CO_2 assimilation). As light intensity increases, the rate of photosynthesis increases until

saturation. On a sunny day (2000 μmol photons/m^{2}s) the amount of excess energy can be far greater than the energy productively used.

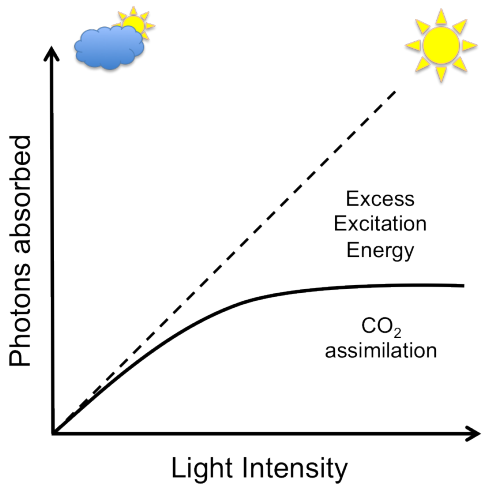

Figure 1.4: Model curve showing the amount of absorbed energy used for productive photosynthesis (CO_2 assimilation versus excess excitation energy). As the light intensity increases, the amount of photons that can be used for productive photosynthesis saturates and the amount of excess energy increases.

Photosynthetic systems need to be able to maximize the energy sent to the reaction center in low light conditions and dissipate excess energy in high light conditions. In case of excess energy absorption, in fact, light energy can induce the generation of reactive oxygen species (ROS) that can be damaging for the organism.

In order to prevent photooxidative damage, photosynthetic organisms have evolved a series of mechanisms to safely dissipate excess energy, collectively known as *photoprotection*. Different photosynthetic organisms have evolved different mechanisms to cope with the diversity in environmental conditions, in availability of light in terms of intensity and spectral quality, in light harvesting apparatuses. Long-term photoprotection mechanisms (photoacclimation) involve changes to the composition of the photosynthetic system, with degradation and de-novo synthesis of parts of the photosynthetic apparatus [10]. Short-term mechanisms involve fast and reversible modifications of the photosynthetic apparatus. One subset of these short-term photoprotection mechanisms is Non Photochemical Quenching (NPQ) of chlorophyll fluorescence, which corresponds to the de-excitation of singlet excited PPCs. If singlet-excited PPCs are not rapidly quenched, they can decay to Chlorophyll triplet states, which can interact with oxygen to form singlet oxygen, potentially damaging for the photosynthetic proteins [11, 12]. Our interest will be on the rapidly turning on and off components of NPQ ('flexible NPQ') [2].

Cyanobacteria were the first oxygenic photosynthetic organisms to evolve $\sim$3 billion years ago. The main light-harvesting antenna of cyanobacteria (see also Fig. 2.1) is the phycobilisome, which exhibits NPQ responses to blue-green light absorption. Chapter 2 will be devoted to the description of an NPQ mechanism in cyanobacteria, which involves the Orange Carotenoid Protein (OCP), a single carotenoid-binding PPC. As will be described in

detail in Section 2.2, upon excess light absorption, OCP undergoes a conformational change to an active form, which binds to the phycobilisome antenna and dissipates excess energy safely as heat.

Upon endosymbiosis, cyanobacteria have evolved, leading to the diversification of red algae, green algae and plants. During evolution, the light harvesting systems have largely diversified to adapt to the particular environment of the organism. This diversification of light-harvesting systems has led to the diversification of NPQ mechanisms, with the acquisition and the specific loss of genes encoding for PPCs (see Fig. 1.5) [13].

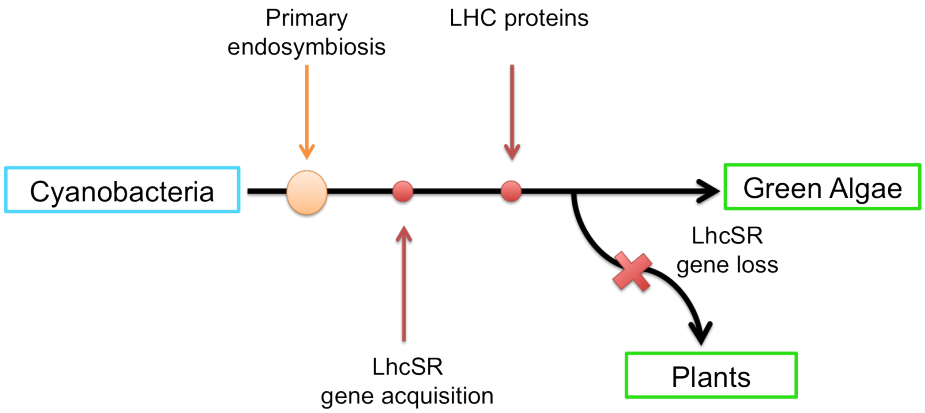

Figure 1.5: Evolution from cyanobacteria to green algae and plants. The primary endosymbiosis is the evolutionary event in which plants and algae acquired photosynthetic capabilities from cyanobacteria, which evolved into chloroplasts. Acquisition and loss of specific genes is also highlighted.

A vast research effort has been devoted to the investigation of NPQ in plants, yet the mechanisms that are triggered by excess light absorption, the trigger itself and the components playing a role in energy dissipation have not been fully elucidated yet. NPQ in plants requires the buildup of a ΔpH across the thylakoid membrane, and the presence of specific carotenoids (conversion of violaxanthin into zeaxanthin occurs in the so-called 'xanthophyll cycle' [14, 15, 16]). Also, a four-helix membrane protein, PsbS, has been shown to play a very important role in NPQ [17]. The precise molecular mechanisms of NPQ in plants remain elusive, but the current hypothesis is that excess light absorption leads to a buildup of ΔpH across the thylakoid membrane. This ΔpH is sensed by PsbS, which presumably promotes a rearrangement in the membrane and the induction of a quenched state. Quenching occurs in PPCs in the antenna system; however, the exact location and molecular mechanism of energy dissipation is still under debate [18] (see also Section 1.3).

The photosynthetic apparatus of green algae is similar to that of plants. The main antenna system in algae is composed of three-helix membrane PPCs and flexible NPQ is triggered by the buildup of a ΔpH across the thylakoid membrane and by the presence of the xanthophyll zeaxanthin. It has been recently discovered that a specific PPC, LhcSR, is essential for flexible NPQ in algae [19]. LhcSR from *Chlamidomonas reinhardtii* has been shown to be able to perform two functions: 1) it senses the change in pH thanks to lumen-exposed protonatable residues; and 2) is capable of quenching chlorophyll fluorescence [20]. Chapter 4

will present spectroscopic results obtained on LhcSR, investigating its quenching capabilities under different environmental conditions. A comparison with a mutant on its protonatable sites will be also presented.

Other photoprotective mechanisms, different from NPQ, have evolved at the level of the individual PPC, as alternative energy pathways that become available under high light intensities. Chapter 3 will be devoted to the investigation of the energy transfer dynamics in the reaction center from purple bacteria. Investigating the reaction center in its oxidized state gives information about the energy transfer pathways available in the case of a closed reaction center (not capable of performing any more charge separation events). These pathways are therefore important in high light conditions.

1.3 The interplay between carotenoids and chlorophylls in photosynthesis

It is well accepted that Cars and Chls play fundamental roles in photosynthesis, both in light harvesting and in photoprotection. What remains to be elucidated is the exact nature of the interactions/interplay between Cars and Chls and how the change in their interaction is related to the larger scale switch of photosynthetic systems between efficient light harvesting and efficient and safe excess energy dissipation.

Cars and Chls play an essential role in light harvesting by absorbing the solar energy and ensuring efficient funneling of the excitation energy to the reaction center and in the reaction center itself. In particular, Cars absorb solar radiation in a spectral region complementary to that of Chls. Upon absorption of light, they are able to transfer excitation energy efficiently to the Chls. These energy transfer pathways have been observed in a variety of photosynthetic systems (for example, see [21, 22, 23] for LHCII, [24] for LH1, [25] for LH2). Generally, two main pathways for Car $\rightarrow$ Chl energy transfer are: 1) transfer via the S_2 state of Car to the Q_x state of Chls, which then relaxes to their Q_y state in a few hundred fs; 2) energy transfer from the S_1 state of Cars directly to the Q_y state of Chl. Other pathways which involve transfer through intermediate carotenoid states have been proposed in LH1 and LH2 [24, 25].

Additionally, the interplay between Cars and Chls is fundamental in photoprotection. For example, Cars are known to be very efficient in quenching the triplet states of Chls (which can form upon excess light absorption) directly via triplet-triplet energy transfer, and to quench singlet oxygen (formed by interaction of ground state oxygen and Chl triplet states) by accepting energy in their triplet state [26]. However, other mechanisms of energy dissipation that are rate-competitive with Chl triplet formation exist. The idea at the basis of all of these mechanisms is fast energy or charge transfer to a lower lying state that decays quickly to the ground state dissipating energy as heat. Many mechanisms have been proposed to contribute to flexible NPQ (qE) in higher plants, and it is thought that similar dissipation processes could take place in other photosynthetic organisms as well, such as algae. The main hypotheses in the literature are:

- Formation of a carotenoid cation and a chlorophyll radical anion (upon forming of a

Car-Chl heterodimer) has been proposed on the basis of transient absorption experiments on intact thylakoids and isolated minor complexes from plants. Upon excitation of the Chl *a* Q_y transition (670 nm), a signal appears at either 980 nm (Zeaxanthin) or at 940 nm (Lutein) in both intact thylakoid membranes and isolated minor antenna complexes [27, 28, 29].

- Energy transfer from Chl to the Car S_1 state has been proposed by [30, 31].
- Formation of excitonic states between Chl and Car [32, 33, 34, 35, 36]. This hypothesis has been proposed on the basis of two sets of experiments: 1) transient absorption has measured an instantaneous population of the Car S_1 state upon excitation of Chl [34], with a signature at $\sim$ 540 nm, showing Chl $\rightarrow$ Car transfer; 2) selective Car S_1 two photon excitation and probing of the Chl fluorescence has indicated energy transfer Car $\rightarrow$ Chl. Therefore, upon NPQ induction, bidirectional energy transfer between Car and Chl is observed, which could be explained by excitonic interactions [33].
- Formation of Chl-Chl excitonic interactions both *in vivo* and in LHCII aggregates, with energy transfer to a far-red emitting charge transfer state, has been proposed in [37, 38]. This hypothesis excludes any involvement of carotenoids.

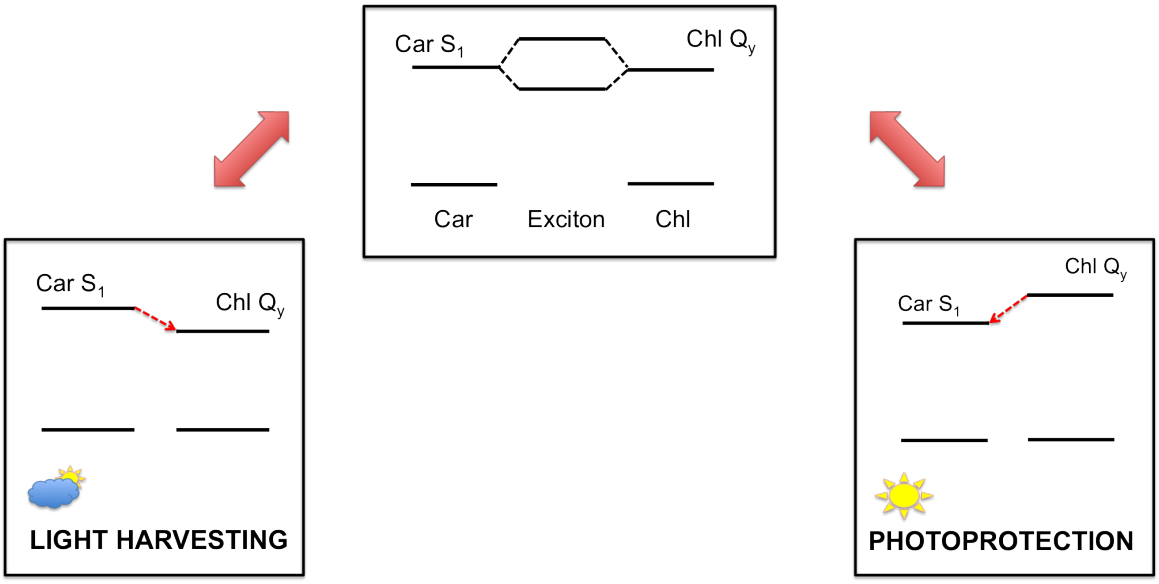

Figure 1.6: The fluctuations in energies and couplings of Cars and Chl determine the direction of energy flow. Excitonic interaction between the Car S_1 state and the Chl Q_y state give rise to two new energy levels, one lower and one higher in energy than the original states. In light-harvesting conditions, energy transfer is preferentially from the Car to the Chl, in photoprotection conditions the flow is reversed.

Holleboom and Walla [36] have recently proposed a model that unifies these experimental observations. This model assumes that Cars are playing a fundamental role both in light harvesting and in photoprotection. A Car and a Chl form an excitonic interaction (see Fig. 1.6),

for which the lower lying excitonic state is energetically favorable as a trap for excitation energy and has a lifetime intermediate between the long Chl Q_y excited state lifetime (3.5 ns in LHCII [39]) and the short Car S_1 lifetime (a few tens of ps). Since the excitonic interaction depends on the relative energy of the states and on their coupling strength, thermal fluctuations in these parameters need to be taken into account. Excitonic mixing would then be an intermediate state between a case in which the lower lying state has more Car character (thus promoting Chl $\rightarrow$ Car energy transfer) and one in which it has more Chl character (promoting Car $\rightarrow$ Chl energy transfer). How and why the equilibrium is shifted preferentially in one direction or the other for light harvesting and photoprotection, respectively, still needs to be elucidated. However, this model reconciles many experimental observations, under the assumption that a variety of dissipative mechanisms can take place with different yields depending on the particular system fluctuations. It explains the observation of Forster-like energy transfer in both directions [31], and of an increased energy transfer in either direction upon induction of NPQ [33]. The excitonic state formation explains the instantaneous population of Car states upon Chl excitation in [40, 34]. The excitonic mixing could be also a precursor for a charge transfer state involved in charge transfer between a Car and a Chl [41, 42, 27]. Also, an excitonic lower lying state would explain as well the observed red shift in absorption [33] and fluorescence [43].

1.4 Ultrafast Spectroscopy Techniques

The processes of energy transfer inter- and intra- PPCs and energy dissipation described so far occur on ultrafast timescales. Energy moves inside individual PPCs on a femtosecond timescale, and the overall transfer of excitation from the periphery of the antenna system to the reaction center takes $\sim$ 200 ps [44]. Moreover, as discussed in Section 1.1, for maximal absorption of the solar spectrum, evolution has optimized PPCs to absorb over a wide range of wavelengths in the visible region of the spectrum. In order to investigate processes occurring on such fast timescales and over such broad bandwidths, we need experimental tools that offer both temporal and spectral resolution.

In this section, I will present three experimental techniques that I have used in this thesis work for studying energy transfer and quenching dynamics in photosynthetic pigment protein complexes. Further experimental details for the specific systems under investigation can be found in the corresponding Chapters.

1.4.1 Two Dimensional Electronic Spectroscopy

Two dimensional (2D) electronic spectroscopy is a four-wave mixing technique which aims at retrieving the full third-order nonlinear response of a material. Three ultrashort laser pulses interact with the material under investigation, and induce the emission of a signal. The temporal ordering of these three pulses in shown in Figure 1.7, and the electric field associated with each pulse is given by

$$E_j(t) = \tilde{A}_j(t)[e^{-i(\omega_0 t + \vec{k_j}\cdot\vec{r})} + e^{i(\omega_0 t - \vec{k_j}\cdot\vec{r})}] \quad (1.4.1.1)$$

where $j = 1, 2, 3$, ω_0 is the central laser frequency, $\tilde{\text{A}}(\text{t}) = \text{A(t)}\exp(-i\varphi(t))$ is the complex envelope, with a Gaussian profile $\text{A(t)} = \exp(-2\ln 2\,(t/\tau_P)^2)$ of full width half maximum corresponding to the pulse duration τ_P and phase $\varphi(t)$ [45].

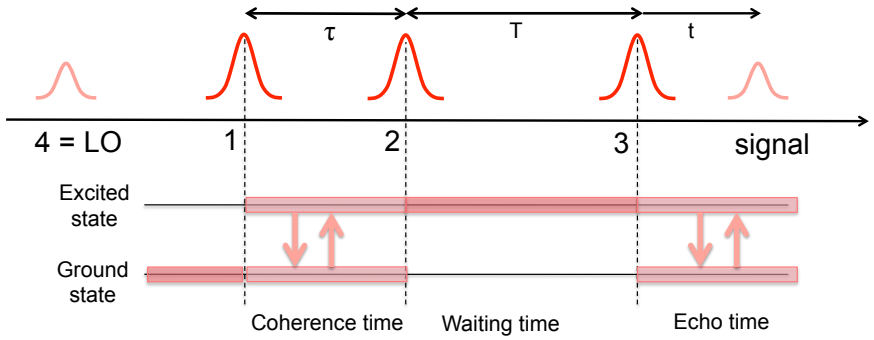

Figure 1.7: Time-ordering of the interactions of the three laser pulses, and emission of the signal *(top)*. Representative time evolution of the density matrix for a two level system after interaction with the laser pulses *(bottom)*.

Referring to Figure 1.7, let us assume for simplicity a 2 level system. When pulse 1 interacts with the sample, its oscillating electric field induces an oscillation of the transition dipoles of the molecules in the system, corresponding to the coherence $|g\rangle\langle e|$. The frequency of this oscillating coherence, ω_{eg}, is proportional to the energy gap between the excited and the ground state. This oscillation evolves during the time τ (known as *coherence time*) between pulses 1 and 2. When the second pulse arrives, it pushes the system into a population state, and we can follow its evolution during the *waiting time* T between pulses 2 and 3. The arrival of pulse 3 induces another oscillation in the transition dipoles of the sample, at a frequency ω_{ge}. The interaction with the three pulses produces a macroscopic third order polarization in the system, given by

$$P^{(3)}(t) = \int_0^\infty\int_0^\infty\int_0^\infty S^{(3)}(t_1,t_2,t_3)\,E_3(t-t_3)\,E_2(t-t_3-t_2)\,E_1(t-t_3-t_2-t_1)\,dt_1\,dt_2\,dt_3, \quad (1.4.1.2)$$

where $S^{(3)}(t_1,t_2,t_3)$ is the third order response function of the system (the third order polarization in case of applied impulsive electric fields) and E_j, where j = 1,2,3, is as in equation (1.4.1.1).

The polarization is source for the signal field, emitted at time *t* (*echo time*). The signal is recorded experimentally as a function of the conjugate frequency ω_t:

$$E_s(\tau,T,\omega_t) \sim \frac{i\omega_t}{n(\omega_t)}P^{(3)}(\tau,T,\omega_t). \quad (1.4.1.3)$$

The 2D correlation spectrum is eventually obtained upon Fourier transforming along the coherence time axis:

$$S_{2D}(\omega_\tau, T, \omega_t) = \int_{-\infty}^{\infty} iP^{(3)}(\tau, T, \omega_t) e^{i\omega_\tau \tau}\, d\tau. \tag{1.4.1.4}$$

The 2D spectrum represents a correlation in the frequency domain between excitation and emission energies. Figure 1.8 shows a sample 2D spectrum. The peaks along the diagonal correspond to transitions for which excitation energy and emission energy are the same, thus they contain the information encoded in linear absorption (also shown on top of the spectrum). Cross-peaks correspond to transitions for which excitation energy and emission energy are different, so they carry information about energy transfer processes and couplings in the system. Positive peaks correspond to bleach and stimulated emission processes, while negative peaks correspond to excited state absorption transitions.

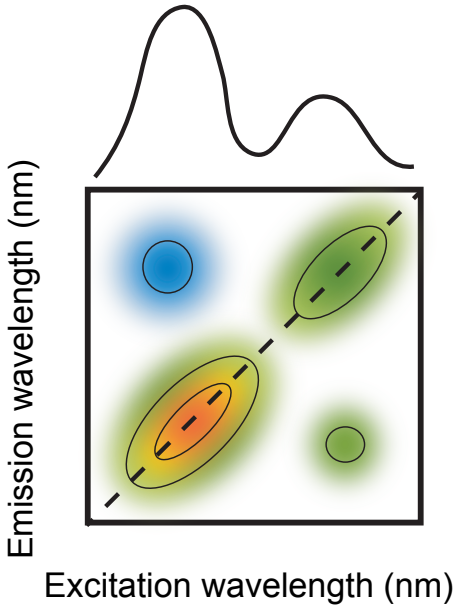

Figure 1.8: Sample 2D spectrum. Positive peaks are shown in green and red, negative peaks in blue. On top, the corresponding linear absorption spectrum is reported.

Experimental apparatus

Various implementations of 2D spectroscopy have been presented in recent years with varying time-ordering of the pulses, geometries and methods of delay introduction [46, 45, 47, 48]. Here I will review the experimental apparatus used to perform degenerate 2D electronic spectroscopy experiments, in which all pulses have the same spectrum.

A home-built Ti:sapphire regenerative-amplifier laser system generates 41-fs pulses centered at 805 nm, with a spectral bandwidth of ∼30 nm. The beam is split into two replicas

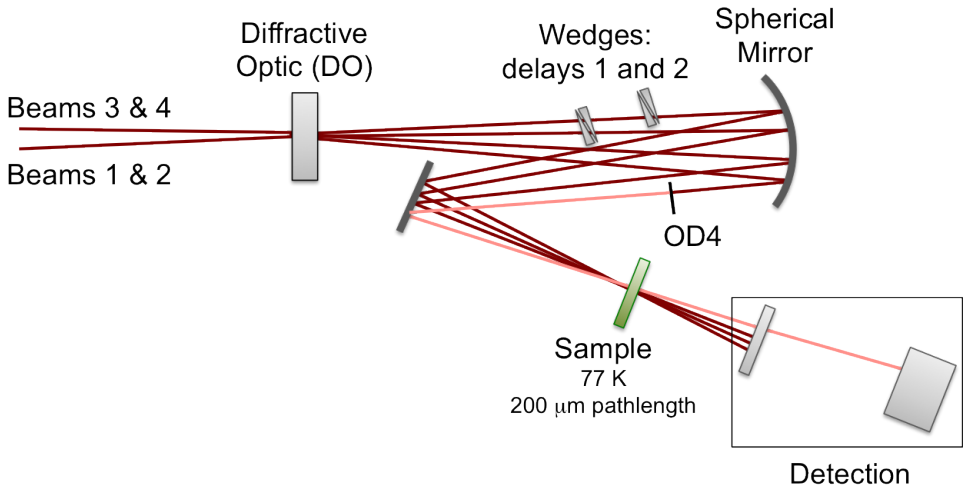

Figure 1.9: Schematic of the experimental setup. The two beam pairs 1 & 2 and 3 & 4 are split at the diffractive optic (DO). Beams 1 and 2 go through movable wedges (delays 1 and 2), allowing the interferometric control over the first delay τ. Beam 3 goes through a pair of glass wedges (not shown), to set the delay between pulse 3 and the local oscillator (beam 4). Beam 4 is attenuated by a factor of 4 going through a neutral density filter (OD4). The beams are focused at sample, contained in a 200 μm cuvette. The signal is emitted collinearly with beam 4 and detected. See Fig. 1.10 for the details of the detection system.

by a beam-splitter (1&2 and 3&4 in Figure 1.9), delayed with respect to each other by a computer-controlled retroreflector delay stage; this allows us to control the waiting time T between pulses 2 and 3. The two beam pairs are further split into two by a diffractive optic (DO) optimized for first-order diffraction, that allows for phase stability between them [45]. The coherence time τ is changed using movable glass wedges, which allow for interferometric precision in the control of τ. This high precision is required because of the Fourier transform that needs to be carried along the coherence time axis. The dispersion introduced by the glass can be compensated numerically. The beams are focused to the sample position and have an energy of $\sim$4 nJ per pulse. Pulse 4 is largely attenuated by means of a neutral density filter (OD = 4) and delayed with respect to beam 3 with another pair of glass wedges inserted into pulse 3 path. Pulse 4 is the *local oscillator* (LO), necessary to perform heterodyne detection of the signal field, which is emitted collinearly to the LO beam in the phase matched direction $\vec{k_s} = -\vec{k_1} + \vec{k_2} + \vec{k_3}$. The signal impinges then on a spectrometer, that spectrally resolves it on the pixels of a CCD camera (see figure 1.10). The Fourier transform along the emission axis (echo time t) is therefore performed directly by the experimental apparatus, and the signal is recorded as a spectral interferogram for fixed values of the coherence time τ and of the waiting time T:

$$I_{signal}(\tau, T, \omega_t) = |E_s(\tau, T, \omega_t) + E_4(\omega_t) e^{i\omega_t \Delta t}|^2 \tag{1.4.1.5}$$

where the signal electric field E_s is as in equation 1.4.1.3, E_4 is the electric field of the local oscillator, $\Delta t = t_4 - t_3$ [49]. By expanding this expression, we get:

$$I_{signal}(\tau, T, \omega_t) = |E_s(\tau, T, \omega_t)|^2 + |E_4(\omega_t)|^2 + E_s^*(\tau, T, \omega_t)E_4(\omega_t)e^{i\omega_t \Delta t} + E_4^*(\omega_t)E_s e^{-i\omega_t \Delta t} \quad (1.4.1.6)$$

The first term, the square of the signal field, is negligibly small; the second term, the intensity of the local oscillator field, can be measured separately and subtracted. The two cross terms, which can be rewritten as $2Re[E_s(\tau, T, \omega_t)E_4(\omega_t)]cos(\Delta\phi(\omega_t))$, constitute the spectral interferogram, that oscillates with the phase difference $\Delta\phi$ between the two fields.

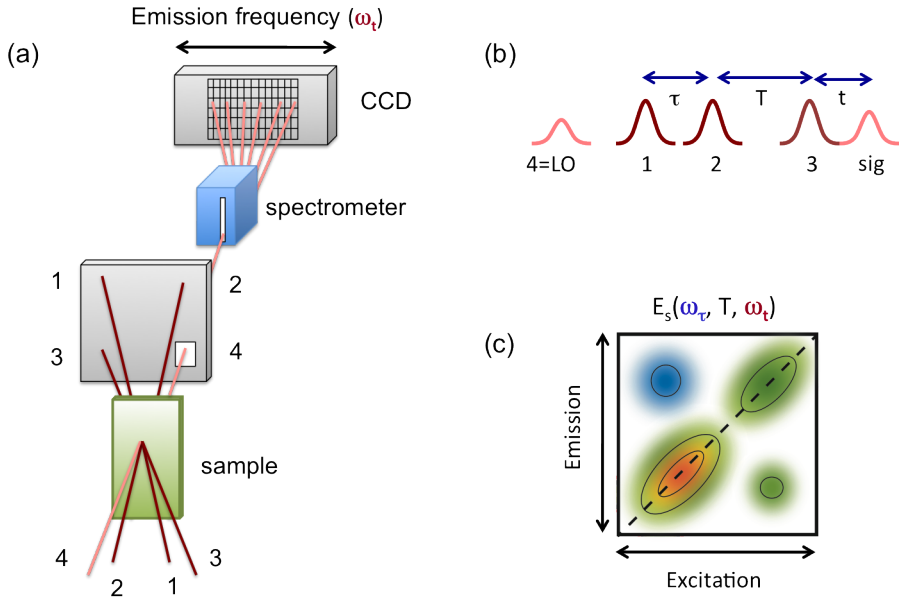

Figure 1.10: The detection system. (a) Laser beams geometry and detection system, showing the spectrometer and the CCD camera. Figure based on [50]. (b) The pulse sequence used in the experiment. (c) Upon Fourier transforming along the τ axis, the 2D spectrum is retrieved, with excitation frequencies on the horizontal axis, and emission frequencies on the vertical axis.

The coherence time is then scanned from -390 to 390 fs (negative times imply that pulse 2 is arriving before pulse 1) in 1.3 fs steps, keeping the waiting time *T* fixed. Hence, for fixed values of *T*, we obtain a two-dimensional interferogram, in which on the horizontal axis we have the values of the coherence time and on the vertical axis the emission frequency ω_t. A Fourier transform along the coherence time axis is then performed and the 2D spectrum is retrieved as in Figure 1.10 (c), where on the x axis we find the excitation frequency and on the y axis the emission frequency. By scanning the waiting time *T*, we construct a series of 2D spectra. Looking at the evolution of the features in the spectra as a function of T, we are able to get information on the excited state dynamics of the molecular system under investigation.

The 2D spectrum shown in Fig. 1.8 represents a relaxation spectrum, for waiting times $T > 0$. The relaxation spectrum is given by the combination of the photon echo contribution (rephasing signal, obtained experimentally for positive coherence times τ, when pulse 1 comes before pulse 2) and the free induction decay (nonrephasing signal, obtained exper-

imentally for negative values of the coherence time τ, when pulse 2 arrives before pulse 1). The individual components to the 2D relaxation spectrum contain useful information. In fact, the particular shape of the peaks in the nonrephasing spectrum (anti-diagonally elongated) allows us to discern closely spaced peaks, otherwise not separable in the relaxation spectrum (see Chapter 3). Additionally, since different pathways contribute differently to the rephasing and nonrephasing spectra, it is possible to discern the origin of specific features in the 2D spectra by looking separately at the rephasing or nonrephasing pathways (see Chapter 2).

1.4.2 Transient Absorption

Femtosecond transient absorption spectroscopy (TA) is a well established technique in ultrafast spectroscopy to measure photochemical processes occurring in the excited state of molecules. In particular, TA has been successfully used to probe the energy and charge transfer dynamics related to energy transfer and quenching processes in photosynthetic systems [51]. TA is particularly helpful in unraveling the excited state dynamics of non-emissive states, which are not accessible to other techniques such as time-resolved fluorescence. Non-emissive states play a very important role in photosynthesis, such as in energy transfer and quenching processes involving dark states of carotenoids.

In a typical TA experiment, a *pump* pulse creates a non-equilibrium state by exciting a fraction of the molecules to an excited state. After a controllable delay time *t*, a *probe* pulse is sent to the sample and monitors the state of the molecules (see Fig.1.11 (a)). TA is a third-order nonlinear spectroscopic technique, and upon two interactions with the pump beam and one interaction with the probe beam, the signal is radiated collinearly with the probe beam, in the direction $\vec{k}_{sig} = +\vec{k}_{pu} - \vec{k}_{pu} + \vec{k}_{pr} = \vec{k}_{pr}$.

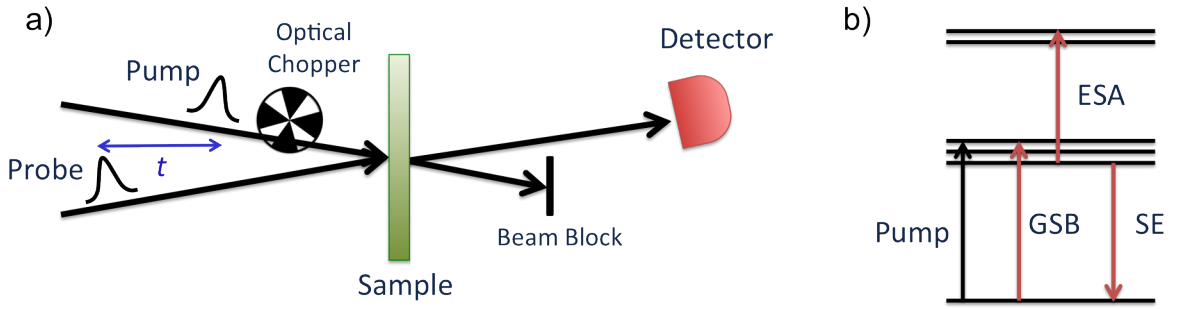

Figure 1.11: (a) Basic Setup for a TA experiment. Pump and probe pulses are separated by a controllable delay time *t*, and the pump pulse goes through an optical chopper. After interaction with the sample, the pump beam is blocked, while the transmitted probe is collected on a detector. (b) Contributions to the TA signal for a model system, upon excitation of an electronic transition: GSB = ground state bleach; ESA = excited state absorption; SE = stimulated emission.

By optically chopping the pump pulse, a differential absorption signal ΔA is measured as the difference in absorption of the probe beam in the sample in presence and in absence of the pump pulse. The delay time *t* between pump and probe can be varied, and the differ-

ence absorption signal is collected as a function of *t*. In a degenerate TA experiment, pump and probe pulses have the same spectrum. In order to be able to investigate energy transfer and coupling processes between different chromophores, non-degenerate experiments are usually performed. Additionally, spectrally resolved TA experiments can be performed using a broadband detector such as a photodiode array or a CCD camera. In this case, the probe pulse is usually supercontinuum generated in a sapphire or calcium fluoride plate, spanning the visible and near infrared (IR) regions (from 450 up to 1200 nm). The detector collects the differential absorption signal ΔA(*t*,λ) as a function of time delay *t* and probe spectrum λ. The ΔA(*t*,λ) spectrum contains information about the excited state dynamics of the system under investigation. Three main different types of processes can contribute to the TA signal (see also Fig. 1.11 (b)) [51]:

- *Ground State Bleach* (GSB): the effect of the pump pulse is to excite a fraction of the molecules into the excited state. This reduces the number of molecules available for absorption in the ground state in the presence of the pump pulse, therefore the contribution of ground state bleach effects to the ΔA(*t*,λ) signal is negative.

- *Stimulated Emission* (SE): the Einstein coefficients for stimulated emission and absorption for a two level system are the same, therefore the probe photons can also induce the stimulated emission of additional photons from an excited state back to the ground state if the transition is allowed. This emission occurs at the same frequency and in the same direction as the probe photons that have stimulated the transition. This process corresponds to an increase in the signal detected, therefore to a negative contribution to the ΔA(*t*,λ) signal.

- *Excited State Absorption* (ESA): depending on the particular energy level structure of the system under investigation, we can observe absorption of the probe beam if resonant with allowed transitions to higher lying states. This process contributes with a positive sign to the ΔA(*t*,λ) signal.

What the detector measures is the change in probe intensity when the pump is present versus when it is not present. In particular, the signal that is recorded is related to the third order polarization generated in the sample as follows [52]:

$$\frac{\Delta I_{probe}(\omega)}{I^0_{probe}(\omega)} = \frac{n\omega L}{\epsilon_0 c} Im\left\{\frac{P^{(3)}(\omega)}{E_{probe}(\omega)}\right\} \tag{1.4.2.1}$$

where $I^0_{probe}(\omega)$ is the probe intensity in absence of the pump, n is the refractive index, L is the sample thickness and $E_{probe}(\omega)$ is the electric field of the transmitted probe on the detector. The measured intensity is related to the absorption difference by the relation:

$$I(\omega) = I^0(\omega) * exp(-\Delta\alpha(\omega)L) \tag{1.4.2.2}$$

where $\alpha(\omega)$ is the absorption coefficient.

Experimental Apparatus

Figure 1.12 shows a schematic of the experimental setup used for the TA experiments described in Chapters 2, 4. The details pertaining to the specific experiment are specified in the corresponding Section.

A diode-pumped, frequency-doubled Nd:YVO4 laser (Coherent Verdi V-18) pumps a commercial femtosecond laser system (Coherent Mira and Coherent RegA 9050) to produce pulses of $\sim$ 60 fs duration, centered at 800 nm. The beam is split into two portions. The pump pulse is produced in an optical parametric amplifier (Coherent OPA 9040). The center wavelength is tunable from 480 up to 700 nm, with a bandwidth of 10 - 20 nm FWHM. The duration of the compressed pulse (after prism compression) is approximately 40 fs as measured by autocorrelation of the pump pulse in a β- barium borate (BBO) crystal. The pump beam is optically modulated by a chopper at a frequency such as to reduce electrical noise. The broadband probe pulse is produced by focusing the radiation from the laser system into a 2-mm Sapphire plate, which generates a supercontinuum ranging from 450 nm - 1200 nm. After the plate, a short (long) pass filter selects the visible (near-infrared) portion of the supercontinuum to be used as a probe.

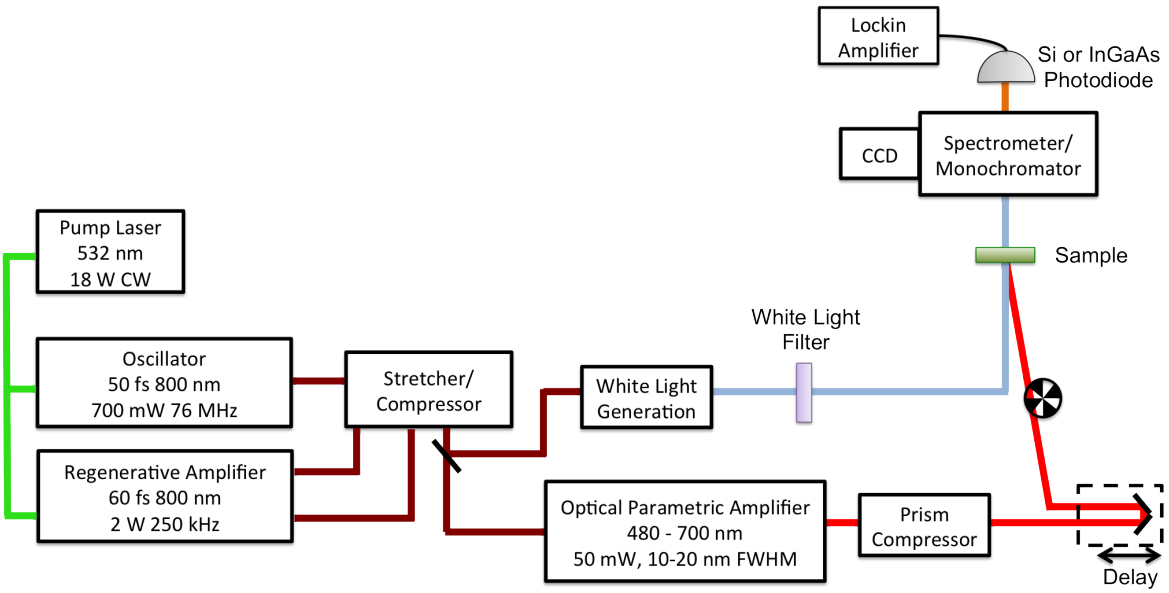

Figure 1.12: Schematic of the apparatus used for the TA experiments described in the next chapters. The laser system produces $\sim$ 60 fs pulses centered at 800 nm. The radiation is split by a beamsplitter: a portion goes through an optical parametric amplifier to produce pulses in the visible of $\sim$ 10-20 nm FWHM, and $\sim$ 40 fs duration after prism compression. These pulses are sent through a delay stage and an optical chopper and constitute the pump beam. The other portion of the radiation from the laser is used to generate white light in a 2 mm sapphire crystal. The generated supercontinuum is passed through an appropriate filter to select the spectral region of interest (either visible or near infrared) and sent to the sample as the probe beam. After the sample, the transmitted probe is either dispersed with a spectrometer on the pixels of a CCD camera for spectrally resolved detection, or a specific wavelength is selected by a monochromator and detected on a photodiode connected to a lockin amplifier.

Pump and probe beams are focused at the sample, typically contained in a cuvette of 1 mm path length (pump spot size ∼250 μm, probe spot size ∼100 μm). The delay between pump and probe pulses is controlled by translating a retroreflector mounted on an optical delay stage (Newport Nanomover). After the sample, the pump pulse is blocked and the probe pulse is focused with a f=30 cm lens onto the slit of a spectrometer (Princeton Instruments). The spectrometer can be used to disperse the beam onto the pixels of a CCD camera (Princeton Instruments NTE2), for spectrally resolved TA experiments. The spectral response of our CCD is such that only the visible portion of the probe spectrum can be detected, therefore we put a short pass filter in the probe beam, before the sample, to filter out the near-infrared portion (SPF700 or SPF750, CVI-Melles Griot). Additionally, in order to increase the signal to noise ratio of the data collected on the CCD, a reference beam is collected simultaneously. The reference is obtained by putting a beamsplitter in the probe beam and collecting the transmitted portion (while the reflected portion is used as a probe). The reference beam travels parallel to the probe beam, and hits the sample without overlapping with the pump beam. Both probe and reference beams are detected onto the CCD and the TA signal is measured as[i]:

$$\Delta OD(t,\lambda) = log\left(\frac{I_{pr}(t,\lambda)}{I_{ref}(\lambda)}\right)_{Pump\,off} - log\left(\frac{I_{pr}(t,\lambda)}{I_{ref}(\lambda)}\right)_{Pump\,on} \tag{1.4.2.3}$$

It is also possible to detect the differential absorption signal ΔA(t) with a photodiode. In this case, the spectrometer can be used as a monochromator and we are able to select the wavelength of interest and detect the signal using either a Si photodiode (for visible probe wavelengths, Thorlabs DET 210) or an InGaAs photodiode (for near IR wavelengths, Thorlabs DET 410).

1.4.3 Time correlated single photon counting

Time correlated Single Photon Counting (TCSPC) is an established time-domain technique that measures the timescale of fluorescence decay of excited states [53]. In a TCSPC experiment the fluorescence intensity $I(t)$ is measured as a function of time. In case of single exponential decay, the intensity decays as a function of time as:

$$I(t) = I(0)\,exp(-t/\tau) \tag{1.4.3.1}$$

and the lifetime τ represents the inverse of the total decay rate, given by the sum of rates that contribute to the depopulation of the excited state (fluorescence, non radiative decay). The lifetime represents the average time that a fluorophore spends in the excited state after excitation.

More generally, intensity decays are multiexponential, and the lifetimes can be obtained from the intensity decay by fitting the curve to the following equation:

[i] the OD (Optical Density) is equivalent to the absorbance and corresponds to the logarithmic ratio between final and initial intensities, $OD = log_{10}(\frac{I(\omega)}{I^0(\omega)})$

$$I(t) = \sum_{i=1} A_i \, exp(-t/\tau_i) \tag{1.4.3.2}$$

TCSPC is based on the detection of less than one photon per excitation pulse. When a photon is detected, its arrival time with respect to a reference start time collected on a photodiode (see Fig. 1.13) is recorded. The photons are then binned as a function of the arrival time. After enough photons are accumulated, a histogram representing $I(t)$ is retrieved. This curve then needs to be deconvolved from the instrument response function (IRF) which is collected separately using a scattering sample. TCSPC measurements are based on Poisson statistics: the probability of emission of a single photon after excitation is equivalent to the actual intensity versus time distribution of all the photons emitted after excitation.

Experimental Apparatus

A commercial mode-locked Ti:Sapphire oscillator (Coherent Mira 900F) generates 150 fs pulses at a repetition rate of 76 MHz (see Fig. 1.13). The central wavelength is tuned to 820 nm with a full width at half-maximum (FWHM) of 12 nm. The output is frequency doubled in a 1-mm-thick BBO crystal, producing a pulse centered at 410 nm with an energy at sample of $\sim$10 pJ/pulse. The repetition rate of the pulses is reduced by a factor of 8 using a pulse picker (Spectra Physics model 3980). The fluorescence emission is sent through a polarizer set at magic angle (54.7°, to avoid anisotropy or rotational diffusion effects), followed by a monochromator (HORIBA Jobin-Yvon H-20) or a long pass filter. The fluorescence is detected with a MCP/PMT detector (microchannel plate photomultiplier tube, Hamamatsu R3809U), electrically cooled to -30° C and connected to a PC computer through a DCC-100 detector control (Becker-Hickl). The FWHM of the instrument response function (IRF), measured with dilute non-dairy creamer, is 45-55 ps. The samples are held in 1 or 2 mm - thick quartz cuvettes (Starna Cells) and kept at $\sim$12° using a home-built nitrogen cooling system.

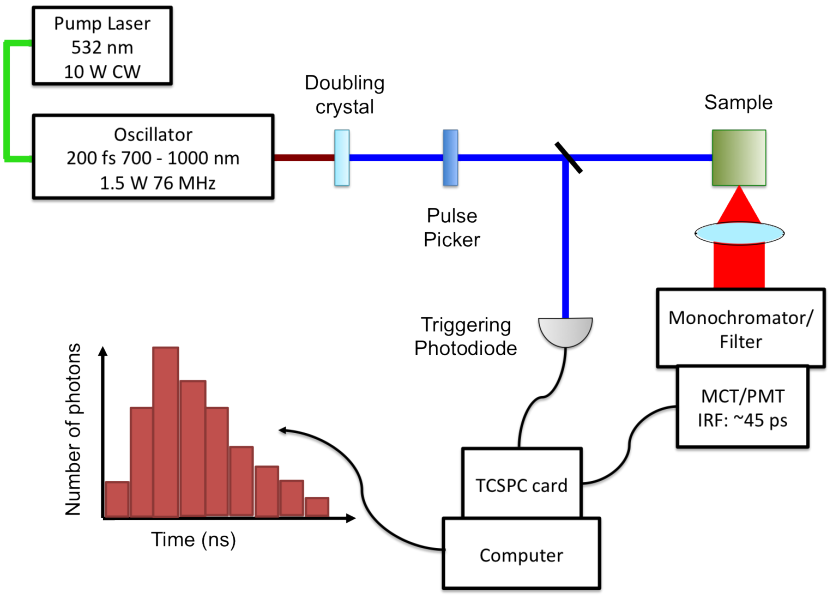

Figure 1.13: Schematic of the apparatus used for the TCSPC experiments. The radiation from the laser is doubled in frequency in a doubling crystal as to produce $\sim$ 400 nm radiation. A pulse picker reduces the repetition rate of the pulse train, exciting the sample. The emitted fluorescence is detected on a MCT/PMT detector connected to a TCSPC card on a computer. The detection wavelength is selected using either a monochromator or a band pass filter. A portion of the excitation beam is used to send a triggering signal to a photodiode, that communicates with the TCSPC card to set the start/stop time for photon collection. A histogram is built, plotting the number of photons arriving at the detector as a function of time.

Chapter 2

The Orange Carotenoid Protein

Contents

2.1 Photosynthesis and photoprotection in cyanobacteria

Cyanobacteria are oxygenic photosynthetic organisms that evolved at least 3 billion years ago. According to the endosymbiotic theory, they are precursors for chloroplasts of eukaryotic organisms such as green algae and plants. The main photosynthetic antennae of cyanobacteria are the phycobilisomes, which are found on the outside of the thylakoid membrane, on the stromal side, and associated to Photosystem II (PSII; see Fig. 2.1) [54, 55] and Photosystem I [56]. Phycobilisomes are large complexes composed of pigment-binding phycobiliproteins, held together by linker peptides. They are composed of a core, constructed of trimeric disks of allophycocyanin (APC), from which usually six cylindrical rods radiate. The rods are composed primarily of phycoerythrin and phycocyanin. The main pigments bound

are bilins, open-chain tetrapyrroles. Bilins in phycobiliproteins absorb energy in the green-orange region of the spectrum (465 - 665nm), extending the light-harvesting capabilities of chlorophyll. Excitation energy absorbed in the phycobilisomes is funneled from the exterior of the rods to the core in an efficient downhill energy transfer process. From the core, energy is transferred to PSII, where it drives charge separation in the reaction center.

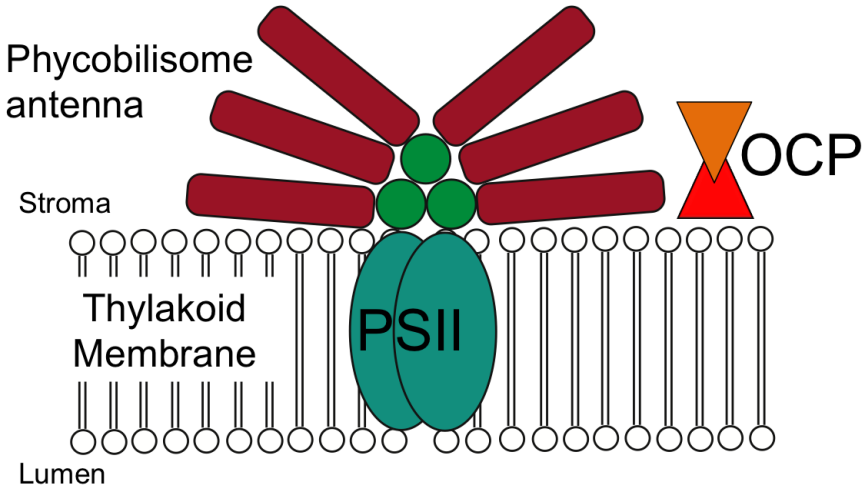

Figure 2.1: Cartoon of the photosynthetic apparatus of cyanobacteria, showing the antenna system (phycobilisome), and Photosystem II (PSII) embedded in the thylakoid membrane. OCP is shown unbound, on the stromal side of the membrane.

As discussed in the Introduction, photosynthetic organisms need to be able to cope with the variability in light conditions, harvesting sufficient light to drive photochemistry while at the same time avoiding excess light absorption. In cyanobacteria, strong blue light has been shown to induce a type of NPQ associated with the phycobilisomes [57]. The action spectrum of this type of NPQ resembles very closely the absorption spectrum of a carotenoid (hydroxyechinenone) [58], suggesting its direct involvement in the NPQ process. Eventually, it was demonstrated that a carotenoid-binding protein, the Orange Carotenoid Protein (OCP) is involved in this phycobilisome-related NPQ [59]. The NPQ mechanism associated with OCP will be referred to in the following as OCP-NPQ. Unlike the rapid components of NPQ in plants, OCP-NPQ is not related to the induction of a trans-thylakoid ΔpH, nor to the de-epoxidation state of the carotenoid [60, 61]. While the involvement of OCP in blue-light induced quenching is known, the precise molecular mechanisms of OCP-NPQ and the details of the interactions between OCP and the phycobilisome antenna still need to be elucidated.

Other photoprotection mechanisms exist in cyanobacteria [61, 62]. Zeaxanthin plays an important role, as mutants lacking this carotenoid are sensitive to strong light [63]. Under iron stress conditions, the Chl-binding protein IsiA (Iron-starvation inducible protein) forms quenching complexes [64, 65]. In high light or under temperature or nutrient stress, single-helix Chl-binding proteins HLIPs (High Light Inducible Proteins) are expressed and play a

photoprotective role [66, 67]. In this thesis chapter, we will focus on the OCP-NPQ quenching mechanism found in cyanobacteria. In particular, Section 2.2 will be devoted to the description of what is known about OCP-NPQ and what still needs to be described. Section 2.3 will be devoted to the description of 2DES experiments on OCP, while Section 2.4 will describe transient absorption results obtained on this PPC. Finally, Section 2.5 will summarize the results obtained and give the interpretation of these results in terms of implications for OCP-NPQ.

2.2 The OCP-related photoprotection mechanism in cyanobacteria

In Section 1.2 we have discussed how evolution has diversified the light-harvesting apparatuses of photosynthetic organisms, and thus the corresponding photoprotection mechanisms. The precursors of all eukaryotic photosynthetic chloroplasts are cyanobacteria, therefore the type of flexible NPQ in this organism comes early in the evolutionary pathway.

Flexible NPQ in cyanobacteria is induced by blue-green light and mediated by a water-soluble protein, the Orange Carotenoid Protein (OCP). The intensity and color of light determines the photoprotection strategy adopted by cyanobacteria: low levels of blue light (20 μmol photons m^{-2} s^{-1}) induce state transitions; higher levels (but still well below PSII activity saturation) induce OCP-dependent quenching. 440 μmol photons m^{-2} $s^{-}1$ of light induce OCP-NPQ, even though PSII activity is only at 30% [61]. No induction of OCP-NPQ is observed for wavelengths longer than 520 nm [57].

As will be explained in more detail in the next Section, OCP non-covalently binds a single carotenoid, 3-hydroxyechinenone, which spans two distinct structural domains of the protein. OCP acts as a switch for photoprotection and combines the functions of light sensor and quencher of excess excitation. The OCP-related photoprotective mechanism occurs as a three-step process (see Fig. 2.2): 1) light intensity-dependent photoactivation of OCP; 2) light-independent formation of the quenching complex by binding of OCP to phycobilisomes (PBS) [68]; 3) detachment of OCPR from PBS mediated by the action of the Fluorescence Recovery Protein (FRP).

In darkness, OCP is not attached to the PBS. The carotenoid is sparingly solvent-exposed, suggesting that a conformational change of the protein, which makes the carotenoid more accessible, is necessary for binding to the antenna and for energy dissipation. The concentration of activated protein is very low in darkness or under low light conditions [69].

1. **Photoconversion:** Upon absorption of blue-green light, OCPO undergoes conformational changes at the level of the pigment and of the protein and converts to a metastable form, OCPR. OCPR is able to bind to the phycobilisome antenna and quench fluorescence. The quantum yield of OCPO to OCPR conversion is estimated to be 1% in vitro [69]. Gorbunov *et al.* estimate a quantum yield for formation of quenching complexes (OCPO to OCPR photoconversion followed by binding of OCPR to the PBS) of 0.1%

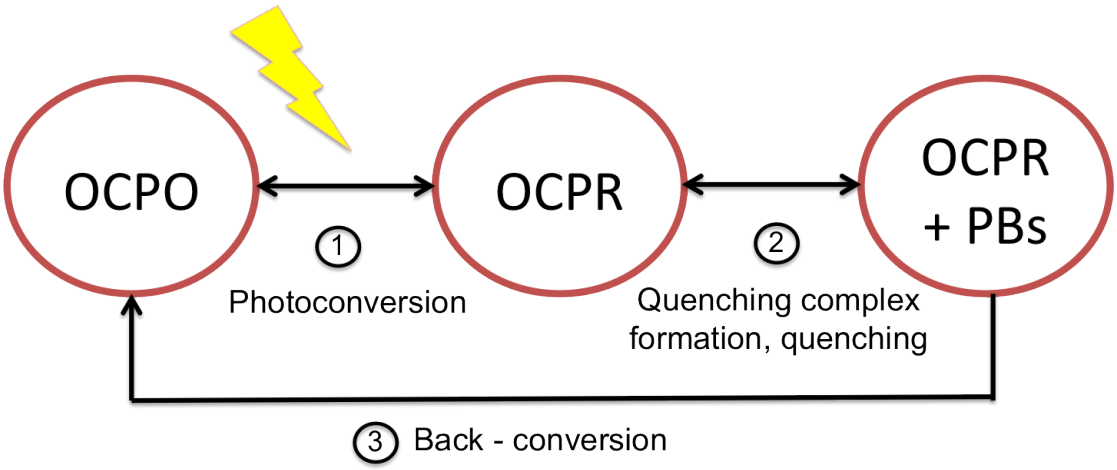

Figure 2.2: Three state model for the OCP-NPQ mechanism. (1) Upon light absorption, OCPO undergoes photoconversion, switching to its red form (OCPR), with conformational changes at the level of both the protein and the pigment. (2) Subsequently, formation of a quenching complex with the phycobilisome antenna can occur (see text for yield), followed by quenching of excess absorbed energy. (3) Back conversion dynamics are independent of temperature and break the quenching complex and induce the conversion back to the OCPO conformation.

in vivo [70]. Photoconversion of OCP to the red form is not sufficient for formation of a quenching state *in vivo*, as the binding to the PBS is also required.

2. **Formation of quenching complex and quenching:** After photoconversion, OCPR is able to bind to the core of the phycobilisome; the phycobilisome rods stabilize OCPR binding [68]. The interaction occurs via the N-terminal domain of the OCP [71]. Excitonic energy is transferred away from the phycobilisome core, suppressing the pathway from PBS to Chl *a* and reaction centers in PSII. NPQ reduces the amount of absorbed light energy transferred from the PBS to the RC by 52% [70]. The amplitude of fluorescence quenching depends on OCP concentration; WT contains 1 OCP per 2-3 PBS and the quenching of maximal fluorescence is ∼30% [69]. High light stress and iron starvation cause an increase in fluorescence quenching, correlated with an increase in OCP concentration relative to Chls and phycobiliproteins [72].

3. **Back-conversion and role of the Fluorescence Recovery Protein:** Isolated OCPR spontaneously converts back to OCPO in darkness, with strong temperature dependence (30 sec at 32 C to ∼45 min at 11 C) [69]. *In vivo*, attachment of OCPR to the PBS stabilizes OCPR and another protein, the Fluorescence Recovery Protein (FRP), is needed for detachment from the PBS and back-conversion to OCPO [68]. FRP is a soluble protein that does not bind pigments. *In vitro*, FRP accelerates the back-conversion of OCPR to OCPO [73]. *In vivo*, FRP undocks OCPR from the phycobilisome and is essential to recover the full antenna capacity [73]. FRP interacts with the C-terminal domain of the OCP [74], possibly driving the N- and C- terminal domains back together or otherwise triggering the conformational change of the protein back towards

OCPO. FRP has a higher affinity for OCPR, suggesting that the conformational change occurring upon photoconversion is required not only for OCP docking to the PBS, but also for FRP interaction [73]. Most likely, FRP acts by lowering the activation energy of the OCPR to OCPO reaction, but the molecular mechanism of this reaction is still unknown [75]. FRP cannot be activated/deactivated by light, as it binds no chromophore, and therefore needs to be present in lower concentration than the OCP to ensure maximal NPQ efficiency [73].

2.3 Broadband 2D Electronic Spectroscopy on the two forms of OCP

This Section is reproduced (adapted) with permission from:
"Insights Into the Structural Changes Occurring upon Photoconversion in the Orange Carotenoid Protein from Broadband Two-Dimensional Electronic Spectroscopy"
by Eleonora De Re, Gabriela S. Schlau-Cohen, Ryan L. Leverenz, Vanessa M. Huxter, Thomas A. A. Oliver, Richard A. Mathies and Graham R. Fleming,
accepted for publication to the *Journal of Physical Chemistry B*
DOI: 10.1021/jp502120h

Abstract

Carotenoids play an essential role in photoprotection, interacting with other pigments to safely dissipate excess absorbed energy as heat. In cyanobacteria, the short timescale photoprotective mechanisms involve the photoactive Orange Carotenoid Protein (OCP), which binds a single carbonyl carotenoid. Blue-green light induces the photoswitching of OCP from its ground state form (OCPO) to a metastable photoproduct (OCPR). OCPR can bind to the phycobilisome antenna and induce fluorescence quenching. The photoswitching is accompanied by structural and functional changes at the level of the protein and of the bound carotenoid. Here, we use broadband two-dimensional electronic spectroscopy to study the differences in excited state dynamics of the carotenoid in the two forms of OCP. Our results provide insight into the origin of the pronounced vibrational lineshape and oscillatory dynamics observed in linear absorption and 2D electronic spectroscopy of OCPO, and the large inhomogeneous broadening in OCPR, with consequences for the chemical function of the two forms.

2.3.1 Introduction

Light absorption can be dangerous to photosynthetic organisms when it exceeds their capability to convert light energy into chemical energy. To avoid formation of damaging species

upon excess light absorption, photosynthetic organisms adopt a series of mechanisms to dissipate light energy safely as heat, collectively referred to as non-photochemical quenching (NPQ). Carotenoids play a critical role in NPQ, as validated by a variety of biochemical [76, 77], spectroscopic [78, 40, 27, 31, 33] and theoretical studies [41, 42]. The mechanistic role of carotenoids in NPQ, however, is still not fully understood [18]. In cyanobacteria, excess light absorption induces a photoprotective mechanism that involves a carotenoid-binding photoactive protein, the Orange Carotenoid Protein (OCP), which both senses light intensity and directly triggers photoprotection [58, 59, 2].

OCP is a soluble 35 kDa protein found in the inter-thylakoid region, on the same side of the membrane as the phycobilisome antenna, the major light-harvester in cyanobacteria [59, 79]. OCP non-covalently binds a single pigment, the carotenoid 3′-hydroxyechinenone (3′-hECN). Absorption of blue-green light by OCP induces conformational changes in both the pigment and the protein, as experimentally demonstrated by Raman, FTIR experiments and native mass spectrometry [69, 80]. These changes convert the protein from its dark stable photoactive form, the orange OCPO, to a metastable form, the red OCPR. OCPR has been suggested to adopt an "open" conformation with increased accessibility of the carotenoid to solvent [81, 71, 82, 83] and a weaker protein-carotenoid binding interaction [80]. OCPR has been shown to bind to the phycobilisome antenna and induce fluorescence quenching [59, 69, 68]. Isolated OCPR spontaneously converts back to the orange form in darkness and the back-conversion kinetics are independent of illumination but very sensitive to temperature. The conversion takes a few seconds at room temperature (298 K) and $\sim$ 40 minutes at 283 K [69].

OCPO binds the carotenoid 3′-hECN in an all-trans configuration (see Fig. 2.3 (a)) [79]. The carbonyl on the 4-keto-β-ionylidene ring of 3′-hECN forms hydrogen bonds at the C-terminal domain of the protein. This carbonyl group is essential for OCP photoactivity, as OCP with zeaxanthin or β-carotene bound (which do not have a carbonyl group) is unable to photoconvert [84]. The roles of specific pigment-protein interactions responsible for tuning the spectroscopic and photochemical properties of 3′-hECN in OCP remain largely uncharacterized. Moreover, the conformation of the carotenoid and its interactions with the surrounding protein in OCPR are not conclusively known, as crystal and NMR structures are unavailable for this form.

In this paper, we investigate the photophysics of 3′-hECN in the two forms of OCP using two-dimensional electronic spectroscopy (2DES), to understand how the protein environment modulates the pigment energetics and dynamics in OCPO and OCPR, and relate this to the different biological function of the two forms (photoactive vs. quenching). OCP is an ideal minimal system for the study of protein-pigment interactions, as it binds a single carotenoid. In contrast to other pigment-protein complexes that bind both carotenoids and chlorophyll pigments, the optical response of this minimal system is not complicated by inter-chromophore interactions, allowing direct observation of how the protein environment tunes and alters the properties of the pigment. Carotenoid photophysics are highly dependent both on the structure of the pigment and on the surrounding environment [6]. Therefore, observed differences in the photophysics of the two forms of OCP must arise from changes in the structure of the carotenoid bound to the protein pocket and in the pigment-protein binding

interaction.

Previous time-resolved fluorescence [85] and transient absorption experiments [86, 87, 82] have investigated the mechanism played by OCP in energy dissipation. Transient absorption experiments in the visible [86, 82] suggested that OCPR could accept excitation energy from the phycobilisome bilin S_1 state to the carotenoid intramolecular charge transfer (ICT) state. The ICT state can subsequently relax to the ground state directly or via the S_1 state of 3′-hECN and then decay. Many open questions remain about the molecular origin of the different spectroscopic behavior observed for OCPO and OCPR. For example, the origin of the broadness and red-shifting of the OCPR linear absorption has not been fully elucidated, and the origin of the ICT character enhancement in OCPR [86, 82] is incompletely described.

2DES presents numerous advantages over other nonlinear spectroscopic techniques such as transient absorption (for recent reviews see [50, 49, 88, 89]). 2DES affords time and spectral resolution over both excitation and emission processes and has been very successful in unraveling the complicated structure-function relationship of natural photosynthetic systems [90, 91, 92, 93, 94]. Broadband 2DES probing the visible region allows us to investigate and disentangle a spectral region usually congested in carotenoid photophysics and simultaneously provides the time resolution to investigate the ultrafast processes associated with the excited state relaxation of carotenoids [95].

Our 2DES results for the two forms of OCP are remarkably different. OCPO shows pronounced vibrational dynamics, while OCPR gives a highly inhomogeneously broadened signal. We discuss how the differences in protein environment for the carotenoid in the two forms might relate to their specific biological roles (photoactivity and quenching).

2.3.2 Experimental Methods

Sample Preparation

OCP was purified from a frozen paste of *Arthrospira platensis* cells (a generous gift of Dr. Gerald Cysewski, Cyanotech Corporation) using a procedure similar to that described by Holt and Krogmann [96], with isoelectric focusing omitted. Following anion exchange and gel-filtration chromatography, the purified OCP had an A496:A280 ratio of 1.8:1. To prepare OCP for spectroscopic measurements, purified OCP in 50 mM Tris-HCl, 100 mM NaCl, pH 8 (24 °C) was concentrated to OD 30/cm in a centrifugal spin concentrator. For the OCPR sample, a 30 μL volume of concentrated OCP was initially converted to OCPR by 15 minutes of illumination with a 505 nm LED (Luxeon Rebel LXML-PE01-0070, Philips Lumileds, 40 nm FWHM) at 273 K. The illuminated sample was thoroughly mixed with 70 μL of chilled glycerol and illuminated for an additional 5 minutes. The sample was then transferred to a 200 μm path length quartz cuvette and cooled down to 77 K in an optical cryostat (Oxford Instruments). The OCPR sample was continuously illuminated with the LED during the cooling to cryogenic temperature. The OCPO sample was prepared similarly but in complete darkness. The maximum OD was 0.28 at 502 nm for the OCPO sample, and 0.25 at 518 nm for the OCPR sample. Linear absorption traces were collected before and after every 2DES measurement to check for sample stability at 77 K, and no measurable difference was

observed in either sample. We cannot exclude a minor presence of RCP (red carotenoid protein [59, 96, 97]) in our OCP preparations based on the linear absorption alone. However, its contribution would be the same in both OCPO and OCPR spectra, and we do not expect it to contribute to any observed differences in the dynamics of 3′-hECN in the two forms.

2D Electronic Spectroscopy

The 2DES experimental apparatus has been described in detail previously [95, 98, 45]. A home-built Ti:sapphire regenerative-amplifier laser system pumped a home-built non-collinear optical parametric amplifier, producing laser pulses centered at 540 nm (550 nm for OCPR measurements) with 60 nm FWHM. The combination of a prism compression line followed by a diffraction-based SLM (Spatial Light Modulator) pulse shaper compressed the pulses to a duration of 12 fs, as characterized by TG-FROG (Transient Grating-Frequency Resolved Optical Gating) [99]. The beam was split into two replicas by a beam-splitter, delayed with respect to each other via a retroreflector delay stage; this allowed the control of the waiting time *T* between pulses 2 and 3. The two beam pairs were further split into a total of four beams by a diffractive optic optimized for first-order diffraction, allowing for passive phase stabilization [45]. The delay between pulses 1 and 2, which corresponds to the coherence time τ, was implemented by means of movable glass wedges, allowing for interferometric precision in the control of τ [45].

The beams were focused to the sample position in a box geometry and had an energy of $\sim$10 nJ per pulse. The interaction with pulses 1, 2 and 3 generates a third-order signal in the phase-matched direction, $\vec{k_s} = -\vec{k_1} + \vec{k_2} + \vec{k_3}$, collinear with beam 4, the local oscillator (attenuated by four orders of magnitude as to prevent any strong interaction with the sample). This signal was spectrally dispersed and heterodyne-detected on a CCD camera.

The coherence time τ was scanned from -360 to + 360 fs in 0.8 fs timesteps, for fixed values of waiting time *T*. The resulting array of interferograms collected for each value of *T* was Fourier-transformed to produce the final 2DES spectrum. Negative values of the coherence time generated the nonrephasing signal (free induction decay), while positive coherence times generated the rephasing signal (photon echo signal). The two signals were obtained experimentally by inverting the ordering of pulses 1 and 2. The total 2DES spectrum, the relaxation spectrum, corresponds to the combined rephasing and nonrephasing components.

Dynamics were monitored by varying the waiting time *T*; spectra were collected every 10 fs from 0 to 100 fs, then at 120, 150, 300, 450, 1000, 2000, 5000, 7000, 10000, 15000, 20000 fs. In order to phase the 2DES data, spectrally resolved pump-probe experiments were collected separately for the same values of *T* under the same experimental conditions [100, 45].

2.3.3 Results

Linear Absorption

Fig. 2.3 (b) shows the linear absorption spectrum of the two forms of OCP at 283 K and at 77 K. OCPO, represented by an orange line, has resolvable features that corresponds to the

vibronic structure of the optically bright S_0-S_2 transition. The 0-0 transition is at 499 nm at 283 K, and is red-shifted to 502 nm at 77 K. The OCPO sample appears orange, as shown in the inset on the left in Fig. 2.3 (b). The structure of 3′-hECN in OCP is shown in Fig. 2.3 (a) [101]. The linear absorption spectrum at 283 K is asymmetrically broadened towards longer wavelengths. This broadening is reduced in the 77 K spectrum.

Upon blue-green light illumination, the absorption spectrum broadens and red-shifts. The main peak for the red form OCPR is at 512 nm at 283 K and red-shifts to 522 nm at 77 K. The vibrational structure that was visible in OCPO is lost and the spectrum appears nearly Gaussian, as seen in Fig 2.3 (b). No apparent band narrowing or increased resolution of vibronic structure is observed in the OCPR spectrum at 77 K.

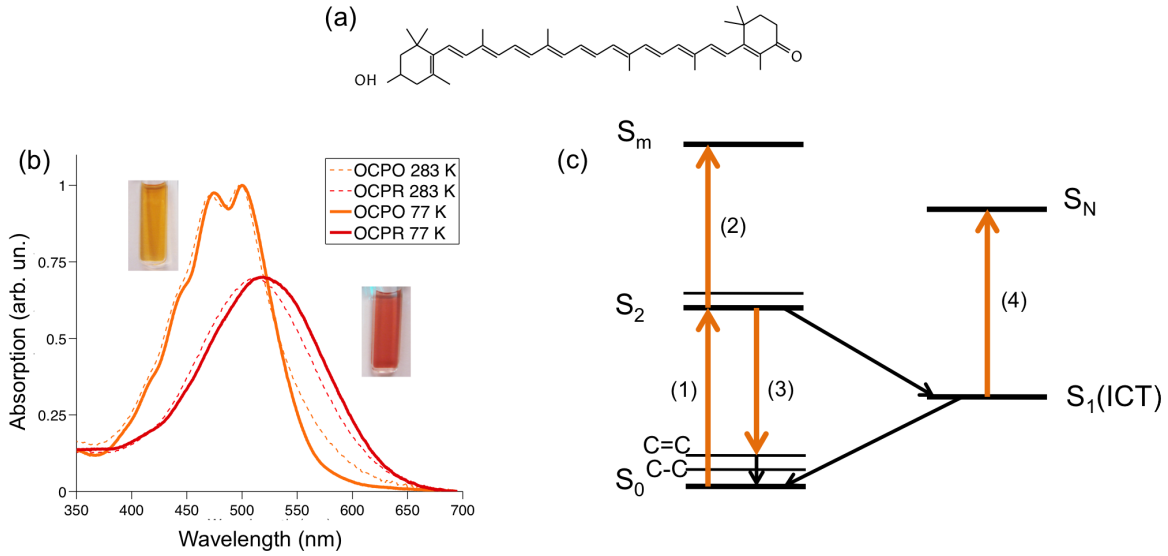

Figure 2.3: (a) Structure of the carotenoid 3′-hECN in the protein pocket in OCPO [101]. (b) Normalized linear absorption spectra of OCPO (orange line) and OCPR (red line) at 283 K (dashed line) and at 77 K (solid line). Pictures of the cuvettes containing the samples are shown next to the corresponding absorption spectra. (c) Energy level scheme of the key transitions within the main molecular pathways for the carotenoid 3′-hECN. The numbered transitions are: (1) $S_0 \rightarrow S_2$ ground-state bleach; (2) $S_2 \rightarrow S_m$ excited-state absorption; (3) S_2 emission; (4) S_1 excited-state absorption. The experimentally observable transitions are described for the two forms of OCP in the text.

2D Electronic Spectroscopy of OCPO

Fig. 2.4 (a) shows the laser spectrum used in the experiment, superimposed on the absorption spectrum of OCPO at 77 K. The laser pulse is resonant with the S_0-S_2 electronic transition of the carotenoid, covering the 0-0 vibrational transition and the red edge of the 0-1 transition.

Fig. 2.4 (b-d) display representative 2DES real-valued relaxation spectra of OCPO. The corresponding absolute-valued spectra are shown in the Supporting Information. Spectra acquired at long waiting times T (see T = 7 ps in Fig. 2.4 (d)), have two main features, A and B, with opposite signs. Short time spectra (T ¡ 1 ps) are more complex (see Fig. 2.4 (b)-(c)), with multiple overlapping positive and negative features.

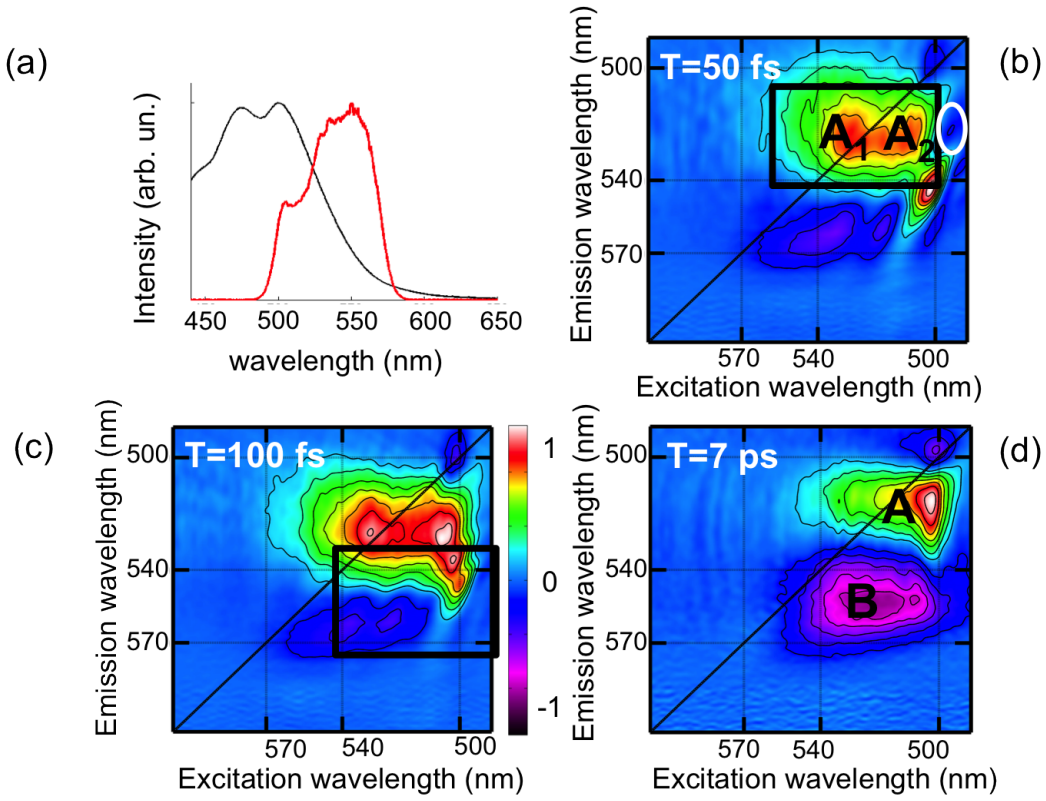

Figure 2.4: (a) Linear absorption spectrum of OCPO at 77 K (black line) and laser spectrum used in the experiment (red line). (b),(c),(d) Real-valued relaxation 2DES spectra of OCPO for selected waiting times T. Positive signals are displayed in red and green, negative signals in purple and blue (see colorbar). The letters and boxes highlight key peaks, described in the text.

The laser pulse excites the system into the S_2 state; the positive feature centered around 515 nm (boxed region in Fig. 2.4 (b)) is assigned to a ground state bleach (GSB)/stimulated emission (SE) signal from the $S_2 \rightarrow S_0$ transition. At early waiting times T we observe the presence of a negative signal centered around 502 nm excitation, 527 nm emission (see Fig. 2.4 (b), circled region in T = 50 fs spectrum). At this waiting time the negative signal has mostly decayed, so it appears blue shifted along the excitation axis, as the bleach signal becomes stronger. Given the spectral position of this negative band and the timescale of decay (the signal disappears after $\sim$ 50 fs), we assign it to an $S_2 \rightarrow S_m$ excited state absorption (ESA). ESA from S_2 has previously been observed in the visible region in 2DES experiments on β-carotene in solution [102, 95]. As the decay of the S_2 ESA signal proceeds, we see the appearance of two separate regions of intensity in the GSB/SE band, labeled A_1 and A_2 in the T = 50 fs spectrum in Fig. 2.4 (b). A_1 and A_2 have an energy separation of $\sim$ 1000 cm^{-1} and they oscillate in intensity with a period of $\sim$ 30 fs. The integrated intensity of the 2DES relaxation spectra in regions A_1 and A_2 is plotted as a function of waiting time T in Fig. 2.5. The oscillation frequency is close to the frequencies of C=C and C-C stretching of the ground state of the carotenoid 3′-hECN (21 and 28 fs, respectively [69]). We might also

expect the intense 1008 cm^{-1} methyl rocking and 980 cm^{-1} hydrogen-out-of-plane (HOOP) wagging modes observed in prior Raman studies [69] to contribute to this oscillatory signal, the latter being unique to 3′-hECN in OCPO. The two peaks A_1 and A_2 are part of the same band, and decay with the S_2 lifetime, therefore are most likely due to stimulated emission rather than ground state bleach processes. They likely oscillate in phase due to the creation of ground-state wavepackets.

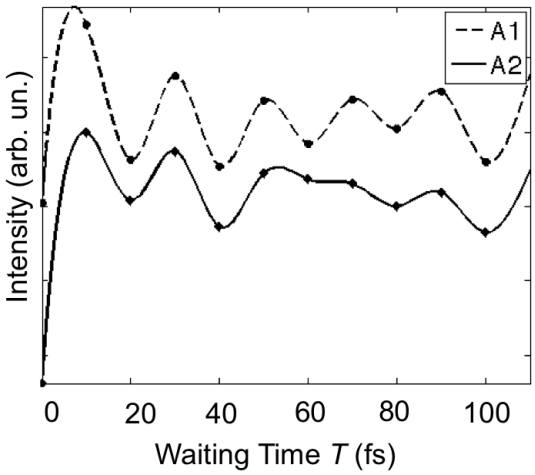

Figure 2.5: Evolution in time of the integrated intensity from the 2D spectra for regions centered at λ_t = 527 nm, labeled as A_1 and A_2 in Fig. 2.4 (b).

Even at early waiting times *T*, the A band (see Fig. 2.4) is well rounded, meaning it does not exhibit any diagonal elongation. This can be explained as a very fast randomization on the S_2 potential energy surface of molecules that unsuccessfully pass through the conical intersection with the S_1 state and are scattered in a range of trajectories [103, 104, 105].

At later times, the system undergoes ultrafast internal conversion to the S_1 state. A negative feature centered at λ_t = 550 nm (feature B, *T* = 7 ps spectrum in Fig. 2.4 (d)) appears, corresponding to $S_1 \rightarrow S_N$ ESA. The spectra at waiting times *T* larger than $\sim$ 2 ps show little evolution of the two main GSB/SE and ESA features. By 20 ps the signals have entirely decayed, corresponding to the complete relaxation of the population from S_1 to the ground state (spectra not shown).

At early times *T*, in the region of emission wavelengths between the GSB/SE and the ESA signals (emission wavelength between 535 and 565 nm), we observe the presence of additional positive and negative features, overlapping spectrally and evolving in time. This region is highlighted by a rectangular box in the *T* = 100 fs spectrum in Fig. 2.4 (c). This spectral region would be difficult to resolve or interpret in a 1D transient absorption experiment (which integrates over the excitation axis), as there are multiple overlapping signals of opposite sign arising from S_2, S_1 and possible contributions from other states such as S* [24, 6, 106, 107]. 2DES, however, can resolve the evolution of all these features and track them as a function of waiting time, *T*.

To understand the origin of these peaks, we refer to the rephasing and nonrephasing components of the early time spectra. Fig. 2.6 shows the rephasing and nonrephasing components of the T = 100 fs spectrum, with a rectangular box highlighting the spectral region of interest. The rephasing spectrum shows a similar pattern to the relaxation spectrum in the boxed region, with alternating positive and negative peaks, while in the nonrephasing component a single positive peak appears. The peaks are observable in the spectra for waiting times shorter than T = 1 ps (data not shown), longer than the S_2 lifetime [82]. A dispersive lineshape for crosspeaks in the rephasing component of 2DES spectra has been previously observed in both theoretical and experimental work [102, 108, 95]. This particular lineshape has been attributed to coupling of an electronic transition to a high frequency vibration. In 2DES experiments on β-carotene in solution, an analogous signal has been assigned to the population of a hot ground state via Impulsive Stimulated Raman Scattering (ISRS) [95]. Given the similarity in dynamics, lineshape and spectral position of the crosspeaks in our spectra, we propose that they arise from the formation of a wavepacket on the hot ground state.

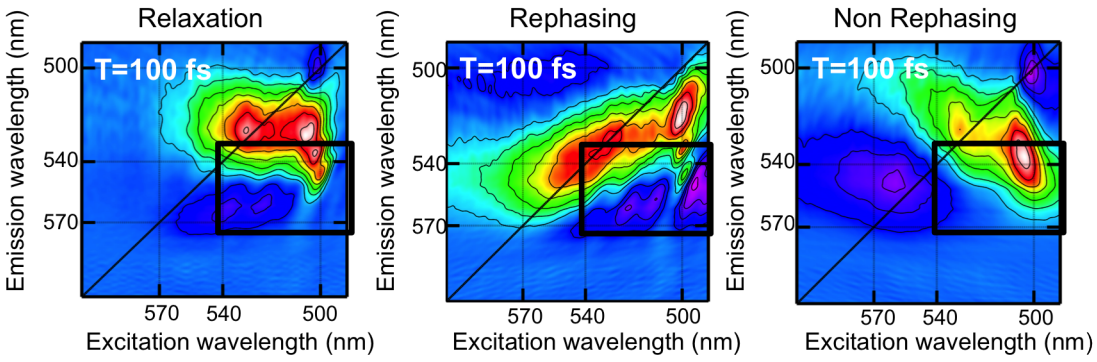

Figure 2.6: 2DES spectra of OCPO for T = 100 fs: relaxation, rephasing and non-rephasing components.

2D Electronic Spectroscopy of OCPR

Fig. 2.7 shows absolute valued 2DES spectra for selected waiting times T for OCPR at 77 K. Fig. 2.8 shows real-valued spectra for T = 30 fs and T = 7 ps [i]. The laser pulse excites the $S_0 \rightarrow S_2$ transition and a positive signal appears in the 2D spectra, corresponding to GSB/SE. After excitation, the S_2 population undergoes ultrafast internal conversion to the S_1 state, but the S_2 lifetime cannot be determined with precision. Due to the spectral position of our laser pulse, we are not able to observe the negative peak corresponding to the $S_1 \rightarrow S_N$ excited state absorption signal in our 2D spectra. This ESA signal is in fact red-shifted in OCPR and falls outside the bandwidth of our laser pulse [86, 82]. No additional features appear: the GSB/SE signal decays as the molecule relaxes back to S_0, and this relaxation is complete by 20 ps. The

[i] It was only possible to retrieve the phase factor from pump-probe data for 2DES spectra at select waiting times T, as shown in Fig. 2.8. For comparison, absolute-valued OCPO spectra are shown in the Supporting Information

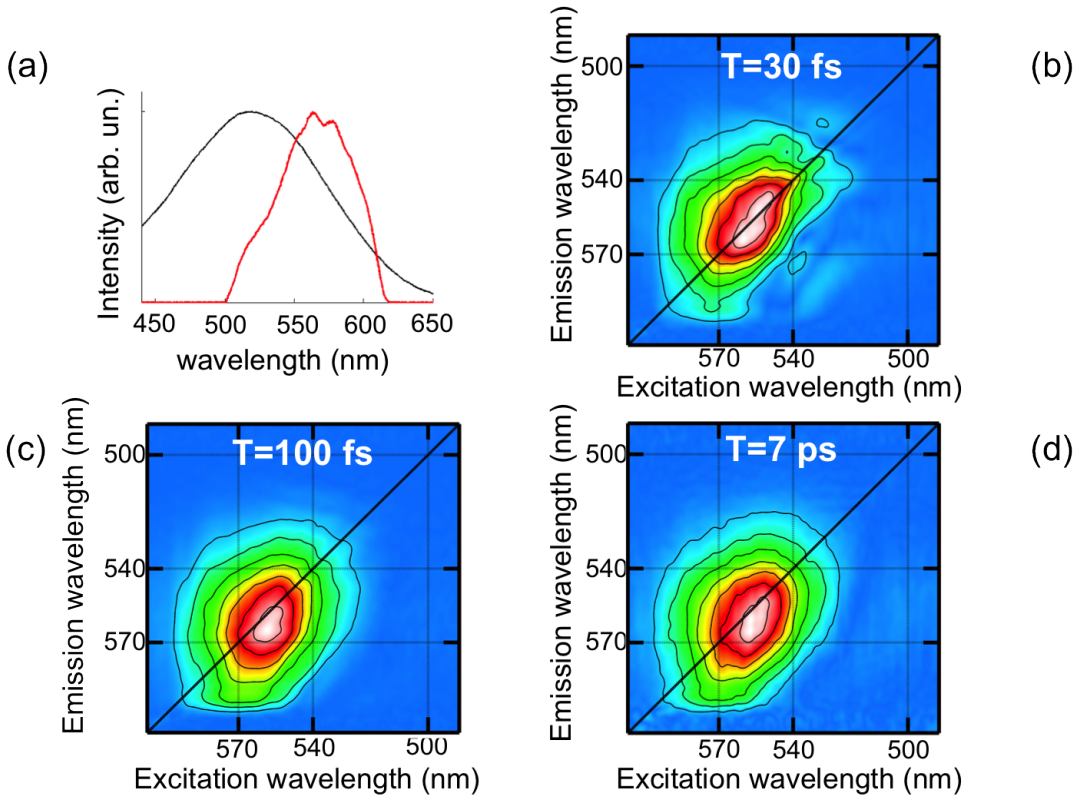

Figure 2.7: : (a) Linear absorption spectrum of OCPR at 77 K (black line) and laser spectrum used in the experiment (red line). (b),(c),(d) Absolute-valued relaxation 2DES spectra of OCPR for selected waiting times *T*.

OCPR 2D spectra are significantly different from the OCPO 2D spectra, being structureless, as well as exhibiting no evidence of vibrational wavepackets on S_2 nor signatures of ISRS between S_0 and S_2.

The shape of the 2D spectra for the red form can help elucidate the origin of the broad static lineshape observed in the absorption spectrum (see Fig. 2.3 (b)). The OCPR spectra have a pronounced diagonal elongation (see the T=30 fs spectrum in Fig. 2.8), suggesting the large contribution of inhomogeneous broadening.

2.3.4 Discussion

Linear absorption

The origin of the asymmetric broadening towards lower energies in the 283 K OCPO spectrum has been previously assigned to the stabilization of the ICT state common to carbonyl carotenoids [101]. Conversely, a more recent study by Polivka *et al.* [87] assigns this to ground state heterogeneity, assuming at room temperature the existence of a mixture of the two forms (OCPO, OCPR). Due to the observed reduction in asymmetric broadening at low

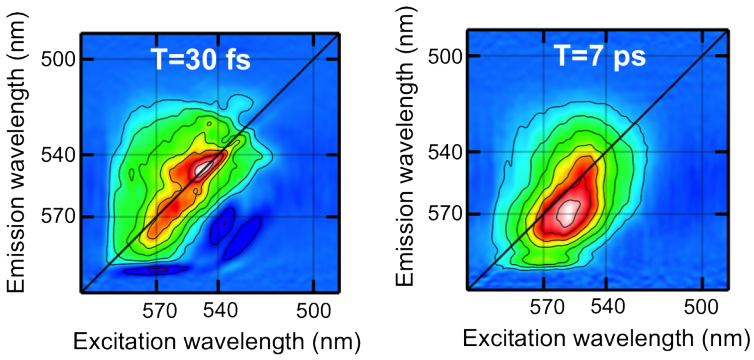

Figure 2.8: Real-valued 2DES spectra of OCPR for T = 30 fs and T = 7 ps.

energies in the 77 K versus the 283 K OCPO linear absorption, we believe that the low energy broadening in the 283 K spectrum could be caused by either the thermal population of low-frequency vibrational modes with energies lower than k_BT ($\sim$ 200 cm^{-1} at 283 K), or a distribution of conformers resulting from rotations about C-C bonds in 3′-hECN.

Concurrently, no narrowing is observed in the OCPR spectra upon lowering of the temperature. The static lineshape is highly broadened in this form even at 77 K. Interestingly, previous studies have shown that even upon absence of the C-terminal domain the shape and width of the spectrum is unchanged [109, 83]. This suggests that the origin of this particular lineshape is not highly dependent on the interactions between the C-terminal domain and the carbonyl group of 3′-hECN. Further investigation of the molecular origin of the static broadening will be provided in the discussion of the 2D results.

2D Electronic Spectroscopy

2DES allows us to compare 3′-hECN photophysics in OCPO versus OCPR, decongesting vibrational and electronic dynamics occurring on femtosecond to picosecond timescales over $\sim$100 nm bandwidth. Our ultrashort ($<$ 15 fs) pulses have allowed us to directly investigate with high time resolution the early time dynamics of 3′-hECN in the protein environment of OCP.

Vibrational activity is visible in both real and absolute-valued 2DES spectra of OCPO. Multiple vibrational modes are initially photoexcited on the S_2 state, and the action of ground state wavepackets persists for up to $\sim$1 ps. The 2DES results for OCPO resemble those obtained at cryogenic temperatures on β-carotene in a 2-methyl tetrahydrofuran glass [95]. OCPR, on the other hand, has no observable vibrational features and appears largely broadened, as expected from the linear absorption spectrum.

The precise molecular origin of the observed large inhomogeneous broadening requires further investigation. Conformational heterogeneity could play an important role if 3′-hECN is exposed to bulk solvent due to a loss of pigment-protein interactions attributed to the C-terminal domain of OCPO [83]. Solvent-induced broadening of the electronic absorption spectra of carbonyl carotenoids has previously been attributed to mixtures of conformational isomers preferentially formed in polar versus non-polar solvents [110, 111]. Exposure of

the carbonyl group of 3′-hECN to bulk solvent may create a distribution of conformers at the carbonyl-containing end ring (from s-*trans*, as in OCPO, to s-*cis*, as in solution [87]). Additionally, fluctuations in the electrostatic environment of the chromophore produced by an ensemble of protein conformations or differences in H-bonding interactions with amino acids or water molecules could create a distribution of 0-0 energies that could further broaden the absorption spectrum in this form. Further experiments on OCP reconstituted with non-carbonyl carotenoids (such as β-carotene or zeaxanthin) and lacking the C-terminal domain could help disentangle these different possible contributions to the inhomogeneous broadening.

Our 2DES data on isolated OCP do not provide evidence for a direct role of 3′-hECN in OCPR-based quenching. We do not, for example, observe any significant shortening of the S_1 lifetime in OCPR vs. OCPO, consistent with the results in [82]. And while it is generally accepted that 3′-hECN plays a direct role in the quenching process [85, 112], the precise mechanism by which excess energy is dissipated remains under debate. 3′-hECN could play a direct role via energy- or charge-transfer [85, 82], or the OCPR complex could act allosterically to initiate quenching within the phycobilisome in analogy to the mechanism proposed for zeaxanthin in plant nonphotochemical quenching by Horton *et al.* [113]. Polivka *et al.* [87] recently determined only a small energetic advantage for the S_1 state of 3′-hECN in OCPR versus OCPO relative to the phycobilisome bilin S_1 state. We are not able to observe signatures of the ICT state in our data, due to the bandwidth of the laser pulse used, so we cannot make conclusions on the enhancement of the ICT character for 3′-hECN in OCPR nor draw conclusions regarding its potential involvement in a quenching mechanism. Our data does, however, provide insight into the perturbed local environment provided by the protein pocket in OCPO and OCPR.

Interestingly, it has not been conclusively demonstrated that the 4-keto-β-ionylidene ring, nor the ICT state resulting from the presence of the conjugated carbonyl group, is necessary for quenching activity in an OCP-phycobilisome complex. Could the presence of the 4-keto group be more strictly required for photoactivity rather than quenching activity? OCP is a photoswitch and the unique photochemistry of 3′-hECN in OCPO must be responsible for driving structural changes in the protein that ultimately lead to formation of the OCPR form, binding of OCP to the phycobilisome, and induction of the quenching mechanism. It is known that interactions between the 4-keto group and absolutely conserved residues in the C-terminal domain (Y203 and W290) are strictly required for OCP photoactivity [84, 114]. While a relevant modulation of 3′-hECNs conformation(s) and/or photophysical properties in the OCPR form certainly may occur in the context of quenching activity, we must also consider the possibility that the photophysical properties of OCPR's 3′-hECN chromophore *in vitro* could simply arise as a secondary consequence of other mechanistically critical changes in protein structure and chromophore solvent accessibility that occur during the photochemical mechanism and allow OCP to bind to the phycobilisome. Further studies of the quenching complex formed by OCP bound to the phycobilisome antenna [68] are clearly needed to elucidate the specific nature of the quenching mechanism.

2.3.5 Conclusions

Here we have presented 2DES results comparing the excited state dynamics of 3′-hECN in OCPO and OCPR. The study investigates the photophysics of a carbonyl carotenoid in two different electrostatic environments following photoconversion of the OCP holoprotein. Our results show resolvable and rich vibrational dynamics in OCPO, consistent with the carotenoid being held in a tightly locked conformation by the protein environment, with consequences for the photoactivity of this form. OCPR, on the other hand, shows a highly inhomogeneously broadened behavior. The origin of this large inhomogeneous broadening can be attributed to conformational heterogeneity due to exposure of the pigment to free solvent or to variations in the electrostatic environment experienced by the carotenoid. Further studies targeted to the investigation of the specific pigment-protein interactions in the C-terminal domain of OCP should help elucidate the role of the carbonyl group and the protein environment in tuning OCP photochemistry.

2.3.6 Supporting Information

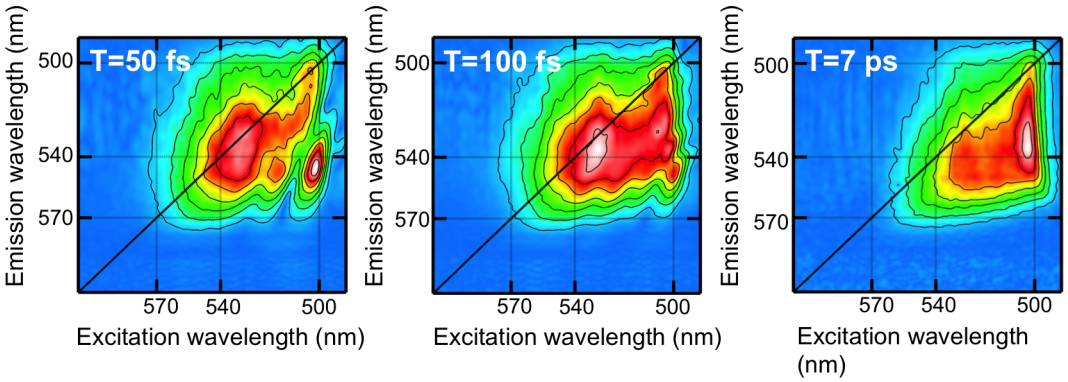

Figure 2.9: (a) 2DES absolute-valued spectra of OCPO for the waiting times of Fig. 2 (T = 50 fs, 100 fs and 7 ps)

2.4 Transient Absorption results on OCP

In order to better investigate the structural and spectroscopic differences between the two conformations of OCP, we have performed transient absorption experiments on OCPO and OCPR at 77 K. These experiments are complementary to the 2DES results presented in the previous section. In fact, transient absorption provides better resolution on the decay kinetics than 2DES, but worse spectral resolution, since there is no resolution over the excitation axis. Additionally, the longer pulses produced by the OPA offer worse time resolution, but better selective excitation, and transient absorption gives a broader probe bandwidth than 2DES, due to the supercontinuum light used as probe.

In particular, we are interested in investigating the role of the intramolecular charge transfer state of 3′-hECN in the two forms of OCP. Such state appears in the electronic structure of carotenoids containing a carbonyl group, which π-conjugates with the carotenoid backbone, thus changing the symmetry of the system and the energy level structure [115, 116]. Carbonyl carotenoids, such as 3′-hECN, are the most abundant Cars in nature (see Fig. 2.3 (a) for the structure of 3′-hECN in OCP). Their behavior is highly dependent on their environment [115], therefore we might expect to observe different photophysics associated with the ICT state in the two forms of OCP since the protein environment is different, as we have suggested in the previous Section. ICT states play an important role in energy transfer (i.e. in the peridinin-chlorophyll *a* protein complex [117] and in an artificial carotenoid-phtalocyanine dyad [118]), so the role of the ICT state in OCP might be relevant for its biological quenching function.

In OCP, the ICT state in stabilized by the protein environment, since the carbonyl group is *s-trans* with respect to the conjugated backbone [101] and it is hydrogen-bonded to the protein. However, in the related Red Carotenoid Protein (RCP), an OCP lacking the C-terminal and with absorption almost identical to that of OCPR [83], no signature of the ICT state has been detected [109], suggesting the importance of the bonding to the protein pocket in enhancing the ICT characteristics.

The carbonyl group of 3′-hECN plays potentially a very important role in the photoactivity capabilities of OCPO versus OCPR (see Section 2.3). Moreover, Berera *et al.* [86, 82] proposed that the ICT state plays an important role in energy dissipation in OCPR. On the basis of transient absorption results at room temperature and at 77 K, the authors proposed that the ICT state in OCPR acts as mediator in the quenching process, accepting excitation energy from the bilin S_1 state and partly decaying to the ground state (on a 0.6 ps timescale) and partly to the S_1 state (which recovers to the ground state with a 3.2 ps lifetime).

The details of the experimental apparatus used for our transient absorption experiments are described in Section 1.4.2. Briefly, the pump pulses were generated in an optical parametric amplifier pumped by a Ti:sapphire laser system. The visible pulses were centered at 520 nm for both OCPO and OCPR experiments, with 12 nm FWHM and compressed to a duration of 60 fs with prisms. The energy at sample position was approximately 10 nJ. The probe is white light obtained via supercontinuum generation in a 2 mm sapphire crystal. The visible portion of this supercontinuum (450 - 800 nm) was selected via use of a lowpass filter (SPF750) before the sample. The sample was contained in a 200 μm cuvette in an optical cryostat (Optistat, Oxford Instrument) and cooled down to 77K. The details of the sample preparation are the same as described in Section 2.3.

Figure 2.10 shows spectrally resolved transient absorption data for OCPO at 77 K upon excitation of the 0-0 transition of the $S_0 \rightarrow S_2$ transition of OCPO (black solid arrow in Fig. 2.11 (b)). The ΔOD is shown as a function of the probe delay (horizontal axis) and the probe wavelength (vertical axis). The data has been manually corrected for the chirp in the white light probe. Horizontal traces of the two dimensional map at selected probe delays are shown in Figure 2.11 (a). We can observe the appearance of three main bands in the signal, labeled as A, B and C in both the two dimensional map and the spectra. Band A has a negative sign and appears immediately at time zero. It extends spectrally from 500 nm to

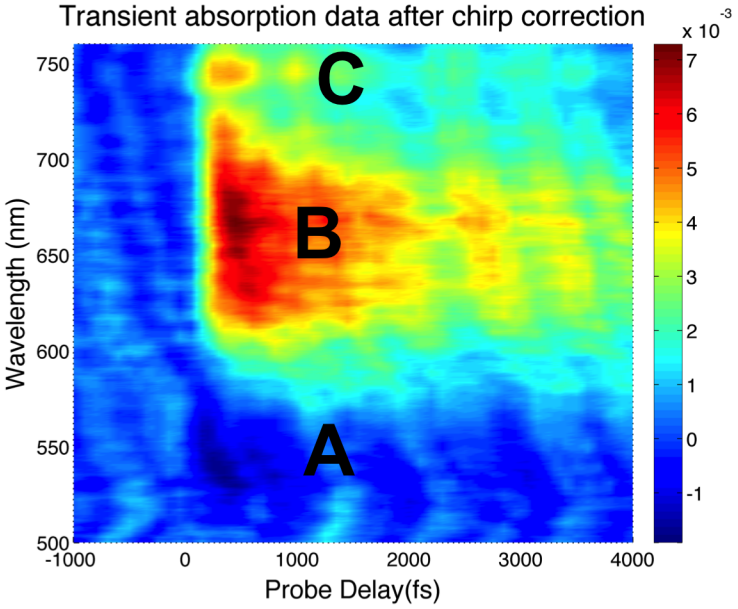

Figure 2.10: Spectrally resolved transient absorption data for OCPO at 77K. The ΔOD is plotted as a function of the time delay between pump and probe pulses (horizontal axis) and the probe wavelength (vertical axis). Horizontal slices of the map represent kinetic traces at selected probe wavelengths, while vertical slices represent transient absorption spectra at selected pump probe delays. Positive signals correspond to excited state absorption transitions, while negative peaks correspond to bleaching/stimulated emission transitions (see Section 1.4.2 for a more detailed explanation) The physical origin of bands A, B and C is discussed in the text.

570 nm. As time progresses, the A band blue-shifts due to the grow-in of the band B, with opposite sign. We assign the origin of band A to bleaching/stimulated emission of the $S_0 \rightarrow S_2$ transition. Band B is positive, and starts being populated around $\sim$ 100 fs, reaching its maximum around 500 fs. Band B extends spectrally between $\sim$ 580 nm and 720 nm. We assign the origin of this band to excited state absorption from the S_1 state to higher lying S_N states, upon relaxation of S_2 to S_1 (shown in Fig. 2.11 (b) as a black thin line). This explain also the blue-shift of the maximum of band A with time: as S_2 relaxes into S_1, vibrational relaxation into the S_1 potential surface happens on a $\sim$ 500 fs - 1 ps timescale.

Band C appears on the same timescale as band B, with lower intensity, and decays on a similar timescale. It extends spectrally between 725 nm and 800 nm (the CCD is sensitive up to 750 nm, but data collected on a photodiode confirms that this band in fact extends to wavelengths higher than 750 nm).[ii]. We assign the origin of this peak to the excited state absorption of the ICT state of 3′-hECN to a higher lying state, labeled as $S_{N'}$. Figure 2.11 (b) shows the ICT state as part of a S_1/ICT state (as suggested by the kinetics similar to the ones observed for S_1) [115, 86, 82], and it is possible that $S_{N'}$ is part of the same S_N manifold, if the symmetry of the S_1 and S_1/ICT states is not significantly different. It is also possible that the ICT state is a separate state absorbing to the same S_N manifold, but this data does not

[ii]Due to the filter used in our experiment, we have no indication whether this band extends above 800 nm into the NIR

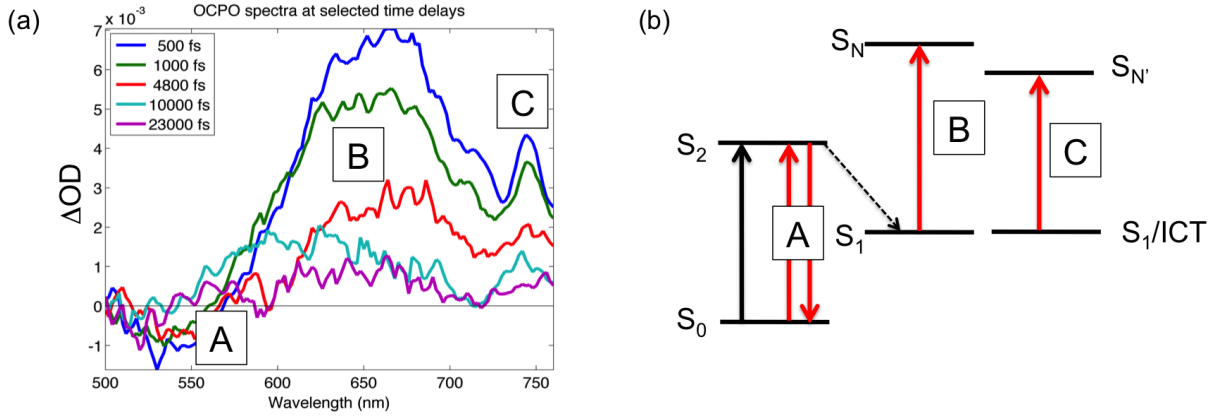

Figure 2.11: (a) Vertical traces from the two-dimensional map of Fig. 2.10 at selected probe delays. The three main features shown in Fig. 2.10 are reported on the spectra as well. (b) Energy level scheme for 3′-hECN in OCPO and main transition observed in the TA data. The physical origin of transitions A, B and C is explained in the text.

allow us to distinguish between the two possibilities, and the similar kinetic suggest instead a mixed state.

Wavelength-specific data collected on a photodiode connected to a lock-in amplifier (see Fig. 2.14 in Section 2.4.1 for the measured traces with corresponding kinetic fits) allows us to determine the kinetics of the various transitions. At 520 nm (A band), the maximum of the GSB/SE region, we observe a biexponential decay, with decay constants of 1.7 ps and 6.3 ps. These two components correspond very closely to the decay components at 640 nm (part of the ESA band B), which are approximately 2 ps and 8 ps. The similarity in decay of the two transitions suggest that the ground state recovers with two time constants, as both the S_2 bleach and the S_1 state recovery occur with similar time constants. At 580 nm we are able to observe population of the S_1 state, upon relaxation of S_2. The fit of the kinetic trace at this wavelength gives a rise time of approximately 200 fs, followed by a decay with a time constant of approximately 9 ps. We can assign the shortest lifetime to the relaxation of S_2. This is in agreement with the results we have obtained from 2DES (see previous Section). Fits of kinetic traces in the C band (between 730 and 800 nm) show two main components of decay, of $\sim$ 1 ps and $\sim$ 6 ps (see 755 nm decay in Fig. 2.14), shortening to approximately 500 fs and 5 ps at lower energies (775 nm, data not shown). The rise time at 775 nm is shorter with respect to 640 nm (below 100 fs), suggesting that the ICT state might be populated before the S_1 state upon S_2 relaxation. Since the lifetimes of rise/decay correspond very closely between bands B and C, we suggest that our results confirm what proposed previously by Berera and coworkers [86, 82]: the S_1 and ICT state form a mixed excited state S_1/ICT. Band B has dominant S_1 character, while band C has dominant ICT character, which explains why band C is populated right after time zero, and decays on a slightly shorter timescale than band C.

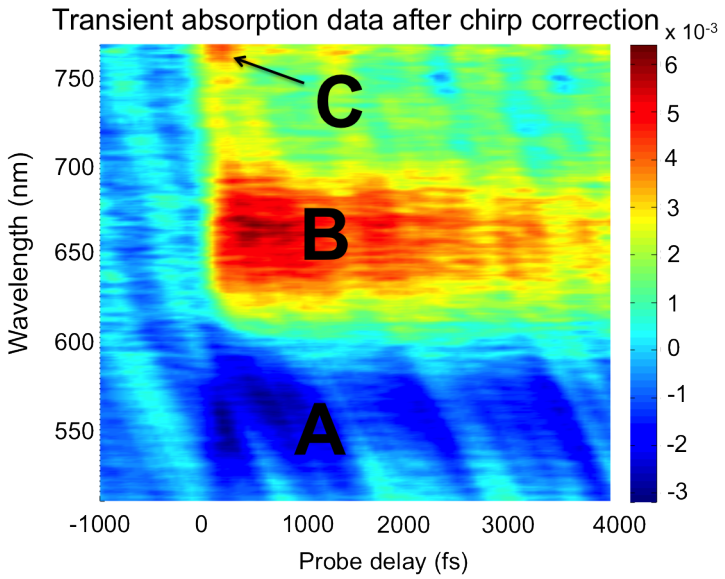

Figure 2.12: Spectrally resolved transient absorption data for OCPR at 77K. The ΔOD is plotted as a function of the time delay between pump and probe pulses (horizontal axis) and the probe wavelength (vertical axis). Horizontal slices of the map represent kinetic traces at selected probe wavelengths, while vertical slices represent transient absorption spectra at selected pump probe delays. The color bar is as in Fig. 2.10. The physical origin of bands A, B and C is discussed in the text.

Fig. 2.13 shows spectrally resolved transient absorption data for OCPR at 77K upon excitation of the maximum of the $S_0 \rightarrow S_2$ transition. Vertical traces from the map, showing the transient absorption spectra at selected probe delays, are shown in Figure 2.13 (a). The two main transitions are indicated as A and B in the Figures. Upon population of S_2, we observe the appearance of a ground state bleach/stimulated emission signal (band A) between S_0 and S_2, which extends between 500 nm and 600 nm. The maximum of this band is around 560 nm, and the decay occurs with a time constant of $\sim$ 6 ps (see Fig. 2.15 in the Appendix for time traces of OCPR with the corresponding fits). Data collected on a Si photodiode at 540 nm gives a biexponential decay (see Fig. 2.15, top left): the shorter component ($\sim$ 230 fs) can be assigned to decay of SE from S_2 as it relaxes to S_1, while the longer component ($\sim$ 4.7 ps) can be assigned to ground state recovery. As in OCPO, we observe a blue shift over the first $\sim$ 1000 fs of band A, due to overlap with band B. Band B extends between 600 and 700 nm and its origin can be assigned to the ESA between S_1 and S_N (see Fig. 2.13 (b)). The maximum of this band is around 650 nm, and fitting the decay trace at this wavelength (Fig. 2.15, bottom left) gives a rise time of less than 100 fs, and a decay constant of $\sim$ 5 ps (ground state recovery). The rise time can be assigned to population of the S_1 state as the S_2 state relaxes. As in OCPO, this rise time is very short, suggesting a very short excited state lifetime of S_2 in the red form as well.

In the two dimensional map in Fig. 2.13, we can observe the presence of a third feature (labeled as C), starting around 760 nm. Due to the limited bandwidth allowed by the CCD, we are not able to fully characterize its time evolution or its spectral extension . However,

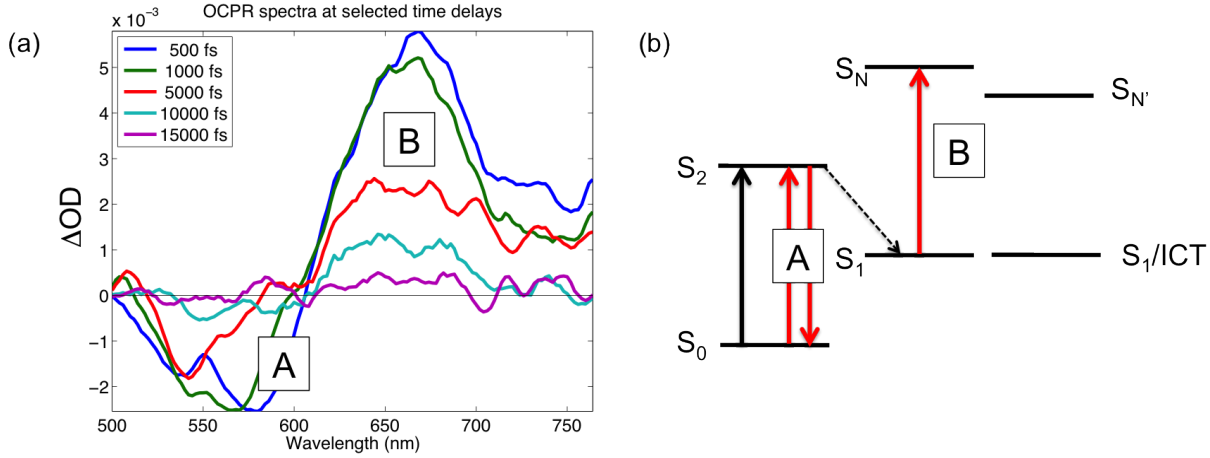

Figure 2.13: (a) Vertical traces from the two-dimensional map of Fig. 2.12 (smoothed data) at selected probe delays. Features A and B of Fig. 2.10 are reported on the spectra as well. (b) energy level scheme for 3′-hECN in OCPR and main transitions observed in the TA data.

we can hypothesize its assignment to the ICT state, in analogy to what observed in OCPO. A fit of the time trace at this wavelength is shown in Fig. 2.15, bottom right. The rise time is below 100 fs, while the decay occurs on a 4 ps timescale. Analogously to OCPO data, we observe shorter lifetimes for band C with respect to band B, confirming that this signal is due to excited state absorption from the S_1/ICT state, with more pronounced ICT character.

A comparison of the photophysics of 3′-hECN as measured by transient absorption in the two forms of OCP does not reveal significant differences. The signals observed are similar, if not red-shifted for OCPR, as expected from the linear absorption. Both forms show signals that can attributed to the ICT state of the carotenoid. However, we cannot make conclusions about the relative importance of this state in the two forms of the PPC. Since we do not have kinetic traces for wavelengths above 760 nm for OCPR, we are not able to fully characterize the strength ICT transition for this form. It would be valuable to extend these measurements to cover that spectral region. A comparison between OCPO and OCPR ICT transitions could help elucidate the role played by the carbonyl group in the biological function of the two forms. In fact, the intensity of the ICT-like transition is an indicator of the charge-transfer character of the S_1/ICT state [119].

If we assume the hypothesis of an ”open” conformation in OCPR, with reduced interactions at the C-terminal (presented in the previous Section and proposed by [62, 83],), then we would expect to observe a reduced contribution of the ICT state in OCPR. In fact, the carbonyl group in this form is more solvent exposed, as expected from the large inhomogeneous broadening observed in the linear absorption and 2DES spectra for OCPR, producing a large heterogeneity in the conformations of the carbonyl-containing end ring (see Section 2.3). In combination with the fact that in solution (where the carbonyl group is s-*cis* with respect to the backbone) [101] and in RCP (which lacks the C-terminal) [109] there is no signature of an ICT state, this indicates that we should observe a reduced contribution from this transition in the transient absorption spectra. What we observe is that the broadness of the excited state

absorption band is narrower in OCPR versus OCPO (compare bands B and C in the two dimensional maps of Figs. 2.12 and 2.10, respectively), which could indicate a weaker mixing of the ICT and S_1 states in this form. In this case, we could hypothesize an important role for the carbonyl group and its interaction with the protein pocket in the photoactivity of the OCPO form. A reduced contribution of the ICT state in the red form would then be expected, as this form is not photoactive. Additional experiments, extending the probing of OCPR to the near infrared, are needed to confirm or refuse this hypothesis. Additionally, transient absorption experiments in phycobilisome-bound OCPR versus phycobilisome-bound RCP proteins binding non-carbonyl carotenoids[iii] would be needed to elucidate whether the ICT state plays a role in excess energy dissipation.

2.4.1 Appendix

Figures 2.14 and 2.15 show the transient absorption traces recorded on a Si photodiode connected to a lockin amplifier for OCPO and on a Si photodiode and CCD camera for OCPR, respectively, at 77 K. The 95% confidence intervals are shown in square parenthesis next to the corresponding fit parameter.

[iii]The carbonyl group is, in fact, essential for photoconversion, and RCP resembles very closely OCPR (the linear absorption spectra are identical) [83].

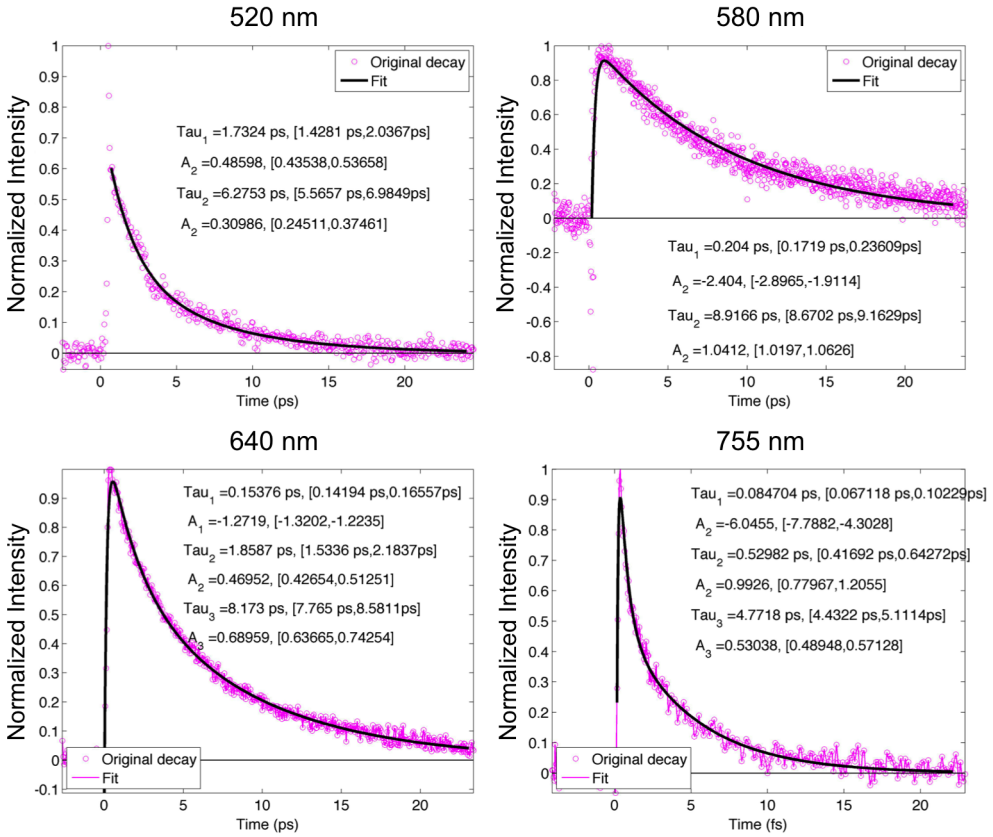

Figure 2.14: Normalized kinetic traces of decay of OCPO at 77 K at selected wavelengths (data points are indicated by magenta circles) with corresponding fits (solid black line). The 95% confidence intervals are indicated in parenthesis next to the fit results. The decay at 520 nm has negative amplitude since it corresponds to the ground state bleach/ stimulated emission transition indicated as A in Fig. 2.11 (b). The decays at 580 and 640 nm are part of the excited state absorption indicated as B, while the 755 nm decay is part of the C excited state absorption band.

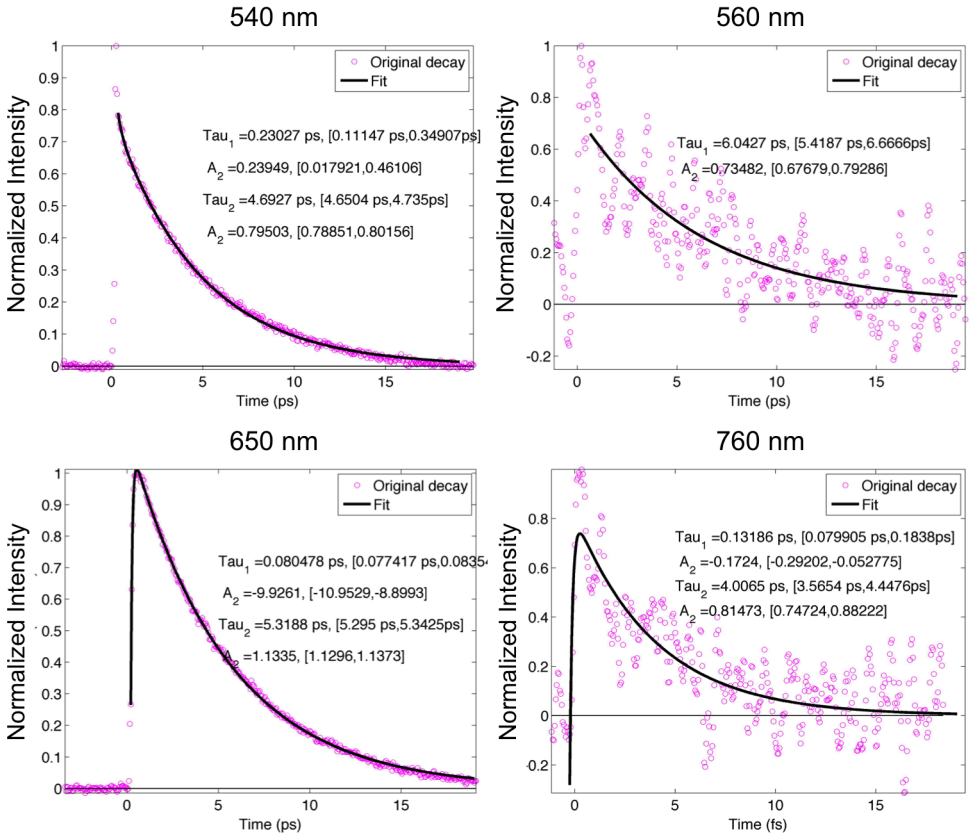

Figure 2.15: Normalized kinetic traces of decay of OCPR at 77 K at selected wavelengths (data points are indicated by magenta circles) with corresponding fits (solid black line). The 95% confidence intervals are indicated in parenthesis next to the fit results. The decays at 540 and 650 nm have been recorded on a Si photodiode connected to a lockin amplifier, while the traces at 560 and 760 nm have been obtained as horizontal traces of the two dimensional map shown in Fig. 2.12. The decay at 540 and 560 nm have negative amplitude since they correspond to the ground state bleach/ stimulated emission transition indicated as A in Fig. 2.13 (b). The decay at 650 nm corresponds to the excited state absorption signal indicated as B, while the 760 nm decay is at the blue edge of the excited state absorption band C in Fig. 2.12.

2.5 Conclusions

This Chapter presents 2DES and transient absorption experiments on the two forms of OCP, a single-carotenoid binding PPC involved in cyanobacterial photoprotection. As a summary of the experimental results, these are the main points known about OCP-NPQ and the hypothesis on the role played by OCP in cyanobacteria.

- The model for OCP-NPQ consists of three states [70] (see Fig. 2.2): 1) OCPO is the dark form, which can convert to 2) OCPR upon excess blue-green light absorption. 3) OCPR can bind to the phycobilisome antenna and quench excitation energy.
- The configuration of OCPO is such that it does not bind to the phycobilisome.
- The temperature-dependence of OCP photoactivation remains an open question. NPQ in cyanobacteria is temperature independent according to [61]. However, the rate of formation of quenching complexes depends on temperature according to Fig. 7 in [70]. It is possible that the overall NPQ is temperature-independent, but the kinetics of photoactivation/formation of quenching complex depend on temperature.
- We propose that the conversion OCPO-OCPR is continuous upon light absorption and we have an equilibrium population of OCPO and OCPR even at room temperature.
- We hypothesize that increased temperature increases the probability of OCPR docking to the phycobilisome antenna, as it can find a binding configuration faster.
- For incident red light, or for low light levels, OCP does not photoconvert and therefore does not dock to the phycobilisome. This fact, together with the particular structure of OCPO (with the carotenoid tightly bound to the protein and minimally solvent-exposed), suggests that OCP does not play a role in light harvesting.
- The current hypothesis in the literature is that, upon formation of the quenching complex OCPR+phycobilisome, energy is dissipated via energy transfer from the Qy state of the bilin pigment in the phycobilisome core to the S_1/ICT state of the carotenoid in OCP [86, 82].

In order to gain insight into the molecular mechanism of quenching by OCPR, it would be interesting to look at the phycobilisome-OCPR complex, as mentioned at the end of Section 2.3. Due to the overlap between OCP signals and phycobilisome absorption, the spectral resolution over the excitation axis offered by 2DES has the potential to elucidate which dissipative pathways turn on upon selective excitation of the carotenoid or of the phycobilisomes in quenching (OCPR) and non-quenching (OCPO) conditions. Additionally, data analysis techniques such as global and target analysis would be required to elucidate these dissipative pathways [120, 121].

In conclusion, OCP is a very interesting PPC under multiple aspects. 1) OCP is a minimal system, composed of a single carotenoid in a protein pocket, and we have shown that it

is possible to directly investigate the role of pigment-protein interactions in tuning the photophysics and spectral properties of its pigment. 2) It has evolutionary importance since it combines the function of light sensor and, possibly, of quencher, which are performed by different PPCs in higher plants. 3) It undergoes a conformational change upon excess light absorption, which seems common to various photosynthetic organisms upon induction of flexible NPQ (see Chapter 4 for a more detailed discussion).

Chapter 3

The Bacterial Reaction Center

Contents

3.1 Introduction

Purple bacteria are a class of anoxygenic photosynthetic organisms which have been extensively studied biochemically, structurally and spectroscopically, making them the most well-understood photosynthetic organism in terms of energy and electron transfer processes [4]. The primary photosynthetic structure for most purple bacteria is the *chromatophore*, a lipid vesicle of 30-60 nm diameter [122] which contains embedded the main light harvesters (LH1 and LH2), the reaction center (RC) and other important photosynthetic components.

LH1 and LH2 are both integral membrane antenna complexes (see Fig. 3.1) which are responsible for light absorption and efficient energy transfer to the RC. Both LH2 and LH1 have a characteristic ring structure. Energy is absorbed in the LH2 and LH1 rings and transfers downhill energetically to lower lying states in LH2 and to LH1 on a 1 ps and 3 ps timescale, respectively. LH1 surrounds the reaction center and energy transfer between LH1 and the RC occurs in $\sim$ 35 ps (see Figure) [4, 123].

The bacterial reaction center is the best characterized photosynthetic reaction center in terms of its structure, energy and electron transfer dynamics. Unlike the structure of antenna

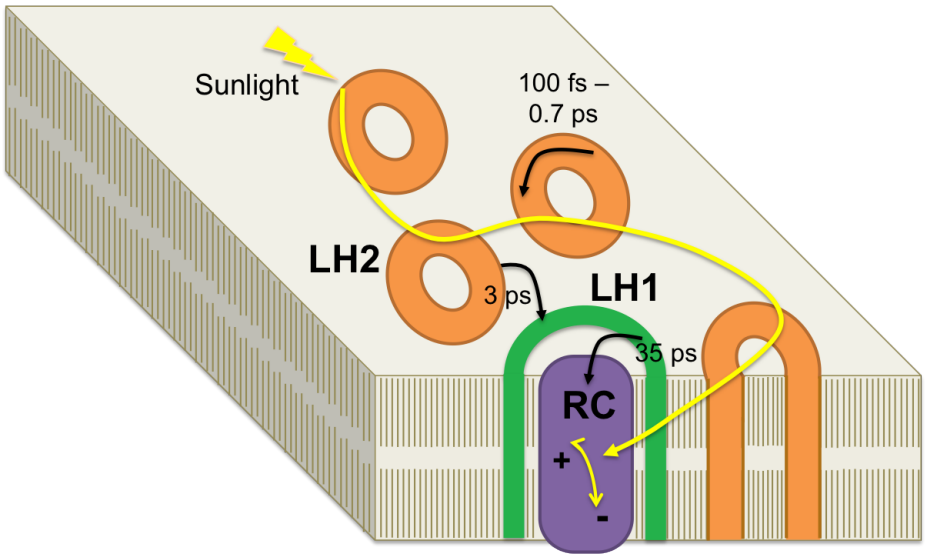

Figure 3.1: Cartoon of the photosynthetic apparatus of purple bacteria, showing the transmembrane antenna complexes LH2 (orange disks), LH1 (green disk) and the reaction center RC (purple) in the lipid membrane. The main energy transfer timescales are indicated in the figure and taken from [123].

systems, the structure of reaction centers is highly conserved across species, therefore the bacterial reaction center is a good model for the functionality of this type of PPC.

Fig. 3.2 shows the structure of the bacterial reaction center (the protein scaffold is in grey, to highlight the pigment composition and arrangement). The bRC was the first PPC for which a crystal structure was obtained [124]. The bRC has a quasi-symmetrical structure with two branches, A and B. Each branch is composed (going downhill energetically and uphill structurally) by a Quinone (Q), a Bacteriopheophytin (BPh, H in the Figure), an accessory Bacteriochlorophyll (BChl, B in the Figure). The two branches reunite at the special pair (P870, named after the absorption maximum of their Q_y transition), composed of two strongly coupled Bacteriochlorophylls. The special pair excited state loses an electron and forms the primary ion state in the chain of electron transfer processes. Branch A also contains a *cis* carotenoid [125] to the side of the accessory Bacteriochlorophyll B_B, usually spheroidene or neurosporene.

Energy transfer occurs along both branches A and B, going downhill energetically from the BPh to the BChl to the special pair. H to B energy transfer has been measured to take < 100 fs [126] (~ 240 fs from calculations [127]), while B to P energy transfer takes 100 - 200 fs (experimentally measured to take 180 fs in [126], 124 fs in [128], and calculated as 164 fs in [127]). The carotenoid can also harvest excitation energy and transfer to the BChl, even though it is thought that its main role is photoprotection, as will be discussed in the following.

While energy transfer occurs along both branches, electron transfer has been shown to occur only along the A branch. Fig. 3.2 shows the main electron transfer pathways (black arrows) overlaid to the structure of the bRC, with their relative timescales. The observation

of this asymmetry in electron transfer has been made possible by the fact that the two BPhs have different spectral signatures for their Q_x transitions due to slightly different protein environments. Upon excitation of the special pair, the excited P870* state decays losing an electron to form $P870^+$. A new state is formed ($P870^+BPh_A^-$) and the electron is transferred to the BPh on the A branch (an intermediate, short lived $P870^+BChl_A^-$ state is also formed). The electron is then transferred to Q_A in 200-300 ps, and to Q_B in $\sim$ 200 μs. All of these steps, except the last transfer between the two quinones, are independent of temperature. The electron on the special pair is replenished by a cytochrome in a reaction that takes a few hundred nanoseconds, much longer than the time required to transfer energy from the antenna or the other RC pigments. Until this occurs, the reaction center is closed and the primary donor is oxidized.

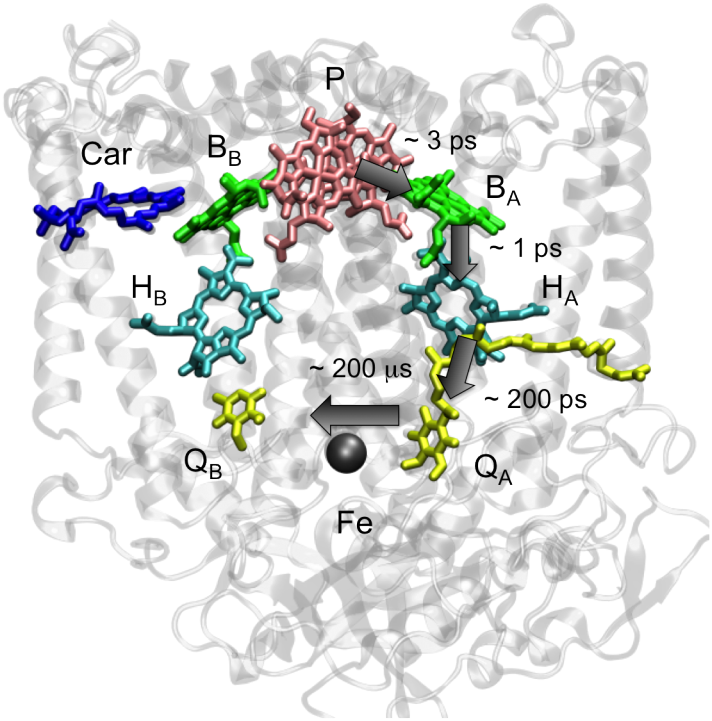

Figure 3.2: Pigment composition, structure and electron transfer dynamics for the bRC. The protein scaffold is shown in gray. The structure has two quasi-symmetric branches A and B. P = special pair; B_A, B_B = Bacteriochlorophyll; H_A, H_B = Bacteriopheophytin; Q_A, Q_B = quinone; Fe = non-heme iron. The main electron transfer steps (black arrows) and their associated timescales at room temperature [4, 129] are shown on the structure as well.

The carotenoid plays a very important role in the case of closed reaction centers. In fact, while the carotenoid is not essential to the electron transfer processes [26], it can quench the triplet state of the special pair. If the quinone is oxidized, or otherwise unavailable to accept an electron from the BPh, a back reaction can take place, which leads to the formation of a triplet state of the special pair. This has been observed in carotenoidless mutants of the bacterial reaction center [130]. For carotenoid-containing reactions centers, instead, a

Car triplet state quenches directly the special pair triplet state as it is formed [131], thus preventing the potential formation of damaging singlet oxygen species (see Section 1.3).

The unidirectionality of the electron transfer reactions is ensured by the fact that the backward rates are 50 times slower [4], making the bRC very robust in terms of efficiency of electron transfer. However, the molecular origin of this asymmetry in the rates and the reason for which electron transfer occurs only along one of the two branches are not understood yet.

In this Chapter, I will present two dimensional electronic spectroscopy experiments performed on the bacterial reaction center from *Rhodobacter sphaeroides*. The experiments address the following questions:

- Investigate the energy level structure that causes the functional asymmetry between the two branches (both active in energy transfer, only one active in electron transfer). The linear absorption spectrum of the bRC (see Fig. 3.3 (b)) contains overlapping transitions from the two branches. We are interested in learning how the overlapping states of the A and B branches are different in terms of energy levels and dynamics.

- Elucidate the ultrafast energy transfer dynamics occurring over broad spectral regions. We have discussed in previous Chapters the importance of the interplay between Chl and Car for energy transfer and energy dissipation. We want to investigate the strength of the coupling between the Car and the BChl in the bacterial reaction center, and what the possible pathways and timescales of energy transfer are between the Car and B_B.

Section 3.2 will present the results of 1-color 2DES experiments on the bacterial reaction center from *Rhodobacter sphaeroides*. Probing of the B band reveals for the first time a spectroscopic signature of the two accessory BChl in the B band of the bRC, and of ultrafast energy transfer between them. In Section 3.3 we present a powerful experimental technique, 2-color 2DES, which allows us to elucidate ultrafast energy transfer dynamics occurring over broad spectral ranges. We apply this technique to the bRC: excitation of the Car region (around 500 nm) is followed by monitoring of the evolution of the energy transfer to the B region. This represents the first example of a fully non collinear two color 2DES experiment.

3.2 2D electronic spectroscopy of the B band of the bRC

Abstract

Photosynthetic organisms convert photoenergy to chemical energy with near-unity quantum efficiency. This occurs through charge transfer in the reaction center, which consists of two

branches of pigments. In bacteria, both branches are energy-transfer pathways, but only one is also an electron transfer pathway. One barrier to a full understanding of the asymmetry is that the two branches contain excited states close in energy that produce overlapping spectroscopic peaks. We apply polarization- dependent, 2D electronic spectroscopy to the B band of the oxidized bacterial reaction center. The spectra reveal two previously unresolved peaks, corresponding to excited states localized on each of the two branches. Furthermore, a previously unknown interaction between these two states is observed on a time scale of $\sim$ 100 fs. This may indicate an alternative pathway to electron transfer for the oxidized reaction center and thus may be a mechanism to prevent energy from becoming trapped in local minima.

In photosynthesis, absorbed sunlight is converted to chemical energy with near-unity quantum efficiency [4, 132]. After absorption, which occurs primarily in the antenna complexes in the outer regions of the photosynthetic apparatus, the excitation energy is transferred to a central location, the reaction center. In the reaction center, an initial charge separation event occurs, which initiates a subsequent chain of electron-transfer reactions [133, 134]. The antenna complexes and the reaction center are pigment protein complexes (PPCs), which consist of densely packed pigments surrounded by a protein matrix. Although antenna complexes exhibit a large amount of architectural and size diversity [135, 136, 137, 138], the molecular structure of the reaction center is highly conserved across species [139]. The bacterial reaction center (bRC) is an ideal model system for studying the functionality of reaction centers because it has been extraordinarily well-characterized by numerous spectroscopic techniques, biochemical experiments, and structural studies [4, 134]. The bRC consists of two branches of chromophores, called A and B, that are arranged with pseudo-C_2v symmetry (shown in Figure 3.3 (a)). Each branch contains two bacteriochlorophylls (BChl), a bacteriopheophytin (BPheo), and a quinone (Q), with a carotenoid found next to the B branch [4, 139, 140]. The linear absorption spectrum, shown in Figure 3.3 (b), exhibits a series of well-separated peaks. Most of these peaks contain two states, one from each of the two branches. The two branches are structurally similar, and both serve as efficient energy-transfer pathways, meaning the excitation moves up the branches to the two BChls known as the special pair (labeled as P in Figure 3.3 (a)), where charge separation is usually initiated. Strong pigment-pigment interactions, which have been predicted theoretically and observed experimentally, give rise to these energy-transfer processes [141, 142]. Upon charge separation, however, electron transfer occurs only down the A branch to Q_A [143, 144]. From Q_A, the electron transfers to Q_B, after which, when Q_B is fully reduced, it leaves its binding pocket to drive downstream biochemistry [133]. Extensive investigations into the structure, biochemistry, and photophysics of the bRC [145, 146, 147, 148, 149] have examined the differences in protein environment and the resultant functional asymmetry. Despite this effort, the differences in excited-state energies and dynamics remain incompletely described.

Two-dimensional electronic spectroscopy maps the electronic structure and dynamics of condensed phase systems [50, 89, 49]. Two-dimensional spectra are frequency-frequency correlation plots, where the dependence of emission energy on excitation energy is represented for a selected set of time delays between excitation and emission events. These plots

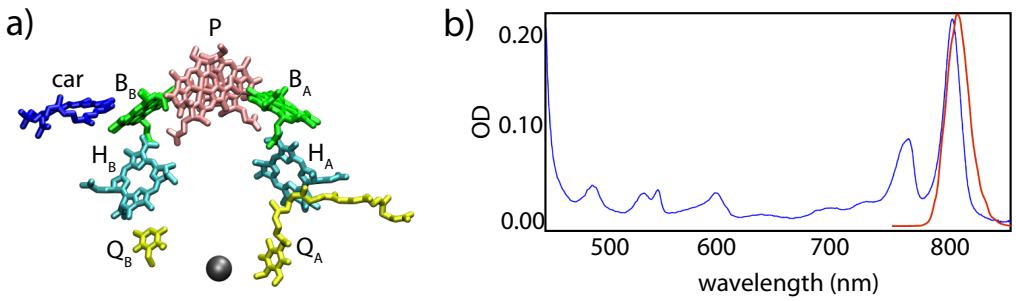

Figure 3.3: Structural model and linear absorption of the bacterial reaction center. (a) Structure of the bacterial reaction center from *Rb. sphaeroides* as determined by X-ray crystallography (PDB code: 2J8C). For clarity, the phytol tails of all bacteriochlorins are truncated. The two branches of pigments both transfer photoenergy to the special pair, P. Upon charge separation, electrons transfer down the A branch. (b) Linear absorption spectrum of the oxidized bacterial reaction center from Ga-strain *Rb. sphaeroides* at 77 K. The excitation laser spectrum is shown as the red line.

display excited-state energies, excited-state couplings, and energy transfer with femtosecond time resolution [150]. From the resultant enhanced spectral resolution across both the excitation and emission axes, this technique can reveal features that are buried in other linear and nonlinear spectroscopies [92]. In particular, the antidiagonal elongation in the nonrephasing component of 2D spectra provides a means to separate closely spaced excited states [151].

Here we describe 2D experiments on the B band of the oxidized bRC (the peak at $\sim$ 800 nm or 12 500 cm^{-1}, in Figure 3.3 (b), arising from the BChl labeled as B_A and B_B in Figure 3.3 (a)). Under high light conditions, a large percentage of the reaction centers are oxidized (closed), and if left unquenched, excited BChl can convert to a triplet state, which can generate deleterious reactive oxygen species. Regenerating the reaction center carries both metabolic (production of new pigments) and opportunity (lost charge separation events during regenerative time) costs. Understanding the dynamics in the oxidized bRC can reveal how it is protected in the absence of the electron transfer pathway. We have investigated the two states proximal to the site of charge separation, the Q_y ($S_0 \rightarrow S_1$) transitions of B_A

and B_B, which correspond to the final steps in the energy transfer chain before the excitation reaches the oxidized special pair. These two states appear as a single peak in linear and nonlinear spectra, which has obscured efforts to investigate their separate dynamics. Spectroscopic studies have, however, indirectly indicated differences in the energies of B_A and B_B. Three-pulse photon echo peak shift (3PEPS) experiments observed two separate bath correlation time scales within the B band of 60 and 90 fs determined under 790 and 810 nm excitation, respectively [129]. Additionally, results from transient absorption experiments with both oxidized and neutral bRCs suggested that, after excitation of the B band, energy transfer along the A branch is slightly faster [152, 128, 153]. Finally, transient absorption spectra suggest an alternate charge separation pathway, with an initial state of $B_A^+H_A^-$, that forms only along the A branch. As this charge-separated state has been observed primarily in the H_x region, this branch-specific effect will fall outside the spectral window of the experimental results discussed in this work [154]. Here we exploit the spectral resolution in excitation and emission provided by 2D spectroscopy as well as the antidiagonal elongation seen in nonrephasing 2D spectra to achieve direct observation of two separate excited-state energies for the first time and relaxation dynamics for the two states within the B band.

Two-dimensional real, nonrephasing spectra of the Q_y region are shown in Figure 3.4. In the linear absorption spectrum shown in Figure 3.3 (b), the two B-band states appear as one peak centered close to 800 nm (12 500 cm^{-1}). In the nonrephasing component of the 2D spectra, two distinct excited states and the dynamics of these two states can be observed. As labeled in the T = 40 fs spectrum, the 2D nonrephasing spectra exhibit two separate positive, diagonal peaks, corresponding to the two states in the B band that are labeled D1 (12 325 cm^{-1}) and D2 (12 450 cm^{-1}). The B-band peak observed in the 2D nonrephasing spectra is slightly red-shifted from the linear absorption peak due to the partial overlap with the negative, excited-state absorption (ESA) feature at $\sim$12 550 cm^{-1}. A second, less intense ESA peak lies at lower energy ($\sim$12 200 cm^{-1}). The ESA peaks increase in intensity relative to the positive diagonal peaks until $\sim$ 50 fs and then show near constant intensities relative to the positive diagonal features through the 150 fs waiting time, which is the time window discussed here. On the basis of previous assignments, D1 most likely corresponds to the B_B transition, and D2 most likely corresponds to the B_A transition [129, 154]. Using polarized linear absorption on neutral bRC crystals, the excited-state energies were determined to be 800 nm (12 500 cm^{-1}) for B_A and 810 nm (12 345 cm^{-1}) for B_B, which compare favorably to our values of 12 450 and 12 325 cm^{-1} [154]. The small shifts may be from the ESA peaks that contribute to nonlinear spectra or from the change in local environment due to formation of P^+. Energy transfers out of the B band (to states localized on P^+) by the T = 300 fs spectrum (not shown). This is also in accordance with previous results, in this case transient absorption measurements [152]. As energy transfers out of D1 and D2, the positive signal from stimulated emission decreases and so cancels out less and less of the negative ESA, resulting in an increase in relative intensity of both negative peaks. However, a second notable feature from the separation of the two peaks is that, as seen in the T = 120 fs spectrum in Figure 3.4, energy transfers out of the D1 state at a slightly faster rate than out of D2.

In the early time spectra (<100 fs), population moving between these two states can be observed by the presence of cross-peaks connecting these two transitions. (The below-

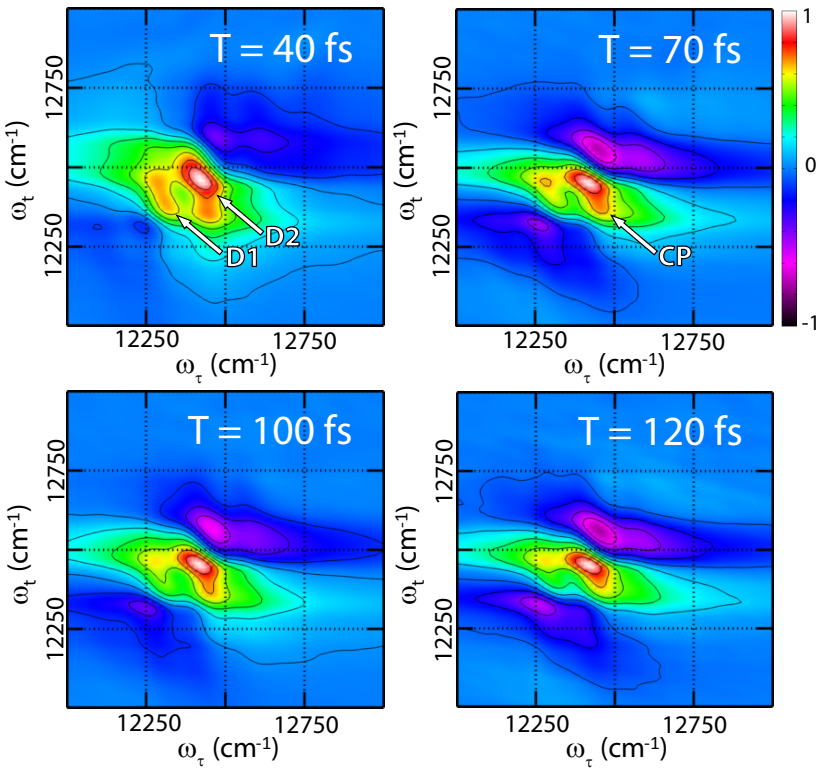

Figure 3.4: Real, nonrephasing 2D spectra of the B band at selected waiting times at 77 K taken under the all-parallel polarization. Each spectrum is normalized to its own maximum. These spectra exhibit two separated states along the diagonal, labeled D1 and D2 in the T = 40 fs spectrum. Energy transfer between these two states appears in the increase in intensity of the cross-peak labeled CP in the T = 70 fs spectrum. The T = 100 and 120 fs begin to show energy transferring out of band, first from D1.

diagonal peak is labeled as CP in the T = 70 fs spectrum.) There are cross-peaks above and below the diagonal, indicating population transfer in both directions between the two states in the B band. The maximum intensity of CP occurs at $T = \sim$70 fs, as population then transfers out of band with a similar time scale as D1. Two distinct transitions as well as interactions between them were not previously observed with other techniques.

The polarization dependence of CP provides further evidence of energy transfer and a greater ability to quantify energy transfer [155]. We investigate the cross-peak below the diagonal. Within a 2D spectrum, each peak is scaled by an orientational prefactor based on the angles between the transition dipole moments in the molecular frame and the angles between the laser pulse polarizations in the lab frame. This has been extensively described elsewhere [92, 155, 156, 157]. Except in the case of energy transfer between a donor and acceptor

with parallel transition dipole moments, cross-peaks will scale differently with changes to the polarization of the incident beams than will diagonal peaks corresponding to absorption and emission from the same state. Spectra were recorded under the all-parallel (0,0,0,0) and cross-peak-specific (π/3,-π/3,0,0) polarization sequences, which are polarization sequences that maximize intensities for energy-transfer steps between parallel transitions and between perpendicular transitions, respectively. We refer to the latter as the cross-peak-specific sequence. Absolute value, nonrephasing spectra taken under the cross-peak-specific polarization sequence are shown in the Supporting Information. The change in scaling of energy-transfer peaks relative to diagonal peaks under these two polarization sequences has been described in detail in previous work [92, 158].

Horizontal slices at the emission energy of D1 (12 325 cm^{-1}) are shown in Figure 3.5 for both the parallel and cross-peak-specific polarization sequences. CP contains intensity from both energy transfer and the dispersive tails of the diagonal peaks. In the all-parallel slices, there are similar relative amplitudes of CP and D1, and compression and spectral fluctuations produce the small intensity fluctuations as a function of waiting time. Under the cross-peak-specific polarization, however, the suppression of the diagonal peaks also suppresses the dispersive tails. This allows a relative enhancement of energy-transfer peaks, and the energy-transfer step appears much more clearly. Specifically, there is a clear increase in relative intensity as amplitude moves from D1 to D2, or as the cross-peak grows in, as shown in Figure 3.5 (b). The CP increases in relative intensity between 40 and 150 fs. This strongly suggests that energy transfer occurs in $\sim$100 fs. If there was no population transfer between these two states, then the difference in polarization sequence would not change the relative intensities of the two peaks. These spectra provide, for the first time, direct evidence of interaction between the two states within the B band.

Whereas the spectra show that amplitude initially on one state in the B band ends up localized on the other, the underlying mechanism remains unknown. There are several possibilities, which we will now discuss, along with an evaluation of their probability. The simplest possibility is that energy could transfer directly from B_A to B_B. On the basis of the calculated B_A to B_B coupling (J = 45 cm^{-1}) [159], the energy gap between the two excited states (125 cm^{-1}), and the reorganization energy due to electron-phonon coupling (80 cm^{-1}), an energy-transfer time scale of a few hundred femtoseconds would be expected. This determination of a rough time scale was made by comparison to the extensive theoretical modeling of each energy-transfer step in the Fenna-Matthews-Olson (FMO) complex [160]. Therefore, the sub-100 fs time scale observed experimentally most probably does not arise from standard energy transfer between the two states.

The second possibility is some component of the energy transfers before localization occurs. The energy eigenstates, or excitons, are delocalized excited states constructed from linear combinations of the excited states of the individual BChl. Calculations on the oxidized bRC have produced the two excitons localized primarily on the B band. The major site basis contributions to these two states are 0.52 and 0.15 from B_A, 0.21 and 0.74 from B_B, and 0.16 and 0.06 from P_5^+ (one of the states localized on the oxidized special pair) [159]. Therefore, these two eigenstates, which are the initially excited states, both have contributions from B_A, B_B, and P^+. Previous experimental and theoretical work has shown that energy transfer

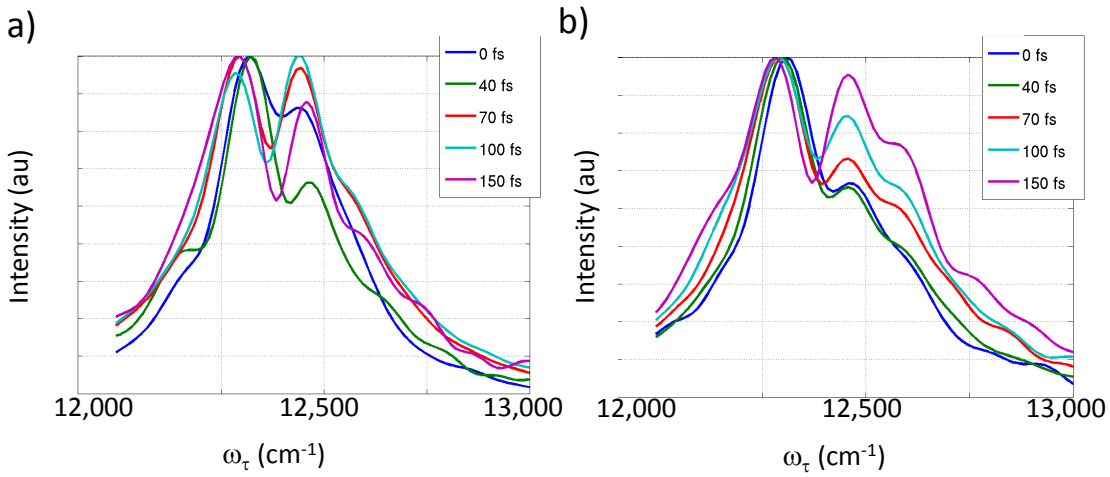

Figure 3.5: Normalized, horizontal slices from the absolute value, nonrephasing 2D spectra at ω_t = 12 325 cm^{-1} for (a) all-parallel and (b) cross-peak-specific polarization sequences. The difference in scaling with polarization, as appears in the clear grow-in of the cross-peak (ω_τ = 12 450 cm^{-1}) under the cross-peak-specific sequence, indicates the existence of an energy-transfer pathway. The suppression of other features also allows the appearance at 70 fs and relative increase in the cross-peak to be more clearly observed.

can occur rapidly ($\sim$ 100 fs) in the event of spatial overlap between excitons. Energy-transfer rates are determined by a balance of electronic coupling and electron-phonon coupling, which is coupling to the protein bath [161, 162]. When the electron-phonon coupling is greater than the electronic coupling, the excitation localizes and energy transfer occurs via hopping from one state to another. There is a time scale associated with localization as phonon reorganization dynamics take place after excitation or re-equilibration of the nuclei in response to the electronic excitation. Before localization, some component of the population can exploit the spatial overlap of these two excitons and transfer rapidly between them.

A third possibility is that the population transfers via two individual energy-transfer steps. Theoretical results have shown several weakly optically allowed states localized on P^+, the oxidized special pair, that have energies close to the B band [159]. Therefore, energy can transfer from B_A first to these states on P^+, and then to B_B. In the case of two sequential incoherent energy transfer steps, the first step (B_A to P^+) is 200 fs. The second step is longer because although the P^+ to B_B rate cannot be directly measured, the B_B to P^+ rate, which

should be faster because it is a downhill transfer, is 400 fs [153]. These two time scales make it unlikely that a component would be visible via this pathway in $<$100 fs.

The fourth possibility is that there is a coherent sequence of B_A de-excitation, P^+ excitation and de-excitation, and finally B_B excitation. With this sequence, the rate can increase [163, 164] according to a superexchange or a "through bond" mechanism, where a linker can mediate indirect coupling between two states. Energy transfer from B_A to B_B can be mediated by these P^+ states serving as a bridge [165]. Experimental and theoretical work has shown that superexchange can produce drastic increases in energy and electron transfer rates [163, 164, 165].

At this point, there is no direct experimental tool to determine whether superexchange or direct energy transfer gives rise to the observed peak. Regardless of mechanism, the experimental results suggest that there is more interaction between the two branches than is often included in the general description of two isolated energy transfer pathways.

The transfer of amplitude from B_A to B_B observed here could offer insight into how the reaction center prevents photodamage by using these states as an alternative pathway for excitation energy. Additionally, this transfer pathway does not interfere with the major dissipation mechanism, whereby the oxidized special pair quenches excitation energy. Photosynthetic systems, however, have multiple levels of safeguards to protect themselves against damage. Whereas there are mechanisms for dissipating harmful photoproducts, such as carotenoids dissipating $BChl^T$ states [166, 26], the energy-transfer pathways are designed to minimize the initial formation of these photoproducts. One mechanism by which this is accomplished is by ensuring that the excitation does not remain trapped in local minima. Experimental and theoretical results show that in purple bacteria around 20% of photoenergy that reaches the bRC is detrapped from the bRC [167, 168, 169, 170]. Calculations suggest that only 13% of the detrapped photoenergy is retrapped by the same bRC. Instead, the vast majority migrates to other bRCs [170]. The pathway observed here may aid in preventing the accumulation of photoproducts because the excitation does not remain trapped on a single BChl but can move around the bRC. Either of the BChl could be better positioned for the excitation to transfer back to LH1, depending on PPC to PPC variation in site basis contributions, energies, and transition dipole moments of the low-energy excited states due to protein fluctuations. From LH1, the excitation can then transfer to neighboring antenna and bRCs.

By exploiting the antidiagonal elongation of 2D nonrephasing spectra, the energies of the two distinct, previously inseparable states within the B band were determined, and transfer of amplitude most simply described as energy transfer between these two states was observed for the first time. Furthermore, the energy-transfer process was characterized by comparing results taken under the all-parallel and cross-peak-specific polarization sequences. The observation of a second energy-transfer pathway may inform on how excitations can easily migrate around the photosynthetic apparatus, thus preventing the formation of deleterious photoproducts. The observation of two separated excited states directly displays the difference in electronic structure of the two branches and thus provides a much more direct reporter of difference in the effective molecular structure of the two branches. The observed excited-state energies and dynamics can benchmark microscopic modeling of how small differences in molecular structure, that is, differences between the two branches, give rise to

tuned pigment-pigment or pigment-protein couplings. Overall, these results illustrate the wealth of information provided by the addition of spectral resolution along both excitation and emission axes provided by 2D spectroscopy and the potential to access previously unknown dynamics through the extension of the technique into polarized pulse sequences.

3.2.1 Experimental Methods

Previously described methods were followed in preparing and isolating the reaction centers of *Rhodobacter sphaeroides*, strain Ga [131]. The samples were suspended in 20 mM Tris HCl and 0.1% LDAO buffer (pH 8.0), and 100 mM $K_3Fe(CN)6$ was added to the buffer to oxidize the primary electron donor, P. The sample was diluted 30:70 (v/v) with glycerol and cooled to 77 K. The OD at 800 nm was 0.2 to 0.3 per 200 μm.

A home-built Ti:sapphire regenerative amplifier, seeded by a home-built Ti:sapphire oscillator, produces a 3.4 kHz pulse train of 45 fs pulses centered at 805 nm with 27 nm of bandwidth, as measured by SHG-FROG [45]. The energy on the sample from each of beams 1, 2, and 3 was 4 nJ per pulse, and beam 4 was attenuated by four orders of magnitude. The beams were focused to a 70 μm beam waist. For the polarization experiments, true zero-order waveplates (CVI) were inserted into beams 1 and 2 and set with a precision of ± 2. All measurements were performed at 77 K.

The details of the experimental apparatus, data acquisition, and analysis have been described in detail elsewhere[45]. The laser beam is split into four beams using a beamsplitter and a diffractive optic. The use of the diffractive optic allows for phase stability between pulse pairs. The four ultrafast beams are incident on the sample in a box geometry. The interaction of three of the beams with the sample generates the signal, emitted in the phase-matched direction, $k_s = -k_1 + k_2 + k_3$, collinear with the fourth beam, a local oscillator pulse. The local oscillator is attenuated by four orders of magnitude to ensure that it does not interact strongly with the sample. Using spectral interferometry, the signal is heterodyne-detected in the frequency domain [171].

The measured electric field is a function of the three time delays between the pulses [150, 172]. The time delay between the first two pulses is known as the coherence time, τ, and is controlled to interferometric precision with movable glass wedges, which were scanned from -390 to 390 fs in 1.3 fs steps. Negative coherence times generate the nonrephasing signal, and positive coherence times generate the rephasing signal. Between the second and third pulses, the system evolves dynamically during a so-called "waiting time", *T*. The third time delay, between pulse 3 and the signal emission, is the rephasing time, *t*. The frequency-frequency 2D spectrum at fixed *T* is produced by spectrally resolving the signal along ω_t and then Fourier-transforming along the scanned coherence time axis, τ. In this frequency domain representation, the spectrum directly correlates excitation and emission energies. The ensemble of PPCs evolves in a coherence during both the coherence time and the rephasing time. If the system progresses in conjugate frequencies during these two time periods, then this allows for the reversal of dephasing and the generation of a photon echo signal. To produce a nonrephasing signal, the ensemble of PPCs evolves with a phase factor of the same sign during the coherence time and the rephasing time, thus generating a free induction

decay signal. The rephasing and nonrephasing signals are separated experimentally by the time ordering of pulses one and two. The signal generated over the entire scan, or the sum of the photon echo and free induction decay contributions, produces a relaxation spectrum for $T>0$. Phasing was performed using the projection-slice theorem by separately measuring the spectrally resolved pump-probe signal for each waiting time [150].

3.2.2 Supplemental Information

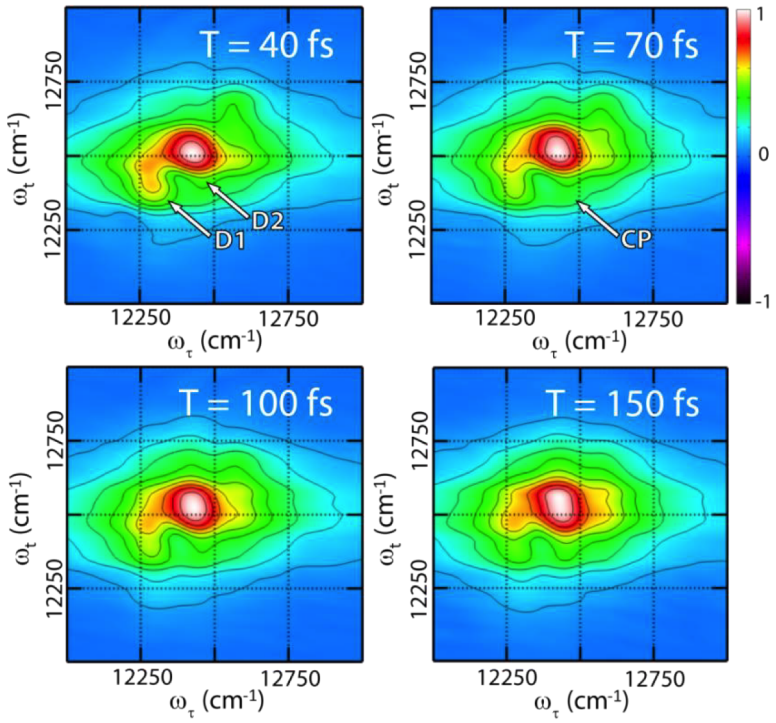

Figure 3.6: Absolute value, nonrephasing spectra of the B band of the bacterial reaction center at selected waiting times at 77 K taken under the cross-peak specific polarization. Each spectrum is normalized to its own maximum. These spectra exhibit two separated states along the diagonal, labeled as D1 and D2 in the T = 40 fs spectrum. Energy transfer between these two states appears in the increase in intensity of the cross-peak (CP in the T = 70 fs spectrum).

3.3 2 color 2D Electronic Spectroscopy

As we have discussed previously in this thesis, two dimensional electronic spectroscopy is a powerful experimental technique that allows us to elucidate energy transfer dynamics and coupling between electronic transitions with both spectral and temporal resolution. An extension of 2DES to a non degenerate experiment, in which the pulses have different spectra, allows us to investigate electronic transitions that are spectrally well-separated.

There have been previous implementations of non-denegerate 2DES experiments. In particular, the group of Jennifer Ogilvie [173] has developed a system based on an acousto-optic pulse shaper that generates phase-locked pulses, where the two colors were obtained from two independent non-collinear optical parametric amplifiers (NOPAs). Additionally, implementations of 2DES with a continuum probe (analogous to a spectrally resolved transient absorption experiment) have been shown [174, 175], as well as implementations in which all four pulses are generated from a supercontinuum [176, 177].

Here we present the first fully non-collinear implementation of 2DES where pulses 1 and 2 have a different color from pulses 3 and 4. Pulses 1 and 2 are obtained in this experiment as the output of a non collinear optical parametric amplifier, so are tunable over the visible range. Pulses 3 and 4 are the direct output of the regenerative amplifier, therefore they are centered around 800 nm. The non-collinear geometry has advantages over other implementations. It allows for easy separability of the rephasing and nonrephasing components of the 2D spectra (see Section 1.4.1). Also, it allows for independent control of the polarization of the four pulses, which has been exploited positively in degenerate 2DES experiments to separate out specific energy transfer pathways (see Section 3.2 and [158, 151, 92]).

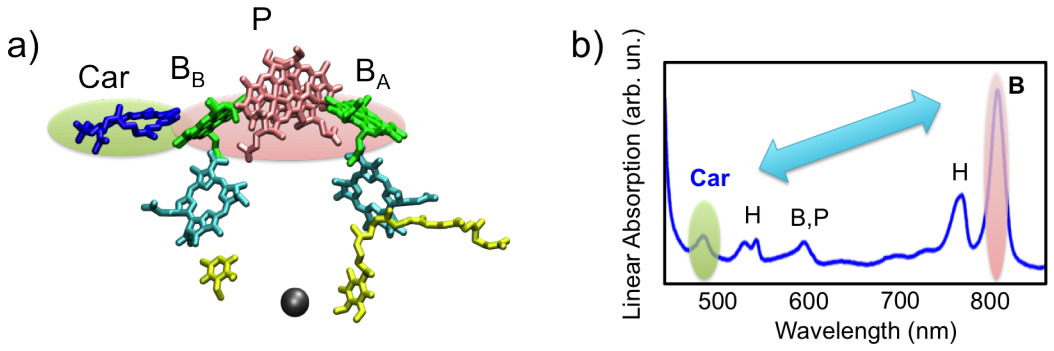

Figure 3.7: (a) Structure of the bRC highlighting the excitation of the Car (green oval) and the investigation of the accessory BChls (red oval). (b) Linear Absorption spectrum of the oxidized bRC, which shows the excitation of the Car (green) and the probing of the accessory BChl Q_y transition (red).

In this Section, I will present the results of 2-color 2DES experiments on the bRC, in which excitation of the Car band is followed by probing of the B band (see Fig. 3.7). The goal of these experiments is to investigate the energy transfer pathways between spectrally separated transitions. Upon excitation of the Car, we are interested in elucidating the energy transfer pathways available to transfer excitation energy efficiently to the BChl and how fast this energy transfer occurs. To investigate wavelength regions with an energy separation larger than the laser spectrum, we need to have the flexibility of ”pumping” and ’”probing” the two transitions independently, such as in a non-degenerate transient absorption experiment. We present here the extension to the experimental setup used for the degenerate 2DES experiment presented in Section 1.4.1.

Since the Car in the RC is in a *cis* configuration, its electronic structure is altered with respect to the C_{2h} point group symmetry discussed in Section 1.1. However, singlet energy

transfer between the Car and the BChl has been observed in the RC from purple bacteria to occur with high efficiency ($\sim$ 80 %) [178, 179], therefore the *cis* geometry must not have a strong effect on the energy transfer capabilities of the Car in the RC.

As we have mentioned, the Car plays an important role in closed reaction centers by quenching BChl triplet states that can form. We will investigate here the dynamics in a closed reaction center (in which the primary donor is oxidized). If the special pair is completely absent, the lifetime of the BChl is longer than a nanosecond [149], but if the oxidized donor P^+ is present, the excited BChl is quenched in a few hundred femtoseconds [180, 148, 126, 153]. Recent measurements on oxidized reaction centers [153], however, have shown how species emitting at 800 nm, upon excitation at 495 nm, take picoseconds to decay. These results were interpreted assuming that B_B generates a picosecond lifetime intermediate state, suggesting different decay processes or newly populated B_B excited states, upon Car excitation. We will exploit the spectral resolution across excitation and emission here to map out the energy transfer dynamics in an oxidized bRC.

3.3.1 Experimental Apparatus

Figure 3.9 shows a schematic of the experimental apparatus. The setup is based on the experimental apparatus described in Section 1.4.1. As shown in Fig. 3.9, a home-built Ti-Sapphire regenerative amplifier generates 41 fs pulses centered at 805 nm, with $\sim$ 30 nm of bandwidth, as characterized by SHG FROG. The radiation out of the amplifier is split into two by a combination waveplate/thin film polarizer. A portion of the radiation is sent through a non collinear optical parametric amplifier (NOPA) to generate broadband pulses (50 nm - 100 nm FWHM) centered at 490 - 720 nm. The pulses can be compressed with a combination of prisms and a diffraction-based spatial light modulator (SLM) pulse shaper [181] to a duration close to their transform-limit [95]. Characterization of the pulses is obtained via transient grating frequency-resolved optical gating (TG-FROG) [99] on a 2-mm quartz plate at sample position [95]. In this experiment, the NOPA pulses are centered at 495 nm, with 40 nm bandwidth FWHM, and compressed to 24 fs with the prism compressor. Due to the high losses of the diffraction-based SLM, we could not make use of this system to further compress the pulses. The NOPA output corresponds to pulses 1 & 2 in the 2DES pulse sequence (see Fig. 3.10).

The remaining portion of the radiation is taken directly as the output of the regenerative amplifier and constitutes beams 3 $\&$ 4. The pulses are sent through a delay stage, which controls the waiting time T with respect to pulses 1 $\&$ 2 (see Fig. 3.9). Each of the two beam pairs is further split into two by a diffractive optic (DO) optimized for first-order diffraction, allowing for phase stability between the two pulse pairs. The coherence time τ is again controlled with movable glass wedges, as in the degenerate experiment (see Section 1.4.1). Beams 1 $\&$ 2 are then in the visible, centered around 500 nm, while beams 3 $\&$ 4 are centered at 800 nm. Beam 4 is the local oscillator and is attenuated by four orders of magnitude, and delayed with respect to beam 3 by an additional pair of glass wedges inserted into the beam 3 path. The beams are focused to the sample position to a spot size of $\sim$ 120 μm for beams 1 & 2, and $\sim$ 70 μm for beams 3 & 4. Fig. 3.8 shows the spectrum of pulses 1 $\&$ 2 and 3 $\&$ 4,

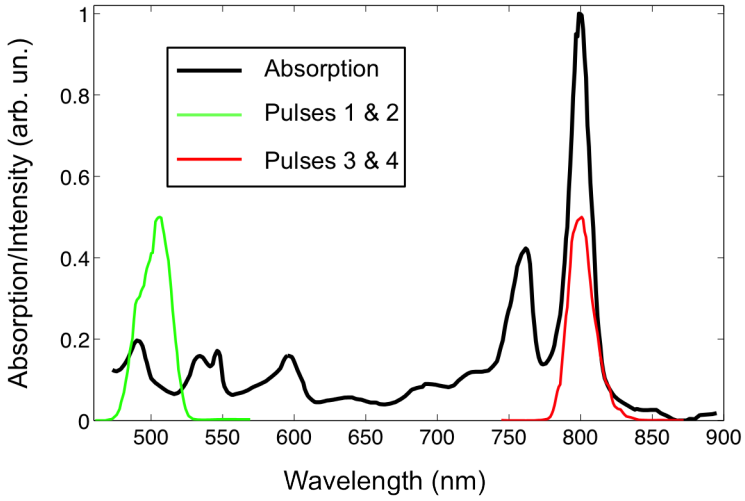

Figure 3.8: Spectrum of pulses 1 and 2 from the NOPA (green thin line) and of pulses 3 and 4 from the regen (red thin line) superimposed to the linear absorption spectrum at 77 K of the sample (black thick line). Pulses 1 and 2 are resonant with the Car peak, pulses 3 and 4 with the B band, Q_y transition.

superimposed to the linear absorption spectrum of the sample.

The signal is emitted in the phase matched direction, and dispersed on a spectrometer onto the pixels of a CCD camera. The retrieval of the 2D spectrum is as described in Section 1.4.1. The coherence time is scanned from -390 to 390 fs in 1.3 fs steps, keeping the waiting time T fixed. The waiting time T is fixed and we collected spectra at T = -1000 fs, -500 fs, -200 fs, 0 fs, 40 fs, 70 fs, 150 fs, 200 fs, 300 fs, 400 fs, 600 fs, 750 fs, 800 fs, 900 fs, 1000 fs, 1200 fs, 1500 fs, 2000 fs.

3.3.2 Results and Discussion

Fig. 3.11 shows 2 color 2D relaxation spectra (absolute value) for selected values of the waiting time T. The excitation axis corresponds to the main Car transition, while the detection spectral region is centered on the Q_y transition of the B band. The T = 40 fs spectrum shows four main peaks, all emitting at 800 nm. The excitation wavelengths are 490 nm (peak A in the figure), 493 nm (peak B), 497.5 nm (peak C) and 510 nm (peak D). Peaks A, C and D are present even before time zero and at time zero (see the spectrum at T = -200 fs in Fig. 3.11), and their physical origin remains to be elucidated. At early times ($T < 600$ fs), most of the intensity is in peak D. Peak B appears for the first time in the T = 40 fs spectrum and becomes a dominant peak at longer delay times ($T > 600$ fs).

At T = 750 fs, the most intense peak becomes peak A, while peak D completely disappears and new peaks (E and F in the Figure) appear. These peaks have excitation at 501 and 510 nm respectively, and emission at 820 nm. Emission at these wavelengths most likely corresponds to emission from states localized on P^+ (we are looking at energy transfer in a an oxidized reaction center, where no charge separation can occur). Peak E appears in the T = 600 fs

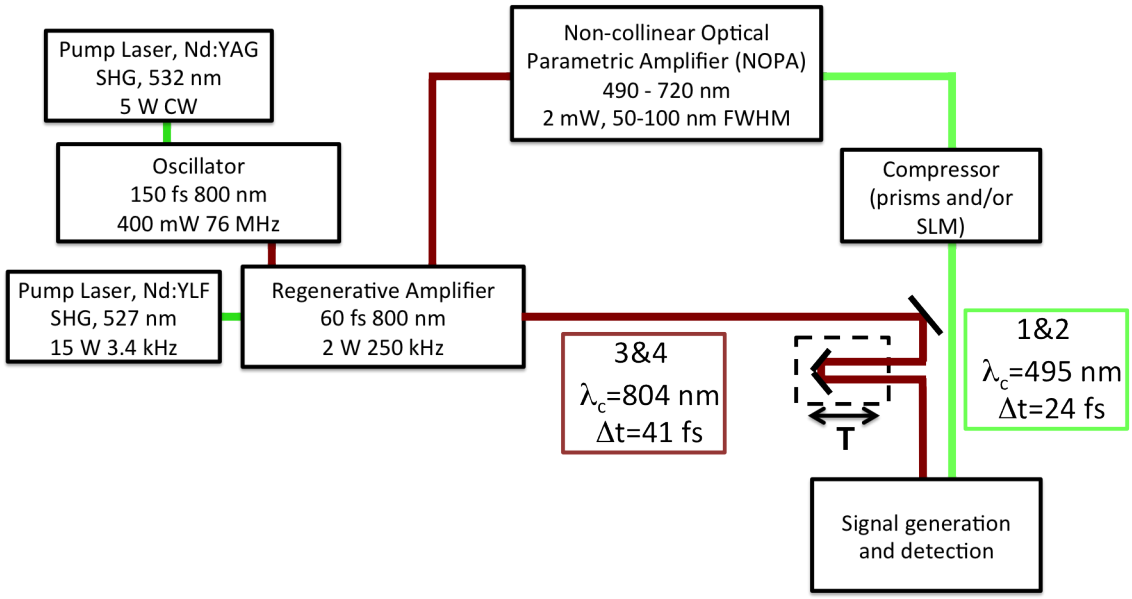

Figure 3.9: Schematic of the experimental apparatus used for the 2-color 2D Electronic Spectroscopy experiments explained in this Chapter. The main components are: the home-built oscillator/regenerative amplifier combination; the NOPA (Non-collinear Optical Parametric Amplifier), which generates broadband pulses in the visible. The compressor has two stages: a prisms compression line is followed by a diffraction-based spatial light modulator (SLM) pulse shaper. Upon retrieval of the phase of the pulse with frequency detected optical gating (FROG), an arbitrary phase can be applied with the pulse shaper to the pulse, thus ideally reducing the dispersion on the pulse to zero. Beams 3 and 4, coming directly from the regenerative amplifier, are sent through a delay stage controlling the waiting time *T*. Then the two pulse pairs are sent to the stage of Signal Generation and Detection, described in detail in Fig. 3.10.

spectrum (not shown) and is completely gone by the T = 1500 fs spectrum. Peak F, on the other hand, appears at T = 750 fs and is gone by T = 1200 fs. Peaks A, B, and D are present until T = 2 ps.

In order to interpret the physical origin of the peaks listed, it's important to remember that peaks in a 2-color spectrum are off-diagonal peaks that correspond to either transitions between states different from the excitation transition (in this case, transitions coupled to the S_0 - S_2 transition for the Car and emitting in the same wavelength region as the B band) or to energy transfer peaks (Car to BChl). The laser pulse excites the 0-0 transition of neurosporene (see Fig. 3.11). Higher-lying vibrational levels of the Car are not excited due to the bandwidth and spectral position of our excitation pulse. Also, since the measurements are performed at 77 K, we can assume that all of the population is initially in the lowest vibrational level of the ground state. Upon excitation of the $S_0 \rightarrow S_2$ transition of the Car, we expect to see energy transfer peaks to appear in the 2 color spectrum following two separate pathways. One of them is from the Car S_2 via the BChl Q_x, which subsequently relaxes to the BChl Q_y on a timescale of $\sim$ 200 fs [insert reference]. A second pathway follows the relaxation of the Car to its S_1 state, followed by energy transfer from the Car S_1 to the BChl Q_y. The BChl Q_y state then transfers energy to states localized on P^+ on a $\sim$ 300-400 fs timescale (see our results in

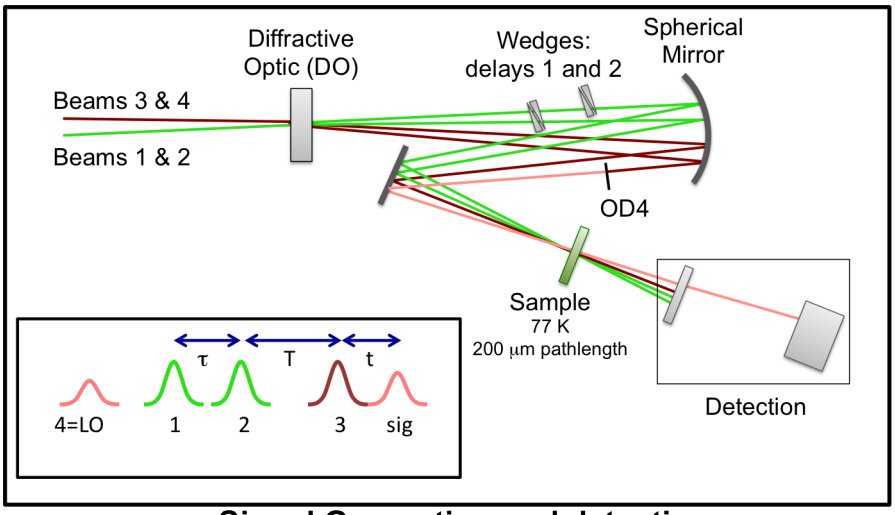

Figure 3.10: Details of the Signal Generation and Detection portion of the 2 color 2DES apparatus shown in Fig. 3.9. The two pulse pairs are sent through a diffractive optic (DO), which is a grating optimized for -1 order dispersion. Beams 1 and 2 are sent through movable glass wedges, which control the coherence time τ. Beam 4 is attenuated (local oscillator), while beam 3 is sent through a pair of glass wedges to control the delay with respect to the local oscillator. The four beams are focused at the sample position and the signal, emitted collinearly with the local oscillator, is collected on a spectrometer/CCD combination. The inset shows the pulse sequence used in the experiment. For details on the detection system and the reconstruction of the 2D spectrum, see Section 1.4.1.

the previous Section and [153]).

The presence of peaks before time zero (see peaks labeled A, C, and D in the T = -200 fs spectrum in Fig. 3.12) and at time zero is unclear. These peaks might be due to 1) a long-lived state that survives between different laser pulses (thus a state for which its lifetime is longer than 294 μs); 2) the formation of an excitonic state between two transitions, giving rise to new energy levels that do not appear in the linear absorption (for short-lived excitons) but that are populated instantaneously. The formation of these transitory excitonic states could be assigned to a local change in the energy of the contributing transitions or to a change in their local environment due to excitation. This second possibility would explain the presence of the peaks at time zero, but does not explain as well their appearance in the T = -1 ps spectrum (data not shown).

It is unclear why the peaks appear as separate peaks, rather than a single peak, especially if their origin is due to initial population of a Car excited state (see below). In particular, the origin of the state absorbing at 510 nm is confusing, since the absorption of the bRC at this wavelength is almost zero, even though most of our excitation energy is at this wavelength (see spectrum of the excitation pulse in Figs. 3.11, 3.8). This peak must be due then to instantaneous population of an otherwise dark state, which could be either S_1 or the dark state X identified by Ostromouv *et al.* [121]. Alternatively, this peak might be due to population of a carotenoid triplet state, which has been observed at these wavelengths previously [131]. Population of this state could occur either directly upon excitation of the Car, or from

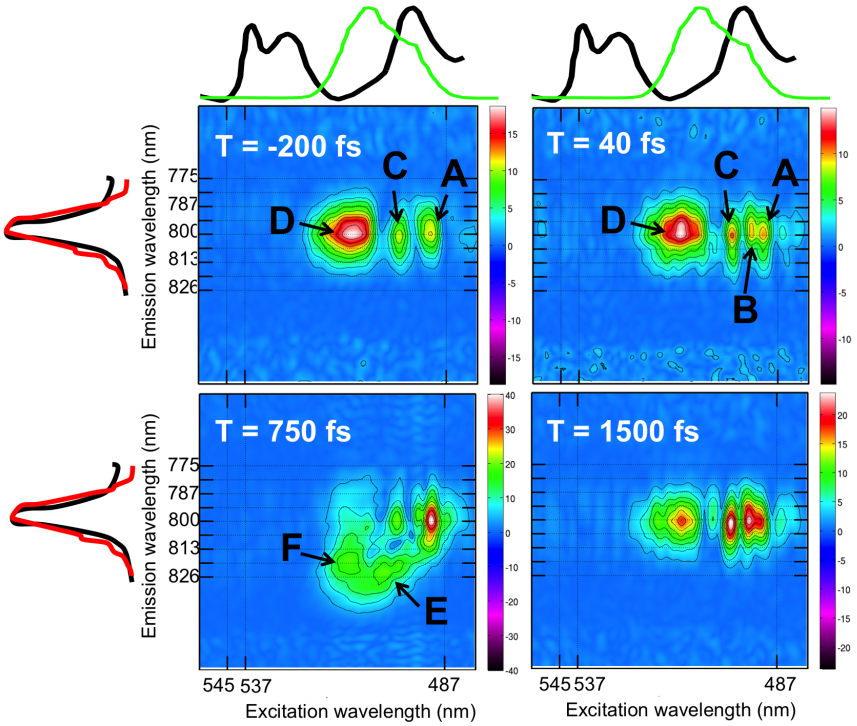

Figure 3.11: 2D absolute valued relaxation spectra for selected values of the waiting time (T = -200 fs, 40 fs, 750 fs, 1500 fs). On top of the spectra, the linear absorption spectrum of the bRC in the excitation spectral region (Car band, H band) is shown (black line), together with the spectrum of the excitation pulse (pulses 1 and 2, green line). On the left side, the linear absorption spectrum in the emission spectral region (B band) is shown (black line), together with the spectrum of pulse 3 (red line). The main peaks in the 2D spectra are labeled A, B, C, D, E and F and their physical origin is discussed in the text. The (excitation, emission) wavelengths for the peaks are, respectively: A (490.4 nm, 800 nm), B (493 nm, 800 nm), C (497 nm, 800 nm), D (510 nm, 800 nm), E (501 nm, 820 nm), F (510 nm, 820 nm).

charge-recombination of a partially non-oxidized population of the bRC, via BChl triplet state formation (see point (3) below for further explanation). However, the half-time decay of this triplet state has been shown to be around 5 μs [131], therefore much shorter than the pulse-to-pulse time interval.

In order to discern the physical origin of the features observed in the 2D spectra, we have drawn Feynman diagrams that elucidate the possible observed pathways (see Fig. 3.12). These are the possible contributing pathways that could contribute to the features observed in the 2DES spectra, however we believe that pathways (3) and (4) are the main pathways contributing.

- (1) *$T < 0$, pulse sequence: 3, 1, 2. Peaks A, C and D.* For negative values of the waiting time, pulse 3 arrives before pulses 1 and 2. Following the Feynman diagram, we observe excitation to the Q_y state of the BChl upon arrival of pulse 3, followed by excitation to a Car excited state generically referred to as Car* in the Figure. This state could be either S_2, S_1 (higher vibrational state that borrows oscillator strength from S_2)

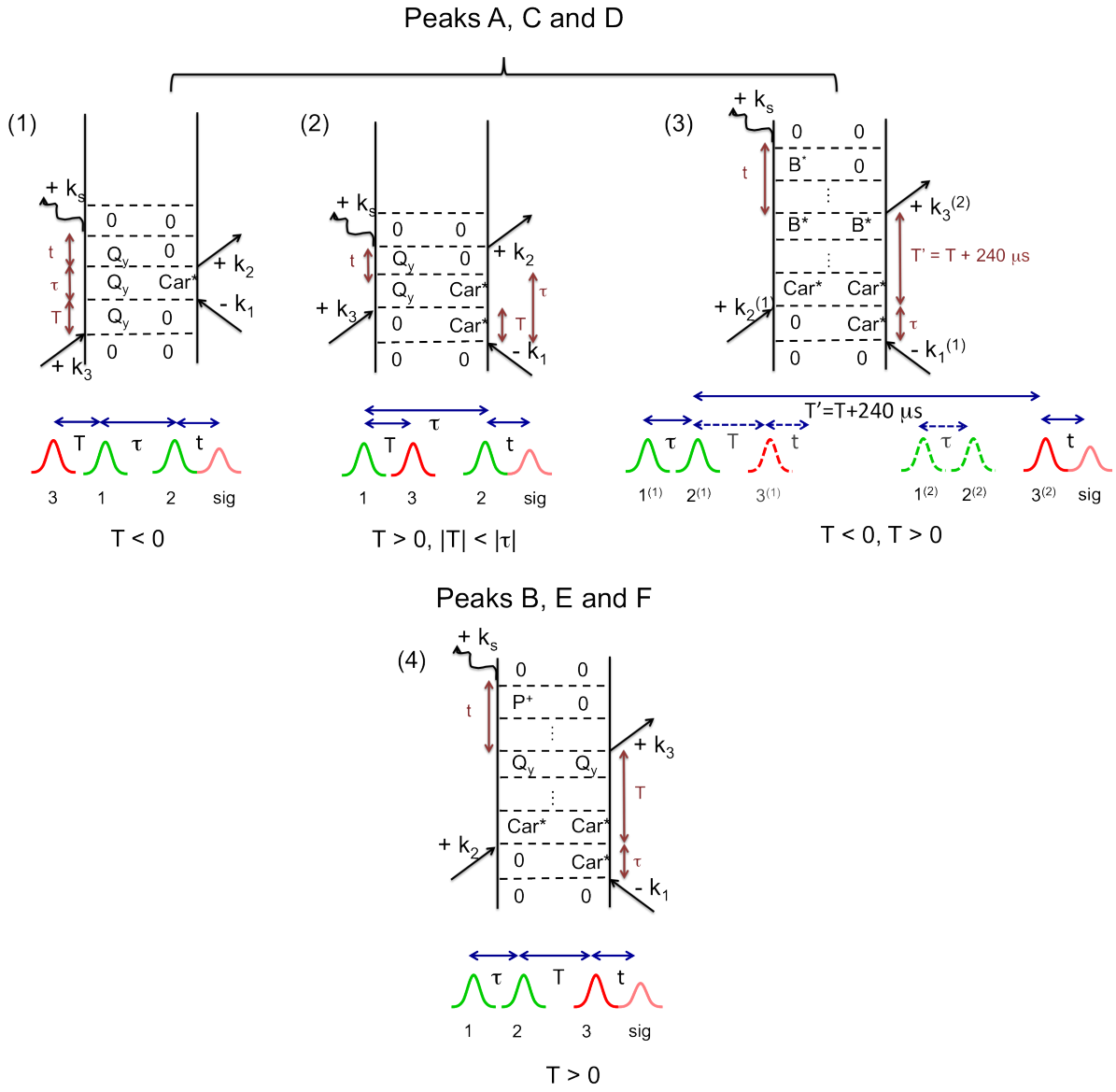

Figure 3.12: Feynman diagrams for three possible pathways given rise to the peaks observed in the 2 color 2DES spectra shown in Fig. 3.11. (1) Pathways for $T < 0$, pulse sequence 3, 1, 2. (2) Pathways for $T > 0$, $|T| < |\tau|$, pulse sequence 1, 3, 2. (3) Pathways for $T > 0$, pulse sequence 1, 2 (from laser pulse 1, labeled as $1^{(1)}$, $2^{(1)}$), 3 (from next laser pulse, labeled as $3^{(2)}$). (4) Pathways for $T > 0$, pulse sequence 1, 2, 3. Car* indicates an excited state of the Car excited by the laser pulse 1 or 2: Car* can be either S_2, a hiher-lying vibrational state of S_1, or X. See text for a description of the pathways.

or the X state. Upon arrival of pulse 2, the Car* decays to the ground state, and after a time t, we observe emission from the Q_y state. This pathway explains the 2D spectra before time zero, where only peaks A, C and D are present. The presence of multiple cross-peaks suggests that all the Car excited states indicated above can be populated and each of these pathways contributes to the 2D spectrum. Additionally, we cannot

exclude some relaxation of the Car* state before the arrival of pulse 2 (such that, for example, pulse 1 could excite S_2, which relaxes onto S_1 on a $\sim$ 300 fs timescale, and pulse 2 stimulates emission from S_1).

- (2) *$T > 0$, pulse sequence 1, 3, 2. Peaks A, C and D.*. For positive values of the waiting time T, but smaller than the coherence time τ, a possible pathway is the following. Pulse 1 excites the Car* state (defined above), and upon arrival of pulse 3, excitation to a coherent Car*-Q_y state is observed. This state evolves until the arrival of pulse 2, which stimulates the decay of the Car excited state, and eventually we observe emission from Q_y. Again, evolution of the Car* state cannot be excluded. This explains the 2D spectra at and immediately after T = 0. This pathway should give features in the 2D spectra identical to those observed for case (1), which would explain why we do not observe much evolution in peaks A, C and D before and after time zero. Additionally, right after time 0, a new cross-peak (peak D) is populated. The origin of this peak can be explained with scheme (4) below.

- (3) *$T > 0$, pulse sequence 1, 2 (laser pulse 1), 3 (next laser pulse). Peaks A, C and D.* Given the absence of time evolution in peaks A, C, and D, we believe that the main pathway contributing to their presence is actually a pulse-to-pulse effect. Pulses 1 and 2 generated from laser pulse '1' induce population of a Car excited state (as defined above). Subsequently, evolution occurs before the arrival of a second laser pulse. During this time (240 μs), evolution to a state indicated as B* occurs. The nature of this state is still under investigation. It could be due to a charged-separated state arising from a non-completely oxidized subpopulation of the sample, or to a recombined state that leads to formation of a BChl and Car triplet state (BChl triplet states, however, have been measured to decay on a $\sim$ 6 μs timescale [182]). Similar charge-separated states have been previously observed emitting around 800 nm [183]. Upon arrival of pulse 3 from the subsequent laser pulse, emission occurs from this B* state. This pathway contributes to all spectra, for $T < 0$ or $T > 0$, but with $T' = T + 240$ μs, where 240 μs is the interval between two subsequent laser pulses in our experiment. This explains why peaks A, C, and D are observed in all spectra, before and after time zero, and not much evolution is observed.

- (4) *$T > 0$, pulse sequence 1, 2, 3. Peaks B, E and F*. Upon arrival of pulses 1 and 2, a Car excited state is populated. The Car* state evolves during time *T*, and energy transfers to Q_x (from S_2; subsequently, Q_x relaxes to Q_y over $\sim$ 200 fs) and Q_y (from S_1). After arrival of pulse 3, we observe, after a time *t*, emission from the Q_y state. This pathway explains population of peak B, as energy transfer from the Car* to the BChl B band. However, it is unclear why peaks B is present even in the T = 2 ps spectrum, since we would expect energy transfer between the carotenoid and the BChl to be completed faster. Additionally, this pathway explains the cross-peaks E and F observed at later times: upon population of S_2, this transfers energy either directly from S_2 to Q_x and then to Q_y and P^+ (peak E), or relaxes to S_1, and subsequently energy is transferred to Q_y and P^+.

The precise origin of the observed peaks and their dynamics remain not completely understood. Further analysis of the 2D spectra, combined with theoretical modeling, will help elucidate the physical origin of the peaks observed in the spectra and their dynamics. These results show that non collinear 2 color 2DES is a powerful and flexible technique to investigate energy transfer between spectrally separated transitions and characterize the relaxation of excited states in a multi-chromophoric system. Multiple pathways of energy transfer between the Car and the BChl have been identified. This would have been not possible with other techniques, such as transient absorption, which lack spectral resolution over the excitation axis.

3.4 Conclusions

This Chapter shows the application of 2DES to the investigation of the energy transfer dynamics in the oxidized reaction center from purple bacteria. 2DES is an excellent technique to probe the structure-function relationship of photosynthetic systems. In this Chapter, in particular, the capability of 2DES to discern closely spaced states has allowed us to see clear signatures of the two BChl on the two branches of the RC, establishing the presence of ultrafast energy transfer between them for the first time. Additionally, we have presented the first implementation of non-collinear 2 color 2D electronic spectroscopy. This technique has allowed us to look at the energy transfer pathways available for energy transfer between the Car and the BChl in the bacterial reaction center, a step of great importance since it precedes charge separation at the special pair. The feasibility of this technique opens up a large amount of possibilities in terms of investigating energy transfer dynamics and coupling between transitions that are spectrally separated. This is particularly relevant for photosynthetic PPCs, where the relative positions of the pigments and their coupling with other pigments and with the protein environment ensure the efficient and robust functioning of photosynthetic organisms under a variety of light conditions. The extension of this technique to other pulse sequences and to polarization studies is very promising for elucidating the structural and energetic changes occurring in individual PPCs upon variation in light intensity and environment.

Chapter 4

LhcSR: photoprotection in green algae

Contents

4.1 Introduction

Green algae are a group of eukaryotic organisms from which plants evolved [4]. Their evolutionary position as intermediates between cyanobacteria and plants makes them particularly interesting to study. The biochemical strategies adopted by algae for survival in aquatic environments are significantly different from those of plants. In particular, with respect to flexible NPQ (see Section 1.2), while for both plants and algae the formation of ΔpH is required for the induction of quenching, the pH sensing and quenching strategies adopted in the two organisms are different. In higher plants, a four-helix protein, PsbS, which does not bind pigments, is able to sense the change in pH and trigger a series of conformational changes that eventually lead to quenching. Quenching itself occurs at the level of the PSII antenna (either in the major light harvester, LHCII, or in the minor complexes, or in both). In algae, a single protein combines the functions of pH sensor and quencher: the Chl/Car-binding three-helix protein LhcSR [19]. In this respect, LhcSR, like OCP in cyanobacteria (see Chapter 2), is able to sense excess light and quench excess excitation. Interestingly, mosses, which are intermediates between algae and higher plants, possess genes for both LhcSR and PsbS, and the two proteins are responsible for independent quenching processes in this organism [184].

The role played by LhcSR in algal NPQ was identified in 2009 by Peers *et al.* [19]: the authors showed that a mutant of *C. reinhardtii* with decreased quenching capabilities was

lacking two of the three genes encoding for LhcSR. LhcSR is accumulated in algal cells acclimated to high light, and is substochiometric with respect to PSII (the ratio LhcSR/PSII is calculated to be 0.17 ± 0.11 in [20]). Due to the low amount of LhcSR3 in *C. reinhardtii*, difficulties in its isolation from light-acclimated cells exist because of its physicochemical similarities with other PPC [20]. An alternative approach is to study the recombinant protein: the encoding gene is expressed in bacteria and the apoprotein is refolded in vitro with pigments. This technique produces PPCs with analogous biochemical and spectral properties as the isolated proteins [185, 28].

While it has been shown that LhcSR presence is correlated with flexible NPQ (LhcSR is accumulated in high light and its presence is correlated with quenching of chlorophyll fluorescence [20]), the precise molecular mechanism of quenching and its relation with LhcSR quenching capabilities remain incompletely understood. This Chapter will be devoted to the spectroscopic investigation of LhcSR3 from *C. reinhardtii*. LhcSR3 is one of the isoforms of LhcSR encoded in the *C. reinhardtii* genome and in the following the terms LhcSR and LhcSR3 will be used interchangeably. The questions that we want to address are the following:

- Is LhcSR capable of quenching chlorophyll fluorescence in isolation, *i.e.* outside of the membrane/cell environment?
- Are LhcSR quenching capabilities related to its pH sensitivity?
- Is the quenching observed in isolated proteins the same as qE *in vivo*? What is the photophysical mechanism of qE in *C. reinhardtii* compared to plants?

4.2 LhcSR3 is a quencher

LhcSR is a three-helix transmembrane PPC, binding 6 Chl *a*, 1 Chl *b* (Chl *a* to Chl *b* ratio of 8), and two to three carotenoids (2 Lutein (Lut) and 1 Violaxanthin (Viola)) (see Fig. 4.1). LhcSR is able to bind Zeaxanthin (Zea) but the substitution of Zea for Viola does not change its spectroscopic properties [20] in contrast to other PPCs, such as CP29 [186]. LhcSR has nine acidic residues [187], four of which are sufficiently lumen-exposed, and thus are most likely responsible for the pH sensing capabilities of this PPC. Because of this, DCCD binding experiments have shown how the affinity for pH sensing of LhcSR is higher than in other PPCs, such as CP29 [20]. DCCD is a chemical agent that can covalently bind to a protein's protonatable residues, thus providing information on the potential pH sensing capabilities of the protein.

Previous time-resolved fluorescence experiments on LhcSR3 measured a very short fluorescence lifetime [20]. The average lifetime at pH 7.5 was measured to be 0.9 ns, much shorter than the one measured for CP29, which has an average lifetime of 3.5 ns [186]. Such a short value for the average lifetime was attributed to the strong contribution (65% amplitude) of the shortest lifetime component, measured to be less than 100 ps (below the instrument response function). Lowering the pH to 5.5 gave an even shorter average lifetime of 0.5 ns

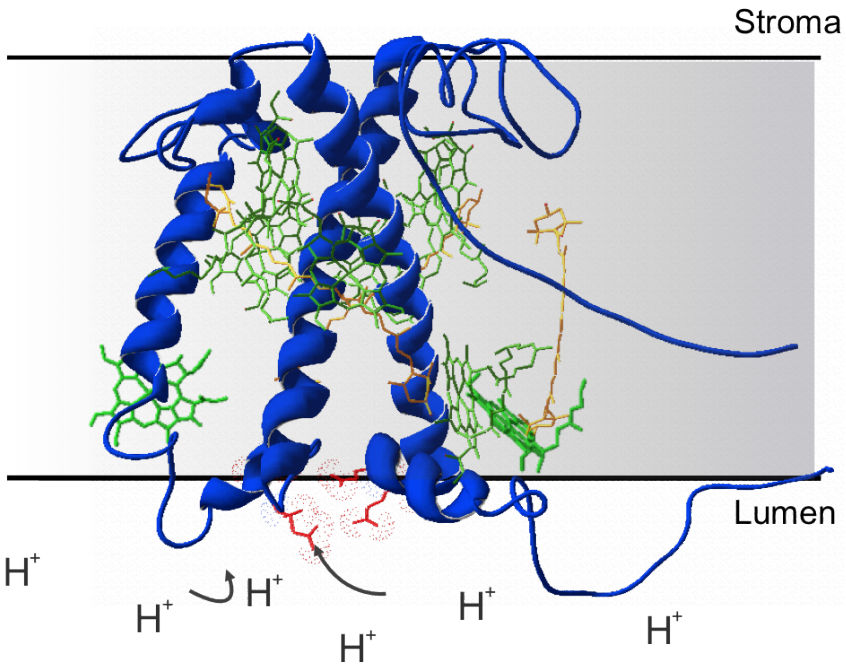

Figure 4.1: Structure of LhcSR3 as determined from the homology model to LHCII. LhcSR binds 6 Chl *a*, 1 Chl *b* and two to three carotenoids. For comparison, an LHCII monomer binds 8 Chl *a* , 6 Chl *b* and 4 carotenoids (1 neoxanthin, 1 violaxanthin and 2 luteins) [137]. The red residues represent lumen-exposed protonatable residues. These residues sense the ΔpH induced upon excess light absorption. Figure courtesy of Matteo Ballottari.

for LhcSR, while no difference was observed for the minor light-harvesting complex CP29. These results suggest the existence of two conformations for LhcSR at different pH values. A similar conformational switch between light-harvesting and quenching forms has been proposed for LHCII upon induction of a transthylakoid ΔpH [188], and supported by resonance Raman results [31].

However, it is unlikely that pH alone could induce a conformational switch in LhcSR. The pH sensitivity of LhcSR is in fact lower than for LHCII, as measured by steady-state fluorescence emission at 680 nm (Ballottari). Another factor that has been shown to play a role in inducing a dissipative state in LHCII and other PPCs [31, 3, 189, 190] is aggregation, which can be induced *in vitro* by varying detergent concentration.

In order to investigate the quenching capabilities of isolated LhcSR as a function of environmental parameters, we have performed TCSPC experiments on LhcSR varying detergent concentration and pH. We define as ”quenching conditions” the combination of low pH (to

mimic lumen acidification that occurs upon qE induction [191]) and low detergent concentration (to mimic aggregation conditions). We refer to these conditions as LL. "Light harvesting conditions" are instead obtained at neutral pH (pH 7.5) and high detergent concentration (above the critical micelle concentration, corresponding to 0.02% concentration for the detergent used, n-dodecyl-α-D-maltopyranoside (α-DM)). We refer to these conditions as HH.

Fig. 4.2 shows the fluorescence decay for reconstituted LhcSR3 wild type (WT) in high detergent at different values of pH, as measured by TCSPC (see Section 1.4). As can be observed in the figure, the decays are very similar at all values of pH. As further confirmation, we fit the decays to the sum of exponentials. The fit is optimized on the basis of the χ^2 parameter, and the best results are obtained by fitting to three lifetimes. The results of the fit are shown in Table 4.1. The longest lifetime component, of $\sim$4 ns, can be assigned to free pigments in solution, as determined by measuring the fluorescence decay for unfolded LhcSR3 (data not shown) and similar to what was concluded for isolated LHCII [192]. The average lifetime for recombinant LhcSR3 at all pH values is of $\sim$2.7 ns, confirming that pH alone is not sufficient to induce a dissipative state for LhcSR3 in high detergent. Similar results have been obtained on LHCII measuring its fluorescence lifetime as a function of pH at high detergent concentration: no variation from an average lifetime of $\sim$ 3.5 ns was observed [192].

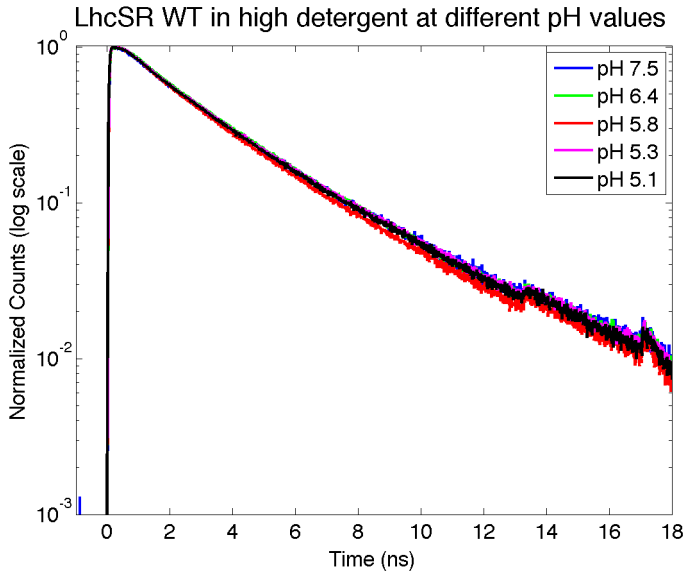

Figure 4.2: Fluorescence decays for LhcSR WT at different values of pH at high detergent concentration (0.03% α-DM). We observe very similar decay at all pH values.

Upon induction of quenching conditions (low pH, low detergent concentration - 0.003% α-DM) the lifetime of LhcSR3 WT is strongly decreased, shortening to an average value of $\sim$ 1 ns (see Fig. 4.3 and Table 4.2). A new lifetime component of $\sim$0.85 ns appears, while the long lifetime component assigned to free pigments is lost and the amplitude of the shortest component is highly increased (from 8% to 42%).

Sample	A_1	τ_1 (ns)	A_2	τ_2 (ns)	A_3	τ_3 (ns)	τ_{ave} **(ns)**
WT pH 7.5 High det	44%	4.04	47.5%	1.88	8.5%	0.21	**2.68**
WT pH 6.4 High det	48.8%	4.02	46.85%	1.87	4.3%	0.25	**2.85**
WT pH 5.8 High det	40%	4.04	51%	1.86	9%	0.19	**2.58**
WT pH 5.3 High det	44%	4.1	46%	1.84	9%	0.17	**2.68**
WT pH 5.1 High det	39.8%	4.22	50.5%	1.91	9.7%	0.19	**2.71**

Table 4.1: Amplitude and lifetime components for the fluorescence decays shown in Fig. 4.2: LhcSR WT in high detergent concentration (0.03% α-DM) at different values of pH.

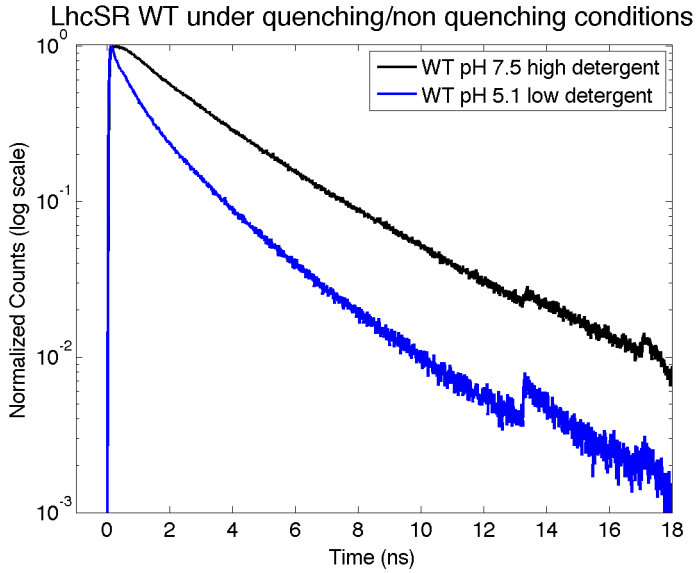

Figure 4.3: Fluorescence decay for LhcSR WT in light harvesting (pH 7.5, high detergent concentration) and quenching (pH 5.1, low detergent concentration) conditions. We observe a significant shortening of the decay in quenching conditions.

Sample	A_1	τ_1 (ns)	A_2	τ_2 (ns)	A_3	τ_3 (ns)	τ_{ave} **(ns)**
WT pH 7.5 High det	44%	4.04	47.5%	1.88	8.5%	0.21	**2.68**
WT pH 5.1 Low det	25%	2.5	33%	0.84	42%	0.14	**0.97**

Table 4.2: Amplitude and lifetime components for the fluorescence decays shown in Fig. 4.3: LhcSR WT in light harvesting (pH 7.5, high detergent concentration) and quenching conditions (pH 5.1, low detergent concentration).

On the basis of these results, we can conclude that LhcSR3 is an effective quencher of chlorophyll fluorescence upon induction of a dissipative state. Our data support the existence of two conformations, a light-harvesting conformation, with an average fluorescence lifetime of 2.7 ns, and a dissipative conformation, with 1 ns average lifetime, which require different pH and aggregation conditions. The existence of two separate conformations for LhcSR3

resembles what has been hypothesized for LHCII upon induction of quenching. Additionally, the group of Roberta Croce has recently performed fluorescence lifetime experiments on LhcSR embedded in synthetic polymers (NAPols) [187] and proposed the existence of a reversible switch between the two conformations (light harvesting and quenching).

4.3 The pH sensing capabilities of LhcSR

Work in the groups of Kris Niyogi and Roberto Bassi has identified the presence of conserved protonatable residues in the lumen-exposed portion of the protein. Mutation in whole *C. reinhardtii* cells on three of these protonatable sites (two glutamates and one aspartate are mutated to glutamine and asparagine, respectively) shows highly reduced quenching. The same type of mutation has been expressed *in vitro* by recombinant methods. We refer to this triple mutant as MUT. We have measured with TCSPC the fluorescence lifetime of MUT in light-harvesting and quenching conditions (as defined above) and compared the results with the WT. The decay curves are shown in Fig. 4.4, while the results of the fitting are given in Table 4.3.

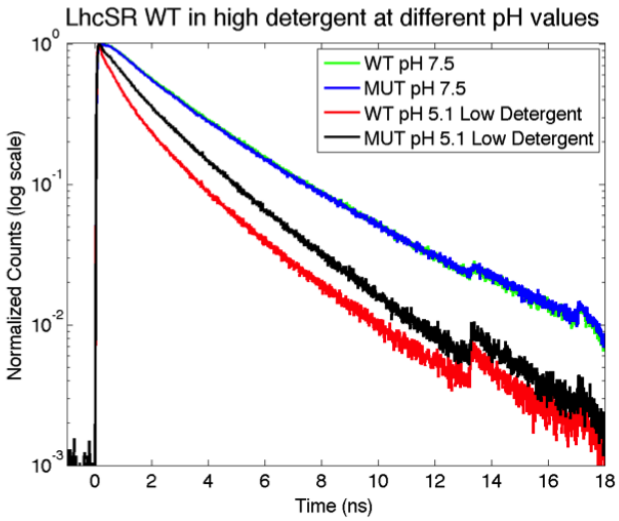

Figure 4.4: Fluorescence decay for LhcSR mutant MUT in light harvesting (pH 7.5, high detergent concentration) and quenching (pH 5.1, low detergent concentration) conditions and comparison with the decays in WT under the same conditions. We observe very similar decay for WT and MUT in light harvesting conditions, and a shortening of this decay in quenching conditions for both WT and MUT. The decay in MUT is longer than in WT in quenching conditions.

We find that in light-harvesting conditions the decays of WT and MUT are identical (on top of each other in Fig. 4.4). The fit gives for MUT an average lifetime of 2.63 ns, essentially the same obtained for WT. Upon induction of a dissipative state, the average lifetime of MUT drops to $\sim$1.4 ns, shorter than in light-harvesting conditions but longer than for quenched WT. The free pigment lifetime contribution is lost and we observe again three lifetime components: $\sim$ 2.6 ns, $\sim$ 1 ns and $\sim$ 140 ps, very similar to those obtained for WT. The

Sample	A_1	τ_1 (ns)	A_2	τ_2 (ns)	A_3	τ_3 (ns)	τ_{ave} (ns)
WT pH 7.5 High det	44%	4.04	47.5%	1.88	8.5%	0.21	**2.68**
MUT pH 7.5 High det	36%	4.37	54%	1.93	10%	0.18	**2.63**
WT pH 5.1 Low det	25%	2.5	33%	0.84	42%	0.14	**0.97**
MUT pH 5.1 Low det	41%	2.63	30%	0.99	29%	0.14	**1.4**

Table 4.3: Amplitude and lifetime components for the fluorescence decays shown in Fig. 4.4: LhcSR WT and MUT in light harvesting (pH 7.5, high detergent concentration) and quenching (pH 5.1, low detergent concentration) conditions.

amplitude of the shortest lifetime component is decreased in MUT (from 42% to 29%), while the longest component amplitude increases proportionally (from 25% to 41%).

It's important to note that some residual quenching is observed in the triple mutant even *in vivo*. In order to completely assess the contributions to quenching due to qE (as measured *in vivo*, and referred to in the remainder of this Chapter as qE-quenching), versus those due purely to concentration quenching [193], we would need a mutant completely unable to sense pH. The type of quenching observed in this mutant could then be assigned solely to concentration quenching, while in our *in vitro* measurements on MUT we need to take into account the presence of both concentration quenching and of some residual qE-quenching.

Nonetheless, the fact that the quenching abilities of LhcSR are reduced *in vitro* as well as *in vivo*, even for the triple mutant, allows us to conclude that the pH-sensing capabilities are related to its quenching properties, as the protonatable residues modulate the induction of a quenched/aggregated state. DCDD-binding experiments by our collaborators have shown that the pH-binding abilities of the MUT version of LhcSR are largely reduced. Given this observation, we make the assumption that all quenching observed in MUT is due to concentration quenching, while in WT we have contributions from both qE quenching and concentration quenching upon induction of dissipative conditions.

4.4 Molecular mechanisms of quenching in LhcSR

It is known that LhcSR plays a role in quenching in algae, and that LhcSR3 is able to perform Chl quenching even in isolation, however it is still unknown whether the quenching performed by LhcSR3 *in vitro* resembles *in vivo* quenching, and what the photophysical mechanism of quenching consists of. Section 1.3 reviews the proposed hypotheses for energy dissipation mechanisms in plants. Similar processes are thought to occur in algae as well.

We have performed transient absorption experiments in order to elucidate the possible mechanisms of quenching in this PPC. Upon excitation of the Chl Q_y transition, at 670 nm, we have investigated the energy transfer pathways in the visible and near-IR regions. The experimental setup is described in Section 1.4.2. Our pump pulse, centered at 670 nm, had a FWHM of 23 nm and was compressed to a duration of $\sim$ 45 fs, with an energy at sample of 15-25 nJ. Figure 4.5 shows the pump pulse spectrum, overlaid with the linear absorption spectrum of the sample. The probe is broadband white light, extending from 480 to 1100 nm,

generated in a 2 mm sapphire plate and filtered out with a short pass 750 nm (long pass 850 nm) filter to select the visible (near IR) portion of the spectrum. Pump and probe pulses are focused at the sample to a spot size of $\sim$ 260 μm and $\sim$ 125 μm, respectively. The sample is held in a 1 mm cuvette, and cooled down to $\sim$ 11-14 °C with a home built nitrogen cooling system.

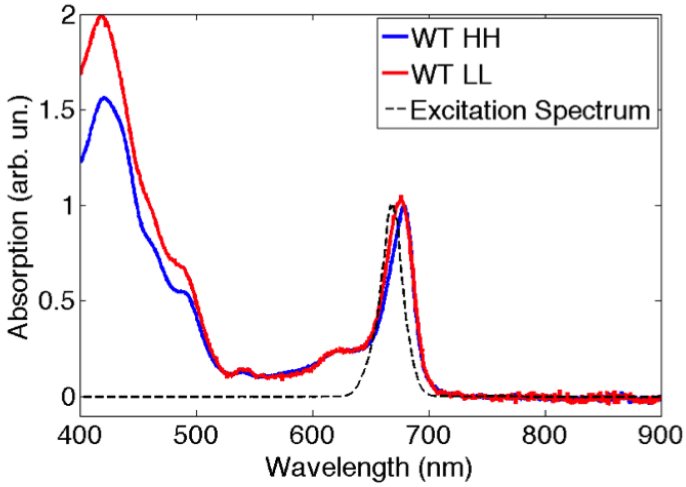

Figure 4.5: Linear absorption spectrum of LhcSR in light-harvesting conditions (blue solid line, high detergent concentration, high pH) and in quenching conditions (red solid line, low detergent concentration, low pH). The spectrum of the pump pulse, resonant with the Chl *a* Q_y transitions, is shown as a black dashed line.

Probing in the near infrared allows us to investigate the possibility of formation of a carotenoid radical cation. Given that LhcSR does not bind zeaxanthin, we looked for signatures of a lutein radical cation state, which has a maximum at 940 nm. We compared LhcSR in its two putative conformations, light-harvesting (at high detergent concentrations and pH 7.5, denoted in the following as HH) and quenching (at low detergent concentrations and pH 5.1, referred to as LL). Detergent removal can be obtained experimentally using SM-2 absorbent biospheres (BioRad), which are neutral macroporous polymeric spheres that absorb non-polar substances from aqueous solutions. The differences observed in WT between light-harvesting and quenching conditions can be assigned to quenching, with contributions both from qE quenching and concentration quenching due to aggregation in LL conditions. The differences observed in MUT, on the other hand, can be assigned purely to concentration quenching, under the assumption that all qE quenching is inhibited in the mutant on the protonatable sites.

Figure 4.6 reports the transient absorption traces for light-harvesting and quenching conditions in the near infrared region, which investigate the formation of carotenoid cation in WT and MUT LhcSR. The signal in the 920 - 980 nm region is always lower in quenching conditions (aggregation and lower pH) compared to light-harvesting conditions. The traces show contributions due to both Chl excited state absorption (only decay components) and Car^+ formation (rise and decay components). Traditionally, Car^+ formation is investigated

by looking at the difference traces between the kinetics in the dark and the kinetics in the light [27]. However, LhcSR shows a rise component attributable to Lut^+ formation under both light-harvesting and quenching conditions, therefore we report the traces and their relative fits (see Table 4.4) rather than their difference [20].

We observe the presence of a $\sim$ 5 ps rise time for LhcSR WT at 920, 940 and 960 nm, together with decay components, in HH conditions (a similar rise time of 6 ps was assigned to carotenoid radical cation formation in isolated CP29 by kinetic modeling of experimental data [194]. This rise time disappears or becomes faster upon induction of quenching conditions. The data for LhcSR MUT are similar, but at 960 nm in MUT we only observe decay components. The decay components become shorter upon induction of quenching conditions. At 980 nm, both WT and MUT show only decay components and no rise component can be detected. Induction of quenching conditions makes the shorter decay component faster at this wavelength, and the longer component slower (see Table 4.4). Given its spectral position (centered around 940 nm) and value (around 5 ps) we hypothesize the assignment of the observed rise component to the formation of a lutein radical cation. At 980 nm, no signatures of the cation are observed, and we only observe the decay of the Chl excited state. This is consistent with the lack of zeaxanthin in our reconstituted proteins, as zea has been shown to not play an essential role in this process in LhcSR [20]. We interpret these results as follows: while carotenoid cation formation is a pathway that is always open in LhcSR (even in light-harvesting conditions), upon induction of quenching conditions new dissipative channels open. These channels are competitive with formation of the cation and Chl excited state population, which explains the reduction/disappearance of the rise component and the reduction in the overall signal.

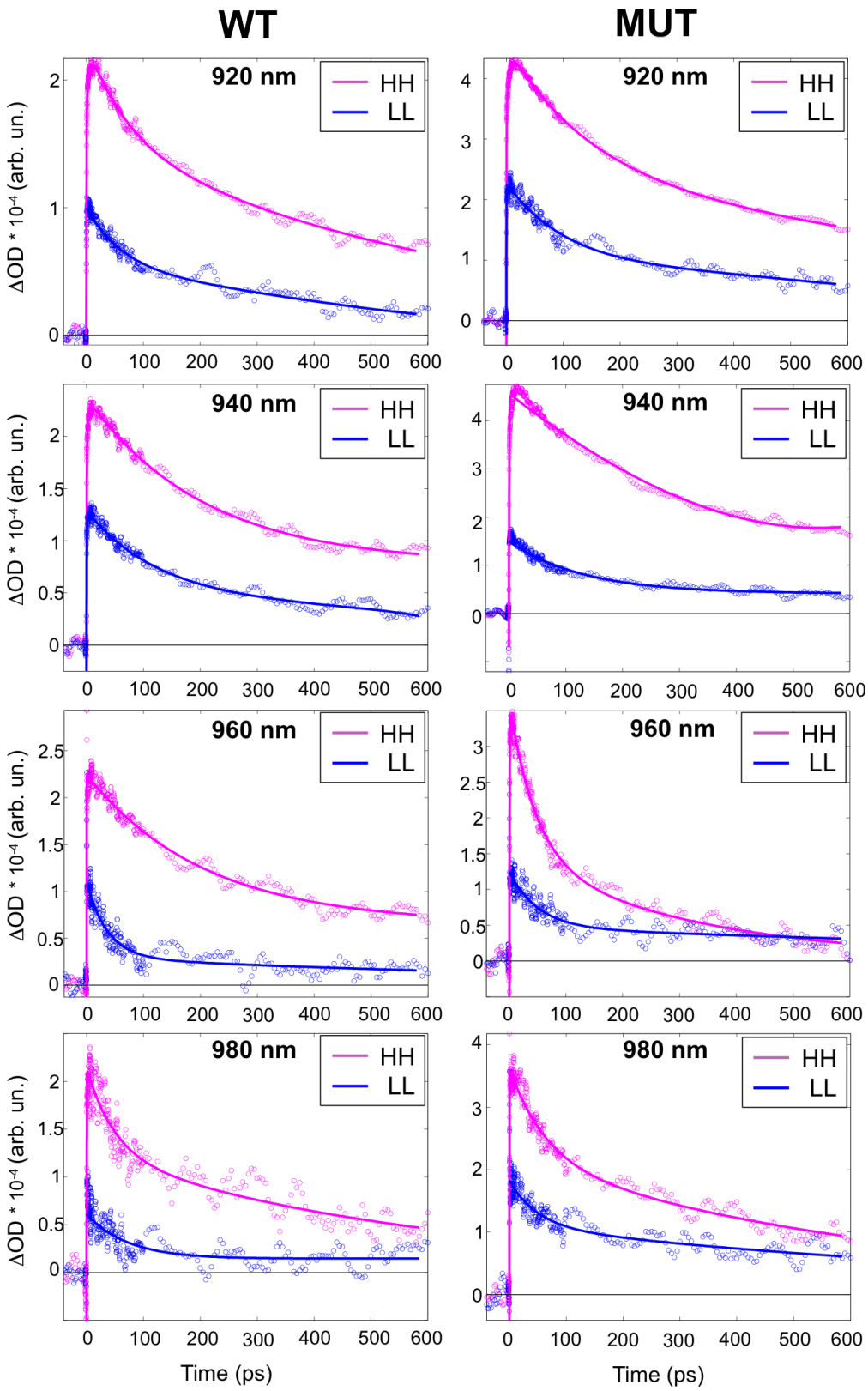

Figure 4.6: Transient absorption traces at selected wavelengths in the near infrared region for reconstituted WT (*left*) and MUT (*right*) LhcSR, upon excitation at 670 nm (Chl Q_y transition). The probe wavelengths are (top to bottom): 920 nm, 940 nm, 960 nm, 980 nm.

Wavelength	WT		MUT	
	HH	LL	HH	LL
920 nm	τ_1 = 0.35 ps ± 0.03 ps A_1=-0.81 ± 0.04	τ_1 = 0.787 ps ± 0.18 ps A_1 = -0.38 ± 0.07	τ_1 = 0.32 ps ± 0.02 ps A_1=-0.64 ± 0.02	τ_1 = 0.37 ps ± 0.03 ps A_1 = -0.802 ± 0.08
	τ_2 = 5.05 ps ± 1 ps A_2=-0.24 ± 0.02	τ_2 = 41.6 ps ± 9 ps A_2 = 0.37 ± 0.05	τ_2 = 5.1 ps ± 0.5 ps A_2=-0.26 ± 0.02	τ_2 = 3.04 ps ± 2 ps A_2 = -0.14 ± 0.04
	τ_3 = 70.6 ps ± 12 ps A_3=0.35 ± 0.04	τ_3 = 441 ps ± 51 ps A_3 = 0.60 ± 0.05	τ_3 = 135 ps ± 9 ps A_3=0.44 ± 0.01	τ_3 = 72 ps ± 9 ps A_3 = 0.44 ± 0.03
	τ_4 = 678 ps ± 62 ps A_4=0.715 ± 0.04		τ_4 = 1072 ps ± 0.8 ps A_4=0.60 ± 0.01	τ_4 = 781 ps ± 1 ps A_4 = 0.52 ± 0.02
940 nm	τ_1 = 0.37 ps ± 0.04 ps A_1=-1.04 ± 0.05	τ_1 = 0.2 ps ± 0.02 ps A_1 = -3.26 ± 0.03	τ_1 = 0.35 ps ± 0.03 ps A_1=-0.99 ± 0.03	τ_1 = 0.14 ps ± 0.03 ps A_1 = -1.91 ± 0.08
	τ_2 = 4.16 ps ± 1.3 ps A_2=-0.18 ± 0.03	τ_2 = 3.47 ps ± 1.9 ps A_2 = -0.17 ± 0.03	τ_2 = 5.06 ps ± 0.6 ps A_2=-0.31 ± 0.03	τ_2 = 57 ps ± 0.9 ps A_2 = 0.49 ± 0.06
	τ_3 = 206 ps ± 17 ps A_3=0.68 ± 0.015	τ_3 = 80 ps ± 22 ps A_3 = 0.45 ± 0.09	τ_3 = 156 ps ±11 ps A_3=0.51 ± 0.01	τ_3 = 745 ps ± 205 ps A_3 = 0.48 ± 0.07
	τ_4 = + inf A_4=0.33 ± 0.02	τ_4 = 644 ps ± 185 ps A_4=0.54 ± 0.1	τ_4 = 1307 ps ± 0.6 ps A_4=0.54 ± 0.02	
960 nm	τ_1 = 0.1 ps ± 0.02 ps A_1=-0.75 ± 0.06	τ_1 = 32 ps ± 5 ps A_1 = 0.36 ± 0.02	τ_1 = 0.406 ps ± 0.03 ps A_1=-1.2 ± 0.03	τ_1 = 0.1 ps ± 0.05 ps A_1 = -0.21 ± 0.1
	τ_2 = 4.9 ps ± 2.6 ps A_2=-0.1 ± 0.025	τ_2 = 773 ps ± 0.05 ps A_2 = 0.142 ± 0.018	τ_2 = 50 ps ± 7.3 ps A_2=0.6 ± 0.07	τ_2 = 44.5 ps ± 5.8 ps A_2 = 0.31 ± 0.02
	τ_3 = 107 ps ± 17 ps A_3=0.68 ± 0.015		τ_3 = 345 ps ± 62 ps A_3=0.51 ± 0.01	τ_3 = 1184 ps ± 0.1 ps A_3 = 0.48 ± 0.07
	τ_4 = 946 ps ± 2 ps A_4=0.46 ± 0.02			
980 nm	τ_1 = 0.37 ps ± 0.04 ps A_1=-1.5 ± 0.1	τ_1 = 35 ps ± 7 ps A_1 = 0.53 ± 0.04	τ_1 = 0.28 ps ± 0.04 ps A_1=-0.68 ± 0.04	τ_1 = 49 ps ± 15 ps A_1 = 0.2 ± 0.02
	τ_2 = 48 ps ± 16 ps A_2=0.38 ± 0.07	τ_2 = 1433 ps ± 0.01 ps A_2 = 0.203 ± 0.03	τ_2 = 63 ps ± 14 ps A_2=0.35 ± 0.06	τ_2 = 996 ps ± 0.5 ps A_2 = 0.3 ± 0.02
	τ_3 = 596 ps ± 161 ps A_3=0.53 ± 0.11		τ_3 = 702 ps ± 148 ps A_3=0.519 ± 0.08	

Table 4.4: Kinetic fits for the transient absorption traces in the near infrared of Fig. 4.6 (the fits are on the normalized curves).

No significant differences are observed between the WT and the MUT sample, except at 960 nm, where in MUT we only observe decay components in both light-harvesting and quenching conditions. This suggests that, while Car^+ formation contributes to quenching, its origin can be correlated mostly to concentration quenching rather than to qE (if it was solely due to qE, we would expect it to disappear or strongly decrease in the mutant). The difference kinetics at 960 nm (data not shown) show a rise component in WT of $\sim$ 11 ps that is completely lost in MUT, which could indicate that the rise observed in WT is due to cation formation correlated to qE quenching (Lut^+ has been observed to peak around 960 nm in LhcSR3 in [20]). However, we don't observe the same behavior at any other wavelength, and it is known that the spectral width of Car^+ is larger than $\sim$ 20 nm [20]. Therefore, we have no evidence from our data that Lut^+ formation can be directly correlated to qE quenching in LhcSR, but rather we propose that it is constitutive in LhcSR due to Chl-Car heterodimer formation. It is important to notice that this conclusion is derived under the assumption that MUT shows no residual qE quenching, which is not completely accurate *in vivo*.

Nevertheless, we observe that upon induction of quenching conditions, new dissipative pathways open up. In order to investigate the molecular origin of these pathways, we have performed transient absorption experiments with excitation of Chl *a* Q_y transition and probing in the visible spectral region (500-700 nm). These measurements investigate a possible involvement of energy transfer to a carotenoid or the formation of an excitonic state between a Chl and a Car. Measurements in the visible are made more difficult by strong photobleaching effects (discussed later) and by the fact that Chl excited state absorption extends over the whole visible spectrum, making the detection of carotenoid signals on top of it complicated.

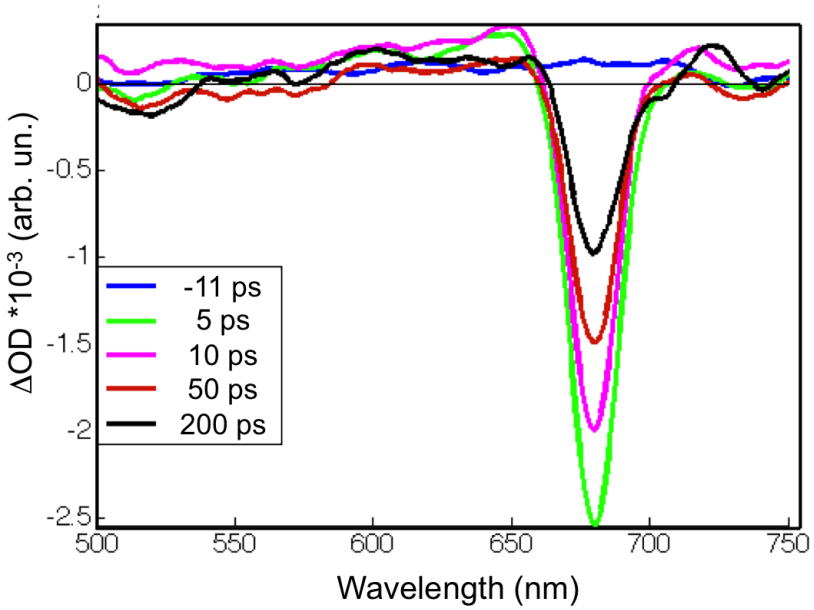

Figure 4.7: Transient absorption spectra obtained on WT LhcSR3 in LL (quenching) conditions at selected delay times, upon excitation at 670 nm.

We have collected transient absorption data using both spectrally-resolved detection on a CCD (see Introduction Chapter) and wavelength-specific data on a Silicon photodiode. Spectrally resolved data obtained on the CCD on the WT sample in LL conditions are shown in Fig. 4.7. We observe the strong negative signal due to Chl *a* bleach/stimulated emission. For wavelengths below $\sim$ 665 nm and above $\sim$ 710 nm, we observe a positive signal which we can assign to Chl excited state absorption. Below 535 nm, an additional negative signal is observed, which we can attribute to bleach/stimulated emission of carotenoids. Data obtained on the WT sample in HH (light harvesting) conditions is similar, only more noisy (data not shown), which complicates the comparison of the sample under the two different conditions.

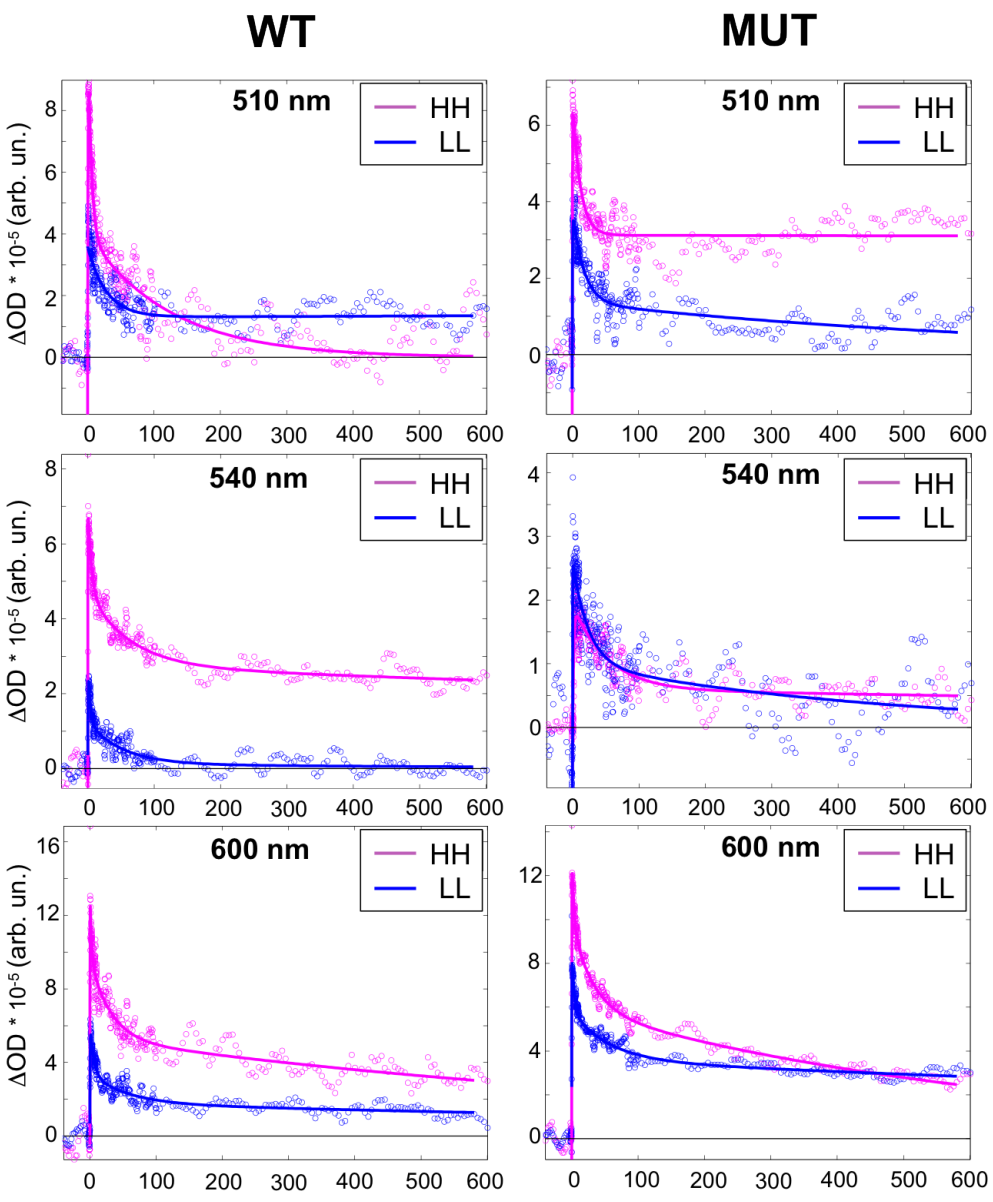

Figure 4.8: Transient absorption traces at selected wavelengths in the visible region for reconstituted WT (*left*) and MUT (*right*) LhcSR, upon excitation at 670 nm (Chl Q_y transition). The probe wavelengths are (*top to bottom*): 510 nm, 540 nm, 600 nm.

Wavelength	WT		MUT	
	HH	LL	HH	LL
510 nm	τ_1 = 0.64 ps ± 0.12 ps A_1=-1.3 ± 0.15	τ_1 = 15.9 ps ± 2.7 ps A_1 = 0.526 ± 0.04	τ_1 = 0.35 ps ± 0.06 ps A_1=-1.16 ± 0.11	τ_1 = 0.54 ps ± 0.14 ps A_1 = -0.89 ± 0.1
	τ_2 = 4.9 ps ± 1 ps A_2 = 0.86 ± 0.13	τ_2 = 2725 ps ± 0.01 ps A_2 = 0.313 ± 0.015	τ_2 = 12 ps ± 1.9 ps A_2 = 0.51 ± 0.03	τ_2 = 16.4 ps ± 3.8 ps A_2 = 0.585 ± 0.05
	τ_3 = 124 ps ± 20 ps A_3 = 0.445 ± 0.04		τ_3 = + inf A_3 = 0.43 ± 0.01	τ_3 = 659 ps ± 214 ps A_3 = 0.328 ± 0.04
540 nm	τ_1 = 0.126 ps ± 0.023 ps A_1=-0.85 ± 0.07	τ_1 = 0.38 ps ± 0.12 ps A_1 = -1.06 ± 0.17	τ_1 = 0.36 ps ± 0.11 ps A_1 = -0.928 ± 0.15	τ_1 = 0.137 ps ± 0.071 ps A_1 = -0.38 ± 0.14
	τ_2 = 12.5 ps ± 1.5 ps A_2 = 0.36 ± 0.02	τ_2 = 3.7 ps ± 1.1 ps A_2 = 0.72 ± 0.13	τ_2 = 50.1 ps ± 8.1 ps A_2 = 0.528 ± 0.03	τ_2 = 24 ps ± 9 ps A_2 = 0.37 ± 0.06
	τ_3 = 1078 ps ± 125 ps A_3 = 0.426 ± 0.01	τ_3 = 66.7 ps ± 12.4 ps A_3 = 0.475 ± 0.06	τ_3 = 2139 ps ± 1 ps A_3 = 0.26 ± 0.03	τ_3 = 461 ps ± 221 ps A_3 = 0.23 ± 0.06
600 nm	τ_1 = 0.12 ps ± 0.03 ps A_1=-0.83 ± 0.1	τ_1 = 0.452 ps ± 0.09 ps A_1 = -0.737 ± 0.11	τ_1 = 0.205 ps ± 0.023 ps A_1 = -0.99 ± 0.06	τ_1 = 0.183 ps ± 0.02 ps A_1 = -0.55 ± 0.04
	τ_2 = 2.36 ps ± 1.2 ps A_2 = 0.23 ± 0.05	τ_2 = 5.1 ps ± 1.7 ps A_2 = 0.47 ± 0.08	τ_2 = 3.14 ps ± 1 ps A_2 = 0.23 ± 0.03	τ_2 = 3.9 ps ± 1 ps A_2 = 0.27 ± 0.03
	τ_3 = 31 ps ± 6 ps A_3 = 0.26 ± 0.03	τ_3 = 55 ps ± 20 ps A_3 = 0.26 ± 0.08	τ_3 = 31.3 ps ± 6 ps A_3 = 0.275 ± 0.02	τ_3 = 55 ps ± 9 ps A_3 = 0.22 ± 0.02
	τ_4 = 1034 ps ± 0.1 ps A_4 = 0.315 ± 0.015	τ_4 = 1748 ps ± 0.3 ps A_4 = 0.28 ± 0.02	τ_4 = 659 ps ± 81 ps A_4 = 0.42 ± 0.01	τ_4 = 2432 ps ± 0.1 ps A_4 = 0.35 ± 0.01

Table 4.5: Kinetic fits for the transient absorption traces in the visible shown in Fig. 4.8 (the fits are on the normalized curves).

Fig. 4.8 shows traces obtained at selected wavelengths in the visible region below 600 nm. Table 4.5 reports the corresponding fits on the normalized kinetic curves. As can be observed in the Figure, the data are noisy, especially at 510 and 540 nm, where Car and Chl signals overlap. For the WT sample, we observe at 540 and 600 nm a very similar decay, with a reduction of the amplitude in LL conditions. At 510 nm WT, the decay to the ground state is much faster in HH conditions (5 ps and 124 ps), and in LL conditions a new long lived component appears (2725 ps). For the MUT sample, at 510 nm, we observe the presence of a long lived component in HH conditions, which disappears in LL conditions. At 540 nm, the signal amplitudes are similar under both conditions, but the decay is faster in LL conditions (the longest decay component shortens from 2140 ps to 460 ps). At 600 nm, the situation is reversed and we observe a faster decay to the ground state in HH conditions (660 ps in HH versus 2430 ps in LL).

Noise and experimental difficulties hamper the quantitative comparison of the two conformations for both WT and MUT samples. LhcSR is very sensitive to irreversible photobleaching effects, which makes the experimental measurement of dynamics complicated. Figure 4.9 shows the photobleaching effects on WT over a 5 min 35 sec period (typical duration of a single scan for our measurements). The stage is fixed at T=10 ps and the transient absorption signal is measured at 680 nm (maximum of the bleach region, where the photobleaching effects are worst). The signal decays by $\sim$ 35% over the time period of a scan collection, indicating high instability of the sample under the laser pulse.

Additionally, LhcSR is an unstable protein in isolation. Its melting temperature (estimate of the temperature at which half of the proteins are unfolded) is much lower than the melting

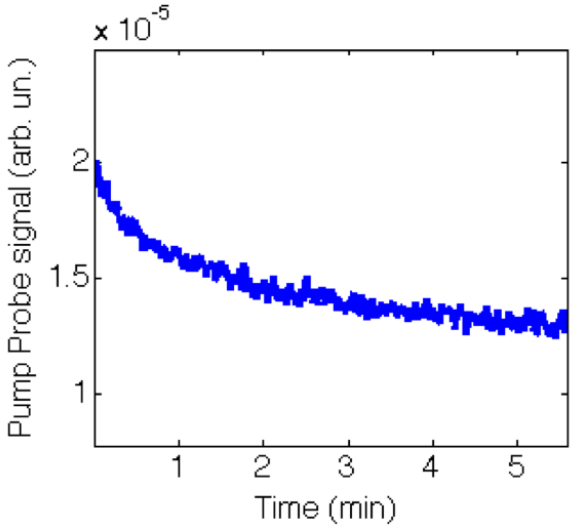

Figure 4.9: Transient absorption signal of LhcSR WT upon excitation at 670 nm and probing at 680 nm, measured over a 5 min 35 sec period, for a fixed value of delay of T=10 ps. The decay of the signal in time shows the effect of irreversible photobleaching effects.

temperature of LHCII (37.8°C for LhcSR versus 77°C for LHCII [195]) (Ballottari). One possible solution to reduce photobleaching could be the use of a flowing system that would allow new sample at each new excitation pulse. However, that would require not only high flow velocities, but also a large amount of sample, which is extremely hard to produce. Both LhcSR3 isolation from *C. reinhartdii* cells and LhcSR3 reconstruction are extremely challenging, therefore the samples used in our experiments have low OD (0.08-0.15 at 675 nm), the amount of sample is quite limited ($\sim$ 25-50 μL) and some gets lost during sample mixing with buffer. These factors make this experiment challenging, and a quantitative comparison between the traces almost impossible. We don't observe the presence of any rise component in our signals in the Car region (at 510 or 540 nm), so we can exclude the energy transfer between Chl and Car S_1 on a few picosecond timescale, as has been observed in LHCII aggregates in [31]. However, we cannot draw conclusions about the formation of excitonic states between a Chl and a Car. The formation of an excitonic state has been observed as an instantaneous population of Car S_1 states upon Chl excitation in intact thylakoids [40] and in LHCII [34] in the difference signal between quenched and unquenched conditions. Due to the noise in our data and the photobleaching of the sample, we cannot make a similar analysis. In Section 4.5, we will propose a possible solution to the photobleaching problem. Until detailed quantitative information (amplitude and lifetime of the signals) can be extracted with precision from these measurements, it is very difficult to draw conclusions about the possible photophysical mechanism of quenching in LhcSR and whether this resembles the type of quenching observed *in vivo*.

4.5 Conclusions and future work

LhcSR is both a pH sensor and a quencher, and has an evolutionary importance being present in green algae and mosses and having been lost in plants. In this Chapter, we have presented a spectroscopic investigation of the quenching properties of reconstituted LhcSR3 WT and of its mutant MUT, with diminished pH sensitivity. We have shown that under quenching conditions LhcSR3 is capable of effectively quenching *in vitro* Chl fluorescence. The investigation of the mutant on three of the lumen-exposed protonatable sites has allowed us to prove that these pH-sensitive residues modulate the amount of quenching that LhcSR3 can perform, both *in vivo* and *in vitro*. Due to experimental challenges, we are not able to draw any definitive conclusion about the possible quenching mechanisms occurring in LhcSR. We observe that upon induction of quenching conditions, the signal amplitude decreases. This suggests the opening of one or more new dissipative channels upon induction of quenching conditions. Since we observe formation of Car^+ in both WT and MUT, we cannot conclude that it is positively correlated with qE quenching in LhcSR. Additionally, we cannot make conclusions on possible energy transfer pathways or excitonic states between Chl and Car. The transient absorption measurements in the visible should be repeated adding a glucose catalase oxidase enzyme to the sample, which consumes oxygen, thus reducing photobleaching effects.

Further work is needed to elucidate the energy transfer pathways of LhcSR in its two conformations. Broadband two-dimensional electronic spectroscopy on LhcSR in light harvesting and quenching conditions will allow us to distinguish the energy transfer pathways in the two configurations The comparison with MUT will allow us to subtract out the energy transfer pathways that are due to aggregation (upon detergent removal) and that are not directly correlated with qE. The combination of these experiments with polarization-dependent two-dimensional electronic spectroscopy experiments on LhcSR (similar to the measurements performed on CP29 by Ginsberg *et al.* in our group [50]) in the quenching vs. light harvesting conditions will infer the structural differences between the two conformations giving rise to potentially different dissipation pathways. These experiments will help answer the bigger question of what are the conformational changes occurring in isolated PPCs upon induction of a dissipative state.

Chapter 5

Conclusions

This thesis discusses the application of different ultrafast spectroscopic techniques to the investigation of the energy transfer dynamics in PPCs involved in the first steps of photosynthesis: efficient collection of solar energy, efficient transfer to the location of charge separation, and efficient and safe energy dissipation in case of excess light absorption. All of these processes occur on ultrafast timescales (fs-ps) and over large bandwidths (over the visible and near infrared spectral regions). Transient absorption and 2D electronic spectroscopy are ideal techniques to study these processes because they follow the evolution of excited states with high temporal resolution and over broad spectral regions. Additionally, time-resolved fluorescence spectroscopy distinguishes between different conformations of a PPC upon a change in the local environmental conditions, due to the technique sensitivity to the lifetime of excited states.

The aim of ultrafast photosynthesis research is to understand the governing principles underlying natural photosynthetic systems so they they can inform the development of artificial devices and the engineering of crops for production of biofuels [196, 197]. The driving force is the ever-growing energy demand on our planet, which cannot be sustainably satisfied by fossil fuels. Sunlight is the most abundant energy source readily available, and it powers all of natural photosynthesis. While natural photosynthetic systems are quite inefficient in terms of sunlight absorbed versus energy stored, they are extremely efficient at functioning under a variety of light and environmental conditions, and able to repair themselves. These properties make them extremely interesting to investigate.

The first steps of photosynthesis correspond to the collection of sunlight and efficient transfer of the excitation energy to the location of conversion into chemical energy. Antenna complexes in photosynthetic systems are optimized to maximally absorb light energy over the spectral range available to the particular organism, and to funnel such energy very efficiently to the reaction center. Additionally, antenna complexes and specialized PPCs provide photoprotection capabilities in the event of excess light absorption (we have discussed two examples in this thesis: a specialized PPC from cyanobacteria in Chapter 2, and a PPC able to switch between light harvesting and quenching functions in green algae in Chapter 4). The structure, size and composition of antenna systems is highly variable, and depends on the specific organism and the environmental conditions of growth. A good artificial antenna sys-

tem should satisfy the following requirements [196]: 1) uniform absorption cross the solar spectrum; 2) efficient transfer of excitation energy to the reaction center; 3) fast and reversible switching to a dissipative state in case of excess absorption.

Reaction centers are the PPCs specialized for charge separation and unidirectional flow of electrons (in Chapter 3 we have investigated the reaction center from purple bacteria). Their molecular construction is highly conserved across different species, as it allows efficient collection of excitation energy from the antenna, efficient charge separation and efficient and unidirectional flow of electrons, largely avoiding recombination of charge-separated states. Even in case of recombination, safety mechanisms are in place even in reaction centers, for example in the form of Cars, which can quench damaging species. The steps in this process are kinetically regulated by a fine tuning of the different lifetimes and steps of energy transfer, to minimize the probability of damage. Still, even in the presence of damage, plants and other photosynthetic organisms have strategies in place to self-repair their photosynthetic system [198, 199]. An artificial reaction center would satisfy the following requirements [196]: 1) easy and efficient interfacing with the antenna system to accept excitation energy; 2) efficient and stable electron transfer; 3) robust to recombination of the charge-separated states.

Successful implementations of artificial antenna/reaction center complexes have made use of components such as tetrapyrroles, coumarin antenna chromophores, phorphyrins, hexads and/or fullerenes [200, 201, 202, 203].

Another photosynthesis-related research field that is in continuous development is biofuel research. The possibility to utilize the sucrose produced by natural crops for biofuel production (usually ethanol) brings along good prospects for alternatives to fossil fuels. So far in our discussion we have focused our attention only on the first steps of photosynthesis. A more complete description of photosynthesis includes the absorption of solar energy, followed the removal of electrons from water and the use of these electrons to reduce carbon dioxide into carbohydrates. While the first steps of photosynthesis have a very high quantum efficiency ($\sim$ 100% in optimal conditions [132] for the amount of absorbed photons that produces stable charge separation events), the overall efficiency of photosynthesis is around only a few percents. A recent review [204] investigates the main inefficiencies of natural photosynthesis and potential ways of overcoming these inefficiencies. A lot of the solar energy is lost upon absorption. Cars and Chl only absorb in the visible portion of the solar spectrum (see Sec. 1.1), thus making the organism transparent to approximately 50% of the incident solar energy [204]. One way of improving the overall efficiency of light collection would be to incorporate new artificial pigments or tune the light absorption properties of natural pigments (by modified interactions with the protein, for example) to cover the entirety of the solar spectrum [204].

Due to these inefficiencies, a lot more needs to be developed before reaching the same levels of robustness and efficiency that natural photosynthetic systems achieve. Continuous research in natural photosynthesis will allow us to design and engineer devices that are possibly even more energetically advantageous than what can be found in nature.

In order to more accurately derive the governing principles behind natural photosynthesis, it would be interesting to use the same experimental techniques discussed in this thesis

to look at systems that are much larger in size than isolated PPCs, exploiting their ability of discerning energy transfer over broad bandwidths with ultrafast time resolution. Transient absorption spectroscopy has been applied successfully to larger scale systems such as thylakoid membranes [40, 27] and even whole leaves [205]. However, these experiments are complicated by the fact that the increased size of the samples under investigations carries significant scattering problems, as the size of the particles becomes comparable with the wavelength of light used. Due to the technical difficulties associated with this experiment, an extension to 2D may be experimentally challenging. 2DES has been used to investigate energy transfer pathways in larger scale systems such as live cells [206]. However, the number of overlapping transitions in these systems is very high. Nonetheless, it would be valuable to use polarization sequences (an example is shown in Chapter 3) to get to the structure of molecular systems and elucidate which particular set of pigments is involved in forming dissipative states. This could help locate the site (sites) of quenching in the thylakoid membrane, which is the smallest isolatable unit capable of performing quenching.

Another direction for technique development is similar to what has been recently developed in our lab for fluorescence lifetime spectroscopy by Amarnath *et al.* [207] and applied to algae [207] and *Arabidopsis* leaves [Sylak-Glassman]. The ability of taking fluorescence snapshots at different times during the acclimation and relaxation process of plants and algae, combined with mutant studies, has helped the elucidation of different contributions to quenching appearing and disappearing on different timescales. A similar 'light acclimation' time axis can be applied to transient absorption. This would allow us to investigate the precise physical mechanism(s) of quenching and their appearance at different points in the acclimation to light, together with their relative timescale of disappearance upon recovery of quenching. The implementation of this new technique has started in our lab, but it is complicated by the experimental issues related to scattering from the thylakoid samples mentioned above.

One particular question that would be interesting to address is the interplay between PsbS and zeaxanthin in the induction/relaxation of qE in plants. Recent fluorescence snapshot experiments by Sylak-Glassman on whole leaves have shown how the interplay between these two components is what allows wild-type *Arabidopsis* plants to be so efficient at turn-on, maintenance and rapid turn-off of quenching. When one of these components is missing, a reduced amount of quenching is observed, together with different dynamics of induction/relaxation. In order to better understand the interplay between PsbS and zea, we propose to use a transient absorption snapshot technique on thylakoids isolated from *Arabidopsis* wild-type, *npq1*, *npq4* and *npq1npq4* mutants. *npq1* is a mutant that lacks the ability of synthesizing zeaxanthin from violaxanthin [208]; *npq4* lacks PsbS [209]; *npq1npq4* is the double mutant lacking both PsbS and zea [210]. These experiments could help elucidate what is the photophysical mechanism of interaction between PsbS and zea that leads to excess energy dissipation. The results can further aid membrane modeling, by establishing the number/positioning of quenching sites. In particular, the specific questions that we are interested in addressing, are: 1) in the *npq4* mutant, can you still observe the formation of excitonic states between Chl and Cars, or of carotenoid cations (see Section 1.3), or is PsbS required for induction of those interactions? Are these cations/states enhanced at all by the putative conformational change induced by PsbS and so we do not expect to observe them in an *npq4*

mutant?[i] Or are the interactions taking place between Chl and Car completely different in this case? 2) In the mutant *npq1*, which lacks zeaxanthin, can you see formation of excitonic states in membranes due to other Cars such as lutein and/or violaxanthin, as observed isolated PPCs [211, 77]? 3) In the double mutant *npq1npq4*, can you observe similar signatures for quenching? If quenching only depended on the particular interaction between PsbS and zea, we should not see the same signatures. However, we cannot exclude the presence of other dissipative channels, and it would be interesting to look at the relative amplitude of these alternative channels that might be present, but just less important, in wild-type plants. Additionally, being able too look at all of these signals as a function of acclimation time will allow us to see at which point in the induction of quenching different pathways appear, and on what timescales they become less relevant if other pathways become available.

[i] Previous measurements on *npq4* thylakoids by Holt *et al.* [27] have shown no cation formation upon induction of quenching.

Bibliography

[1] B. Demmig-Adams and W. W. Adams, "Photoprotection in an ecological context: the remarkable complexity of thermal energy dissipation," *New Phytologist*, vol. 172, no. 1, pp. 11–21, 2006.

[2] K. K. Niyogi and T. B. Truong, "Evolution of flexible non-photochemical quenching mechanisms that regulate light harvesting in oxygenic photosynthesis," *Current Opinion in Plant Biology*, vol. 16, no. 3, pp. 307 – 314, 2013.

[3] H. Kirchhoff, "Molecular crowding and order in photosynthetic membranes," *Trends in plant science*, vol. 13, no. 5, pp. 201–207, 2008.

[4] R. E. Blankenship, *Molecular mechanisms of photosynthesis*. Wiley. com, 2008.

[5] H. A. Frank and R. J. Cogdell, "Carotenoids in photosynthesis," *Photochemistry and Photobiology*, vol. 63, no. 3, pp. 257–264, 1996.

[6] T. Polívka and V. Sundström, "Ultrafast dynamics of carotenoid excited states - From solution to natural and artificial systems," *Chemical Reviews*, vol. 104, pp. 2021–2071, APR 2004.

[7] C. Külheim, J. Ågren, and S. Jansson, "Rapid regulation of light harvesting and plant fitness in the field," *Science*, vol. 297, no. 5578, pp. 91–93, 2002.

[8] Z. Li, S. Wakao, B. B. Fischer, and K. K. Niyogi, "Sensing and responding to excess light," *Annual Review of Plant Biology*, vol. 60, no. 1, pp. 239–260, 2009.

[9] E. H. Murchie and K. K. Niyogi, "Manipulation of photoprotection to improve plant photosynthesis," *Plant Physiology*, vol. 155, no. 1, pp. 86–92, 2011.

[10] J. M. Anderson, W. S. Chow, and Y.-I. Park, "The grand design of photosynthesis: acclimation of the photosynthetic apparatus to environmental cues," *Photosynthesis Research*, vol. 46, no. 1-2, pp. 129–139, 1995.

[11] A. Krieger-Liszkay, "Singlet oxygen production in photosynthesis," *Journal of Experimental Botany*, vol. 56, no. 411, pp. 337–346, 2005.

[12] A. Krieger-Liszkay, C. Fufezan, and A. Trebst, "Singlet oxygen production in photosystem II and related protection mechanism," *Photosynthesis Research*, vol. 98, no. 1-3, pp. 551–564, 2008.

[13] M. Ballottari, J. Girardon, L. Dall'Osto, and R. Bassi, "Evolution and functional properties of Photosystem II light harvesting complexes in eukaryotes," *Biochimica et Biophysica Acta (BBA) - Bioenergetics*, vol. 1817, no. 1, pp. 143 – 157, 2012.

[14] D. Sapozhnikov, T. Krasovskaya, and A. Maevskaya, "Change in the interrelationship of the basic carotenoids of the plastids of green leaves under the action of light," *Dokl. Akad. Nauk SSSR*, vol. 113, no. 2, pp. 465–467, 1957.

[15] H. Yamamoto, T. Nakayama, and C. Chichester, "Studies on the light and dark interconversions of leaf xanthophylls," *Archives of Biochemistry and Biophysics*, vol. 97, no. 1, pp. 168 – 173, 1962.

[16] P. Jahns, D. Latowski, and K. Strzalka, "Mechanism and regulation of the violaxanthin cycle: The role of antenna proteins and membrane lipids," *Biochimica et Biophysica Acta - Bioenergetics*, vol. 1787, no. 1, pp. 3–14, 2009.

[17] X.-P. Li, O. Björkman, C. Shih, A. R. Grossman, M. Rosenquist, S. Jansson, and K. K. Niyogi, "A pigment-binding protein essential for regulation of photosynthetic light harvesting," *Nature*, vol. 403, no. 6768, pp. 391–395, 2000.

[18] A. V. Ruban, M. P. Johnson, and C. D. Duffy, "The photoprotective molecular switch in the photosystem II antenna," *Biochimica et Biophysica Acta (BBA)-Bioenergetics*, vol. 1817, no. 1, pp. 167–181, 2012.

[19] G. Peers, T. B. Truong, E. Ostendorf, A. Busch, D. Elrad, A. R. Grossman, M. Hippler, and K. K. Niyogi, "An ancient light-harvesting protein is critical for the regulation of algal photosynthesis," *Nature*, vol. 462, no. 7272, pp. 518–521, 2009.

[20] G. Bonente, M. Ballottari, T. B. Truong, T. Morosinotto, T. K. Ahn, G. R. Fleming, K. K. Niyogi, and R. Bassi, "Analysis of LhcSR3, a Protein Essential for Feedback De-Excitation in the Green Alga *Chlamydomonas reinhardtii*," *PLoS Biol*, vol. 9, p. e1000577, 01 2011.

[21] J. P. Connelly, M. G. Müller, R. Bassi, R. Croce, and A. R. Holzwarth, "Femtosecond transient absorption study of carotenoid to chlorophyll energy transfer in the light-harvesting complex II of photosystem II," *Biochemistry*, vol. 36, no. 2, pp. 281–287, 1997.

[22] R. Croce, M. G. Müller, R. Bassi, and A. R. Holzwarth, "Carotenoid-to-chlorophyll energy transfer in recombinant major light-harvesting complex (LHCII) of higher plants. I. Femtosecond transient absorption measurements," *Biophysical journal*, vol. 80, no. 2, pp. 901–915, 2001.

[23] N. E. Holt, J. Kennis, L. DallOsto, R. Bassi, and G. R. Fleming, "Carotenoid to chlorophyll energy transfer in light harvesting complex II from *Arabidopsis thaliana* probed by femtosecond fluorescence upconversion," *Chemical Physics Letters*, vol. 379, no. 34, pp. 305 – 313, 2003.

[24] C. C. Gradinaru, J. T. Kennis, E. Papagiannakis, I. H. van Stokkum, R. J. Cogdell, G. R. Fleming, R. A. Niederman, and R. van Grondelle, "An unusual pathway of excitation energy deactivation in carotenoids: singlet-to-triplet conversion on an ultrafast timescale in a photosynthetic antenna," *Proceedings of the National Academy of Sciences*, vol. 98, no. 5, pp. 2364–2369, 2001.

[25] E. Papagiannakis, J. T. Kennis, I. H. van Stokkum, R. J. Cogdell, and R. van Grondelle, "An alternative carotenoid-to-bacteriochlorophyll energy transfer pathway in photosynthetic light harvesting," *Proceedings of the National Academy of Sciences*, vol. 99, no. 9, pp. 6017–6022, 2002.

[26] R. J. Cogdell and H. A. Frank, "How carotenoids function in photosynthetic bacteria," *Biochimica et Biophysica Acta (BBA)-Reviews on Bioenergetics*, vol. 895, no. 2, pp. 63–79, 1987.

[27] N. E. Holt, D. Zigmantas, L. Valkunas, X.-P. Li, K. K. Niyogi, and G. R. Fleming, "Carotenoid cation formation and the regulation of photosynthetic light harvesting," *Science*, vol. 307, no. 5708, pp. 433–436, 2005.

[28] T. K. Ahn, T. J. Avenson, M. Ballottari, Y.-C. Cheng, K. K. Niyogi, R. Bassi, and G. R. Fleming, "Architecture of a charge-transfer state regulating light harvesting in a plant antenna protein," *Science*, vol. 320, no. 5877, pp. 794–797, 2008.

[29] T. J. Avenson, T. K. Ahn, D. Zigmantas, K. K. Niyogi, Z. Li, M. Ballottari, R. Bassi, and G. R. Fleming, "Zeaxanthin radical cation formation in minor light-harvesting complexes of higher plant antenna," *Journal of biological chemistry*, vol. 283, no. 6, pp. 3550–3558, 2008.

[30] H. A. Frank, A. Cua, V. Chynwat, A. Young, D. Gosztola, and M. R. Wasielewski, "Photophysics of the carotenoids associated with the xanthophyll cycle in photosynthesis," *Photosynthesis Research*, vol. 41, no. 3, pp. 389–395, 1994.

[31] A. V. Ruban, R. Berera, C. Ilioaia, I. H. Van Stokkum, J. T. Kennis, A. A. Pascal, H. Van Amerongen, B. Robert, P. Horton, and R. Van Grondelle, "Identification of a mechanism of photoprotective energy dissipation in higher plants," *Nature*, vol. 450, no. 7169, pp. 575–578, 2007.

[32] H. van Amerongen and R. van Grondelle, "Understanding the energy transfer function of lhcii, the major light-harvesting complex of green plants," *The Journal of Physical Chemistry B*, vol. 105, no. 3, pp. 604–617, 2001.

[33] S. Bode, C. C. Quentmeier, P.-N. Liao, N. Hafi, T. Barros, L. Wilk, F. Bittner, and P. J. Walla, "On the regulation of photosynthesis by excitonic interactions between carotenoids and chlorophylls," *Proceedings of the National Academy of Sciences*, vol. 106, no. 30, pp. 12311–12316, 2009.

[34] P.-N. Liao, C.-P. Holleboom, L. Wilk, W. Khlbrandt, and P. J. Walla, "Correlation of Car $S_1 \rightarrow$ Chl with Chl $\rightarrow$ Car S_1 energy transfer supports the excitonic model in quenched light harvesting complex II," *The Journal of Physical Chemistry B*, vol. 114, no. 47, pp. 15650–15655, 2010.

[35] P.-N. Liao, S. Bode, L. Wilk, N. Hafi, and P. J. Walla, "Correlation of electronic carotenoid–chlorophyll interactions and fluorescence quenching with the aggregation of native LHC II and chlorophyll deficient mutants," *Chemical Physics*, vol. 373, no. 1, pp. 50–55, 2010.

[36] C.-P. Holleboom and P. J. Walla, "The back and forth of energy transfer between carotenoids and chlorophylls and its role in the regulation of light harvesting," *Photosynthesis research*, vol. 119, no. 1-2, pp. 215–221, 2014.

[37] Y. Miloslavina, A. Wehner, P. H. Lambrev, E. Wientjes, M. Reus, G. Garab, R. Croce, and A. R. Holzwarth, "Far-red fluorescence: a direct spectroscopic marker for LHCII oligomer formation in non-photochemical quenching," *FEBS letters*, vol. 582, no. 25, pp. 3625–3631, 2008.

[38] M. G. Müller, P. Lambrev, M. Reus, E. Wientjes, R. Croce, and A. R. Holzwarth, "Singlet Energy Dissipation in the Photosystem II Light-Harvesting Complex Does Not Involve Energy Transfer to Carotenoids," *ChemPhysChem*, vol. 11, no. 6, pp. 1289–1296, 2010.

[39] J. P. Ide, D. R. Klug, W. Khlbrandt, L. B. Giorgi, and G. Porter, "The state of detergent solubilised light-harvesting chlorophyll-a/b protein complex as monitored by picosecond time-resolved fluorescence and circular dichroism," *Biochimica et Biophysica Acta (BBA) - Bioenergetics*, vol. 893, no. 2, pp. 349 – 364, 1987.

[40] Y.-Z. Ma, N. E. Holt, X.-P. Li, K. K. Niyogi, and G. R. Fleming, "Evidence for direct carotenoid involvement in the regulation of photosynthetic light harvesting," *Proceedings of the National Academy of Sciences*, vol. 100, no. 8, pp. 4377–4382, 2003.

[41] A. Dreuw, G. R. Fleming, and M. Head-Gordon, "Chlorophyll fluorescence quenching by xanthophylls," *Physical Chemistry Chemical Physics*, vol. 5, no. 15, pp. 3247–3256, 2003.

[42] A. Dreuw, G. R. Fleming, and M. Head-Gordon, "Charge-transfer state as a possible signature of a zeaxanthin-chlorophyll dimer in the non-photochemical quenching process in green plants," *The Journal of Physical Chemistry B*, vol. 107, no. 27, pp. 6500–6503, 2003.

[43] M. P. Johnson and A. V. Ruban, "Photoprotective energy dissipation in higher plants involves alteration of the excited state energy of the emitting chlorophyll (s) in the light harvesting antenna II (LHCII)," *Journal of biological chemistry*, vol. 284, no. 35, pp. 23592–23601, 2009.

[44] N. E. Geacintov, J. Breton, and R. S. Knox, "Energy migration and exciton trapping in green plant photosynthesis," *Photosynthesis research*, vol. 10, no. 3, pp. 233–242, 1986.

[45] T. Brixner, T. Mancal, I. V. Stiopkin, and G. R. Fleming, "Phase-stabilized two-dimensional electronic spectroscopy," *The Journal of Chemical Physics*, vol. 121, no. 9, pp. 4221–4236, 2004.

[46] J. D. Hybl, A. W. Albrecht, S. M. G. Faeder, and D. M. Jonas, "Two-dimensional electronic spectroscopy," *Chemical Physics Letters*, vol. 297, no. 34, pp. 307 – 313, 1998.

[47] K. Gundogdu, K. W. Stone, D. B. Turner, and K. A. Nelson, "Multidimensional coherent spectroscopy made easy," *Chemical Physics*, vol. 341, no. 13, pp. 89 – 94, 2007.

[48] J. A. Myers, K. L. Lewis, P. F. Tekavec, and J. P. Ogilvie, "Two-color two-dimensional fourier transform electronic spectroscopy with a pulse-shaper," *Opt. Express*, vol. 16, pp. 17420–17428, Oct 2008.

[49] G. S. Schlau-Cohen, A. Ishizaki, and G. R. Fleming, "Two-dimensional electronic spectroscopy and photosynthesis: Fundamentals and applications to photosynthetic light-harvesting," *Chemical Physics*, vol. 386, no. 1, pp. 1–22, 2011.

[50] N. S. Ginsberg, Y.-C. Cheng, and G. R. Fleming, "Two-dimensional electronic spectroscopy of molecular aggregates," *Accounts of chemical research*, vol. 42, no. 9, pp. 1352–1363, 2009.

[51] R. Berera, R. van Grondelle, and J. Kennis, "Ultrafast transient absorption spectroscopy: principles and application to photosynthetic systems," *Photosynthesis Research*, vol. 101, no. 2-3, pp. 105–118, 2009.

[52] C. Rullière, *Femtosecond laser pulses*. Springer, 2005.

[53] J. R. Lakowicz, *Principles of fluorescence spectroscopy*. Springer, 2009.

[54] W. Sidler, *Phycobilisome and Phycobiliprotein Structures*, vol. 1 of *Advances in Photosynthesis and Respiration*. Springer Netherlands, 2004.

[55] A. R. Grossman, M. R. Schaefer, G. G. Chiang, and J. L. Collier, "The phycobilisome, a light-harvesting complex responsive to environmental conditions.," *Microbiological reviews*, vol. 57, no. 3, pp. 725–749, 1993.

[56] H. Liu, H. Zhang, D. M. Niedzwiedzki, M. Prado, G. He, M. L. Gross, and R. E. Blankenship, "Phycobilisomes supply excitations to both photosystems in a megacomplex in cyanobacteria," *Science*, vol. 342, no. 6162, pp. 1104–1107, 2013.

[57] K. E. Bissati, E. Delphin, N. Murata, A.-L. Etienne, and D. Kirilovsky, "Photosystem II fluorescence quenching in the cyanobacterium *Synechocystis* PCC 6803: involvement of two different mechanisms," *Biochimica et Biophysica Acta (BBA) - Bioenergetics*, vol. 1457, no. 3, pp. 229 – 242, 2000.

[58] M. G. Rakhimberdieva, I. N. Stadnichuk, I. V. Elanskaya, and N. V. Karapetyan, "Carotenoid-induced quenching of the phycobilisome fluorescence in photosystem II-deficient mutant of *Synechocystis sp.*," *FEBS letters*, vol. 574, no. 1, pp. 85–88, 2004.

[59] A. Wilson, G. Ajlani, J.-M. Verbavatz, I. Vass, C. A. Kerfeld, and D. Kirilovsky, "A soluble carotenoid protein involved in phycobilisome-related energy dissipation in cyanobacteria," *The Plant Cell Online*, vol. 18, no. 4, pp. 992–1007, 2006.

[60] D. Kirilovsky, "Photoprotection in cyanobacteria: the orange carotenoid protein (OCP)-related non-photochemical-quenching mechanism," *Photosynthesis Research*, vol. 93, no. 1-3, pp. 7–16, 2007.

[61] S. Bailey and A. Grossman, "Photoprotection in cyanobacteria: Regulation of light harvesting," *Photochemistry and Photobiology*, vol. 84, no. 6, pp. 1410–1420, 2008.

[62] D. Kirilovsky and C. A. Kerfeld, "The orange carotenoid protein in photoprotection of photosystem II in cyanobacteria," *Biochimica et Biophysica Acta (BBA)-Bioenergetics*, vol. 1817, no. 1, pp. 158–166, 2012.

[63] Y. Zhu, J. E. Graham, M. Ludwig, W. Xiong, R. M. Alvey, G. Shen, and D. A. Bryant, "Roles of xanthophyll carotenoids in protection against photoinhibition and oxidative stress in the cyanobacterium *Synechococcus sp.* strain PCC 7002," *Archives of biochemistry and biophysics*, vol. 504, no. 1, pp. 86–99, 2010.

[64] N. Yeremenko, R. Kouril, J. A. Ihalainen, S. D'Haene, N. van Oosterwijk, E. G. Andrizhiyevskaya, W. Keegstra, H. L. Dekker, M. Hagemann, E. J. Boekema, *et al.*, "Supramolecular organization and dual function of the isia chlorophyll-binding protein in cyanobacteria," *Biochemistry*, vol. 43, no. 32, pp. 10308–10313, 2004.

[65] J. A. Ihalainen, S. D'Haene, N. Yeremenko, H. van Roon, A. A. Arteni, E. J. Boekema, R. van Grondelle, H. C. Matthijs, and J. P. Dekker, "Aggregates of the chlorophyll-binding protein IsiA (CP43′) dissipate energy in cyanobacteria," *Biochemistry*, vol. 44, no. 32, pp. 10846–10853, 2005.

[66] C. Funk and W. Vermaas, "A cyanobacterial gene family coding for single-helix proteins resembling part of the light-harvesting proteins from higher plants," *Biochemistry*, vol. 38, no. 29, pp. 9397–9404, 1999.

[67] Q. He, N. Dolganov, O. Björkman, and A. R. Grossman, "The high light-inducible polypeptides in *Synechocystis* PCC6803 expression and function in high light," *Journal of Biological Chemistry*, vol. 276, no. 1, pp. 306–314, 2001.

[68] M. Gwizdala, A. Wilson, and D. Kirilovsky, "In Vitro Reconstitution of the Cyanobacterial Photoprotective Mechanism Mediated by the Orange Carotenoid Protein in *Synechocystis* PCC 6803," *The Plant Cell Online*, vol. 23, no. 7, pp. 2631–2643, 2011.

[69] A. Wilson, C. Punginelli, A. Gall, C. Bonetti, M. Alexandre, J.-M. Routaboul, C. A. Kerfeld, R. van Grondelle, B. Robert, J. T. M. Kennis, and D. Kirilovsky, "A photoactive carotenoid protein acting as light intensity sensor," *Proceedings of the National Academy of Sciences*, vol. 105, no. 33, pp. 12075–12080, 2008.

[70] M. Y. Gorbunov, F. I. Kuzminov, V. V. Fadeev, J. D. Kim, and P. G. Falkowski, "A kinetic model of non-photochemical quenching in cyanobacteria," *Biochimica et Biophysica Acta (BBA) - Bioenergetics*, vol. 1807, no. 12, pp. 1591 – 1599, 2011.

[71] A. Wilson, M. Gwizdala, A. Mezzetti, M. Alexandre, C. A. Kerfeld, and D. Kirilovsky, "The Essential Role of the N-Terminal Domain of the Orange Carotenoid Protein in Cyanobacterial Photoprotection: Importance of a Positive Charge for Phycobilisome Binding," *The Plant Cell Online*, vol. 24, no. 5, pp. 1972–1983, 2012.

[72] C. Boulay, L. Abasova, C. Six, I. Vass, and D. Kirilovsky, "Occurrence and function of the orange carotenoid protein in photoprotective mechanisms in various cyanobacteria," *Biochimica et Biophysica Acta (BBA) - Bioenergetics*, vol. 1777, no. 10, pp. 1344 – 1354, 2008.

[73] C. Boulay, A. Wilson, S. D'Haene, and D. Kirilovsky, "Identification of a protein required for recovery of full antenna capacity in OCP-related photoprotective mechanism in cyanobacteria," *Proceedings of the National Academy of Sciences*, vol. 107, no. 25, pp. 11620–11625, 2010.

[74] M. Sutter, A. Wilson, R. L. Leverenz, R. Lopez-Igual, A. Thurotte, A. E. Salmeen, D. Kirilovsky, and C. A. Kerfeld, "Crystal structure of the FRP and identification of the active site for modulation of OCP-mediated photoprotection in cyanobacteria," *Proceedings of the National Academy of Sciences*, vol. 110, no. 24, pp. 10022–10027, 2013.

[75] C. A. Kerfeld and D. Kirilovsky, "Chapter One - Structural, Mechanistic and Genomic Insights into OCP-Mediated Photoprotection," in *Genomics of Cyanobacteria* (F. Chauvat and C. Cassier-Chauvat, eds.), vol. 65 of *Advances in Botanical Research*, pp. 1 – 26, Academic Press, 2013.

[76] K. K. Niyogi, O. Björkman, and A. R. Grossman, "The roles of specific xanthophylls in photoprotection," *Proc. Natl. Acad. Sci. U.S.A.*, vol. 94, no. 25, pp. 14162–14167, 1997.

[77] Z. Li, T. K. Ahn, T. J. Avenson, M. Ballottari, J. A. Cruz, D. M. Kramer, R. Bassi, G. R. Fleming, J. D. Keasling, and K. K. Niyogi, "Lutein accumulation in the absence of zeaxanthin restores nonphotochemical quenching in the Arabidopsis thaliana *npq1* mutant," *The Plant Cell Online*, vol. 21, no. 6, pp. 1798–1812, 2009.

[78] A. V. Ruban, A. A. Pascal, B. Robert, and P. Horton, "Activation of zeaxanthin is an obligatory event in the regulation of photosynthetic light harvesting," *J. Biol. Chem.*, vol. 277, no. 10, pp. 7785–7789, 2002.

[79] C. A. Kerfeld, M. R. Sawaya, V. Brahmandam, D. Cascio, K. K. Ho, C. C. Trevithick-Sutton, D. W. Krogmann, and T. O. Yeates, "The crystal structure of a cyanobacterial water-soluble carotenoid binding protein," *Structure*, vol. 11, no. 1, pp. 55 – 65, 2003.

[80] H. Zhang, H. Liu, D. M. Niedzwiedzki, M. Prado, J. Jiang, M. L. Gross, and R. E. Blankenship, "Molecular mechanism of photoactivation and structural location of the cyanobacterial orange carotenoid protein," *Biochemistry*, vol. 53, no. 1, pp. 13–19, 2014.

[81] A. Wilson, J. N. Kinney, P. H. Zwart, C. Punginelli, S. D'Haene, F. Perreau, M. G. Klein, D. Kirilovsky, and C. A. Kerfeld, "Structural determinants underlying photoprotection in the photoactive orange carotenoid protein of cyanobacteria," *J. Biol. Chem.*, vol. 285, no. 24, pp. 18364–18375, 2010.

[82] R. Berera, M. Gwizdala, I. H. M. van Stokkum, D. Kirilovsky, and R. van Grondelle, "Excited states of the inactive and active forms of the orange carotenoid protein," *J. Phys. Chem. B*, vol. 117, no. 31, pp. 9121–9128, 2013.

[83] R. L. Leverenz, D. Jallet, M.-D. Li, R. A. Mathies, D. Kirilovsky, and C. A. Kerfeld, "Structural and Functional Modularity of the Orange Carotenoid Protein: Distinct Roles for the N- and C-Terminal Domains in Cyanobacterial Photoprotection," *The Plant Cell Online*, 2014.

[84] C. Punginelli, A. Wilson, J.-M. Routaboul, and D. Kirilovsky, "Influence of zeaxanthin and echinenone binding on the activity of the orange carotenoid protein," *Biochim. Biophys. Acta*, vol. 1787, no. 4, pp. 280 – 288, 2009.

[85] L. Tian, I. H. M. van Stokkum, R. B. M. Koehorst, A. Jongerius, D. Kirilovsky, and H. van Amerongen, "Site, rate, and mechanism of photoprotective quenching in cyanobacteria," *J. Am. Chem. Soc.*, vol. 133, no. 45, pp. 18304–18311, 2011.

[86] R. Berera, I. H. M. van Stokkum, M. Gwizdala, A. Wilson, D. Kirilovsky, and R. van Grondelle, "The photophysics of the orange carotenoid protein, a light-powered molecular switch," *J. Phys. Chem. B*, vol. 116, no. 8, pp. 2568–2574, 2012.

[87] T. Polívka, P. Chábera, and C. A. Kerfeld, "Carotenoid-protein interaction alters the s_1 energy of hydroxyechinenone in the orange carotenoid protein," *Biochim. Biophys. Acta*, vol. 1827, no. 3, pp. 248 – 254, 2013.

[88] K. L. M. Lewis and J. P. Ogilvie, "Probing photosynthetic energy and charge transfer with two-dimensional electronic spectroscopy," *J. Phys. Chem. Lett.*, vol. 3, no. 4, pp. 503–510, 2012.

[89] G. S. Schlau-Cohen, J. M. Dawlaty, and G. R. Fleming, "Ultrafast multidimensional spectroscopy: principles and applications to photosynthetic systems," *Selected Topics in Quantum Electronics, IEEE Journal of*, vol. 18, no. 1, pp. 283–295, 2012.

[90] E. L. Read, G. S. Schlau-Cohen, G. S. Engel, T. Georgiou, M. Z. Papiz, and G. R. Fleming, "Pigment organization and energy level structure in light-harvesting complex 4: Insights from two-dimensional electronic spectroscopy," *J. Phys. Chem. B*, vol. 113, no. 18, pp. 6495–6504, 2009.

[91] G. S. Schlau-Cohen, T. R. Calhoun, N. S. Ginsberg, E. L. Read, M. Ballottari, R. Bassi, R. van Grondelle, and G. R. Fleming, "Pathways of energy flow in lhcii from two-dimensional electronic spectroscopy," *J. Phys. Chem. B*, vol. 113, no. 46, pp. 15352–15363, 2009.

[92] G. S. Schlau-Cohen, T. R. Calhoun, N. S. Ginsberg, M. Ballottari, R. Bassi, and G. R. Fleming, "Spectroscopic elucidation of uncoupled transition energies in the major photosynthetic light-harvesting complex, LHCII," *Proceedings of the National Academy of Sciences*, vol. 107, no. 30, pp. 13276–13281, 2010.

[93] N. S. Ginsberg, J. A. Davis, M. Ballottari, Y.-C. Cheng, R. Bassi, and G. R. Fleming, "Solving structure in the cp29 light harvesting complex with polarization-phased 2d electronic spectroscopy," *Proc. Natl. Acad. Sci. U.S.A.*, vol. 108, no. 10, pp. 3848–3853, 2011.

[94] G. S. Schlau-Cohen, E. De Re, R. J. Cogdell, and G. R. Fleming, "Determination of excited-state energies and dynamics in the b band of the bacterial reaction center with 2d electronic spectroscopy," *J. Phys. Chem. Lett.*, vol. 3, no. 17, pp. 2487–2492, 2012.

[95] T. R. Calhoun, J. A. Davis, M. W. Graham, and G. R. Fleming, "The separation of overlapping transitions in β-carotene with broadband 2D electronic spectroscopy," *Chemical Physics Letters*, vol. 523, pp. 1–5, 2012.

[96] T. K. Holt and D. W. Krogmann, "A carotenoid-protein from cyanobacteria," *Biochim. Biophys. Acta*, vol. 637, no. 3, pp. 408 – 414, 1981.

[97] Y. P. Wu and D. W. Krogmann, "The orange carotenoid protein of *Synechocystis* pcc 6803," *Biochimica et Biophysica Acta (BBA)-Bioenergetics*, vol. 1322, no. 1, pp. 1–7, 1997.

[98] T. Brixner, I. V. Stiopkin, and G. R. Fleming, "Tunable two-dimensional femtosecond spectroscopy," *Opt. Lett.*, vol. 29, pp. 884–886, Apr 2004.

[99] R. Trebino, K. W. DeLong, D. N. Fittinghoff, J. N. Sweetser, M. A. Krumbgel, B. A. Richman, and D. J. Kane, "Measuring ultrashort laser pulses in the time-frequency domain using frequency-resolved optical gating," *Review of Scientific Instruments*, vol. 68, no. 9, pp. 3277–3295, 1997.

[100] J. D. Hybl, A. A. Ferro, and D. M. Jonas, "Two-dimensional fourier transform electronic spectroscopy," *J. Chem. Phys.*, vol. 115, no. 14, pp. 6606–6622, 2001.

[101] T. Polívka, C. A. Kerfeld, T. Pascher, and V. Sundström, "Spectroscopic properties of the carotenoid 3′-hydroxyechinenone in the orange carotenoid protein from the cyanobacterium *Arthrospira maxima*," *Biochemistry*, vol. 44, no. 10, pp. 3994–4003, 2005.

[102] N. Christensson, F. Milota, A. Nemeth, J. Sperling, H. F. Kauffmann, T. Pullerits, and J. Hauer, "Two-dimensional electronic spectroscopy of β-carotene," *J. Phys. Chem. B*, vol. 113, no. 51, pp. 16409–16419, 2009.

[103] M. Garavelli, P. Celani, F. Bernardi, M. A. Robb, and M. Olivucci, "Force fields for ultrafast photochemisrty: The s2 (1bu) $\rightarrow$ s1 (2ag) $\rightarrow$ s0 (1ag) reaction path for all-trans-hexa-1, 3, 5-triene," *J. Am. Chem. Soc.*, vol. 119, no. 47, pp. 11487–11494, 1997.

[104] W. Fuss, Y. Haas, and S. Zilberg, "Twin states and conical intersections in linear polyenes," *Chem. Phys.*, vol. 259, no. 2, pp. 273–295, 2000.

[105] D. W. McCamant, P. Kukura, and R. A. Mathies, "Femtosecond time-resolved stimulated raman spectroscopy: Application to the ultrafast internal conversion in β-carotene," *J. Phys. Chem. A*, vol. 107, no. 40, pp. 8208–8214, 2003.

[106] W. Wohlleben, T. Buckup, H. Hashimoto, R. J. Cogdell, J. L. Herek, and M. Motzkus, "Pump-deplete-probe spectroscopy and the puzzle of carotenoid dark states," *J. Phys. Chem. B*, vol. 108, no. 10, pp. 3320–3325, 2004.

[107] T. Polívka and V. Sundström, "Dark excited states of carotenoids: Consensus and controversy," *Chem. Phys. Lett.*, vol. 477, no. 13, pp. 1 – 11, 2009.

[108] T. Mančal, A. Nemeth, F. Milota, V. Lukeš, H. F. Kauffmann, and J. Sperling, "Vibrational wave packet induced oscillations in two-dimensional electronic spectra. ii. theory," *J. Chem. Phys.*, vol. 132, no. 18, p. 184515, 2010.

[109] P. Chábera, M. Durchan, P. M. Shih, C. A. Kerfeld, and T. Polívka, "Excited-state properties of the 16 kda red carotenoid protein from *Arthrospira maxima*," *Biochim. Biophys. Acta*, vol. 1807, no. 1, pp. 30 – 35, 2011.

[110] S. Shima, R. P. Ilagan, N. Gillespie, B. J. Sommer, R. G. Hiller, F. P. Sharples, H. A. Frank, and R. R. Birge, "Two-photon and fluorescence spectroscopy and the effect of environment on the photochemical properties of peridinin in solution and in the

peridinin-chlorophyll-protein from *Amphidinium carterae*," *J. Phys. Chem. A*, vol. 107, no. 40, pp. 8052–8066, 2003.

[111] M. M. Enriquez, M. Fuciman, A. M. LaFountain, N. L. Wagner, R. R. Birge, and H. A. Frank, "The intramolecular charge transfer state in carbonyl-containing polyenes and carotenoids," *J. Phys. Chem. B*, vol. 114, no. 38, pp. 12416–12426, 2010.

[112] L. Tian, M. Gwizdala, I. van Stokkum, R. Koehorst, D. Kirilovsky, and H. van Amerongen, "Picosecond kinetics of light harvesting and photoprotective quenching in wild-type and mutant phycobilisomes isolated from the cyanobacterium *Synechocystis* pcc 6803," *Biophys. J.*, vol. 102, no. 7, pp. 1692 – 1700, 2012.

[113] P. Horton, A. V. Ruban, and M. Wentworth, "Allosteric regulation of the light-harvesting system of photosystem ii," *Philos. Trans. R. Soc., B*, vol. 355, no. 1402, pp. 1361–1370, 2000.

[114] A. Wilson, C. Punginelli, M. Couturier, F. Perreau, and D. Kirilovsky, "Essential role of two tyrosines and two tryptophans on the photoprotection activity of the orange carotenoid protein," *Biochim. Biophys. Acta*, vol. 1807, no. 3, pp. 293 – 301, 2011.

[115] H. A. Frank, J. A. Bautista, J. Josue, Z. Pendon, R. G. Hiller, F. P. Sharples, D. Gosztola, and M. R. Wasielewski, "Effect of the solvent environment on the spectroscopic properties and dynamics of the lowest excited states of carotenoids," *The Journal of Physical Chemistry B*, vol. 104, no. 18, pp. 4569–4577, 2000.

[116] D. Zigmantas, R. G. Hiller, F. P. Sharples, H. A. Frank, V. Sundström, and T. Polívka, "Effect of a conjugated carbonyl group on the photophysical properties of carotenoids," *Physical Chemistry Chemical Physics*, vol. 6, no. 11, pp. 3009–3016, 2004.

[117] D. Zigmantas, R. G. Hiller, V. Sundström, and T. Polívka, "Carotenoid to chlorophyll energy transfer in the peridinin–chlorophyll-a–protein complex involves an intramolecular charge transfer state," *Proceedings of the National Academy of Sciences*, vol. 99, no. 26, pp. 16760–16765, 2002.

[118] R. Berera, C. Herrero, I. H. van Stokkum, M. Vengris, G. Kodis, R. E. Palacios, H. van Amerongen, R. van Grondelle, D. Gust, T. A. Moore, *et al.*, "A simple artificial light-harvesting dyad as a model for excess energy dissipation in oxygenic photosynthesis," *Proceedings of the National Academy of Sciences*, vol. 103, no. 14, pp. 5343–5348, 2006.

[119] V. Šlouf, P. Chábera, J. D. Olsen, E. C. Martin, P. Qian, C. N. Hunter, and T. Polívka, "Photoprotection in a purple phototrophic bacterium mediated by oxygen-dependent alteration of carotenoid excited-state properties," *Proceedings of the National Academy of Sciences*, vol. 109, no. 22, pp. 8570–8575, 2012.

[120] I. H. van Stokkum, D. S. Larsen, and R. van Grondelle, "Global and target analysis of time-resolved spectra," *Biochimica et Biophysica Acta (BBA)-Bioenergetics*, vol. 1657, no. 2, pp. 82–104, 2004.

[121] E. E. Ostroumov, R. M. Mulvaney, R. J. Cogdell, and G. D. Scholes, "Broadband 2D Electronic Spectroscopy Reveals a Carotenoid Dark State in Purple Bacteria," *Science*, vol. 340, no. 6128, pp. 52–56, 2013.

[122] B. Feniouk, D. Cherepanov, N. Voskoboynikova, A. Mulkidjanian, and W. Junge, "Chromatophore vesicles of *Rhodobacter capsulatus* contain on average one F_0F_1-ATP synthase each," *Biophysical Journal*, vol. 82, no. 3, pp. 1115–1122, 2002.

[123] G. R. Fleming and R. v. Grondelle, "Femtosecond spectroscopy of photosynthetic light-harvesting systems," *Current opinion in structural biology*, vol. 7, no. 5, pp. 738–748, 1997.

[124] J. Deisenhofer, O. Epp, K. Miki, R. Huber, and H. Michel, "X-ray structure analysis of a membrane protein complex: electron density map at 3 Å resolution and a model of the chromophores of the photosynthetic reaction center from *Rhodopseudomonas viridis*," *Journal of molecular biology*, vol. 180, no. 2, pp. 385–398, 1984.

[125] M. Lutz, I. Agalidis, G. Hervo, R. J. Cogdell, and F. Reiss-Husson, "On the state of carotenoids bound to reaction centers of photosynthetic bacteria: A resonance raman study," *Biochimica et Biophysica Acta (BBA) - Bioenergetics*, vol. 503, no. 2, pp. 287 – 303, 1978.

[126] M. H. Vos, J. Breton, and J.-L. Martin, "Electronic energy transfer within the hexamer cofactor system of bacterial reaction centers," *The Journal of Physical Chemistry B*, vol. 101, no. 47, pp. 9820–9832, 1997.

[127] X. J. Jordanides, G. D. Scholes, and G. R. Fleming, "The Mechanism of Energy Transfer in the Bacterial Photosynthetic Reaction Center," *The Journal of Physical Chemistry B*, vol. 105, no. 8, pp. 1652–1669, 2001.

[128] D. M. Jonas, M. J. Lang, Y. Nagasawa, T. Joo, and G. R. Fleming, "Pump-probe polarization anisotropy study of femtosecond energy transfer within the photosynthetic reaction center of *Rhodobacter sphaeroides* R26," *The Journal of Physical Chemistry*, vol. 100, no. 30, pp. 12660–12673, 1996.

[129] M.-L. Groot, J.-Y. Yu, R. Agarwal, J. R. Norris, and G. R. Fleming, "Three-Pulse Photon Echo Measurements on the Accessory Pigments in the Reaction Center of *Rhodobacter sphaeroides*," *The Journal of Physical Chemistry B*, vol. 102, no. 30, pp. 5923–5931, 1998.

[130] W. W. Parson, R. K. Clayton, and R. J. Cogdell, "Excited states of photosynthetic reaction centers at low redox potentials," *Biochimica et Biophysica Acta (BBA) - Bioenergetics*, vol. 387, no. 2, pp. 265 – 278, 1975.

[131] R. J. Cogdell, T. G. Monger, and W. W. Parson, "Carotenoid triplet states in reaction centers from *Rhodopseudomonas sphaeroides* and *Rhodospirillum rubrum*," *Biochimica et Biophysica Acta (BBA) - Bioenergetics*, vol. 408, no. 3, pp. 189 – 199, 1975.

[132] C. A. Wraight and R. K. Clayton, "The absolute quantum efficiency of bacteriochlorophyll photooxidation in reaction centres of *Rhodopseudomonas spheroides*," *Biochimica et Biophysica Acta (BBA)-Bioenergetics*, vol. 333, no. 2, pp. 246–260, 1974.

[133] W. Zinth and J. Wachtveitl, "The first picoseconds in bacterial photosynthesis: ultrafast electron transfer for the efficient conversion of light energy," *ChemPhysChem*, vol. 6, no. 5, pp. 871–880, 2005.

[134] R. J. Cogdell, A. Gall, and J. Köhler, "The architecture and function of the light-harvesting apparatus of purple bacteria: from single molecules to in vivo membranes," *Quarterly reviews of biophysics*, vol. 39, no. 03, pp. 227–324, 2006.

[135] H. Van Amerongen, L. Valkunas, and R. Van Grondelle, *Photosynthetic excitons*. World Scientific, 2000.

[136] G. R. Fleming, G. S. Schlau-Cohen, K. Amarnath, and J. Zaks, "Design principles of photosynthetic light-harvesting," *Faraday discussions*, vol. 155, pp. 27–41, 2012.

[137] Z. Liu, H. Yan, K. Wang, T. Kuang, J. Zhang, L. Gui, X. An, and W. Chang, "Crystal structure of spinach major light-harvesting complex at 2.72 Å resolution," *Nature*, vol. 428, no. 6980, pp. 287–292, 2004.

[138] G. McDermott, S. Prince, A. Freer, A. Hawthornthwaite-Lawless, M. Papiz, R. Cogdell, and N. Isaacs, "Crystal structure of an integral membrane light-harvesting complex from photosynthetic bacteria," *Nature*, vol. 374, no. 6522, pp. 517–521, 1995.

[139] U. Ermler, G. Fritzsch, S. K. Buchanan, and H. Michel, "Structure of the photosynthetic reaction centre from *Rhodobacter sphaeroides* at 2.65 å resolution: cofactors and protein-cofactor interactions," *Structure*, vol. 2, no. 10, pp. 925–936, 1994.

[140] A. W. Roszak, K. McKendrick, A. T. Gardiner, I. A. Mitchell, N. W. Isaacs, R. J. Cogdell, H. Hashimoto, and H. A. Frank, "Protein regulation of carotenoid binding: gatekeeper and locking amino acid residues in reaction centers of *Rhodobacter sphaeroides*," *Structure*, vol. 12, no. 5, pp. 765–773, 2004.

[141] H. Lee, Y.-C. Cheng, and G. R. Fleming, "Coherence dynamics in photosynthesis: protein protection of excitonic coherence," *Science*, vol. 316, no. 5830, pp. 1462–1465, 2007.

[142] D. Y. Parkinson, H. Lee, and G. R. Fleming, "Measuring electronic coupling in the reaction center of purple photosynthetic bacteria by two-color, three-pulse photon echo peak shift spectroscopy," *The Journal of Physical Chemistry B*, vol. 111, no. 25, pp. 7449–7456, 2007.

[143] C. Kirmaier, D. Holten, and W. W. Parson, "Temperature and detection-wavelength dependence of the picosecond electron-transfer kinetics measured in *Rhodopseudomonas sphaeroides* reaction centers. resolution of new spectral and kinetic components in the primary charge-separation process," *Biochimica et Biophysica Acta (BBA)-Bioenergetics*, vol. 810, no. 1, pp. 33–48, 1985.

[144] C. Kirmaier, D. Holten, and W. W. Parson, "Picosecond-photodichroism studies of the transient states in *Rhodopseudomonas sphaeroides* reaction centers at 5 K. Effects of electron transfer on the six bacteriochlorin pigments," *Biochimica et Biophysica Acta (BBA)-Bioenergetics*, vol. 810, no. 1, pp. 49–61, 1985.

[145] B. A. Heller, D. Holten, and C. Kirmaier, "Control of electron transfer between the L- and M-sides of photosynthetic reaction centers," *Science*, vol. 269, no. 5226, pp. 940–945, 1995.

[146] J. I. Chuang, S. G. Boxer, D. Holten, and C. Kirmaier, "High yield of M-side electron transfer in mutants of *Rhodobacter capsulatus* reaction centers lacking the L-side bacteriopheophytin," *Biochemistry*, vol. 45, no. 12, pp. 3845–3851, 2006.

[147] M. Wakeham and M. Jones, "Rewiring photosynthesis: engineering wrong-way electron transfer in the purple bacterial reaction centre," *Biochemical Society Transactions*, vol. 33, no. 4, pp. 851–857, 2005.

[148] R. J. Stanley, B. King, and S. G. Boxer, "Excited state energy transfer pathways in photosynthetic reaction centers. 1. Structural symmetry effects," *The Journal of Physical Chemistry*, vol. 100, no. 29, pp. 12052–12059, 1996.

[149] J. A. Jackson, S. Lin, A. K. Taguchi, J. C. Williams, J. P. Allen, and N. W. Woodbury, "Energy transfer in *Rhodobacter sphaeroides* reaction centers with the initial electron donor oxidized or missing," *The Journal of Physical Chemistry B*, vol. 101, no. 29, pp. 5747–5754, 1997.

[150] D. M. Jonas, "Two-dimensional femtosecond spectroscopy," *Annual review of physical chemistry*, vol. 54, no. 1, pp. 425–463, 2003.

[151] E. L. Read, G. S. Schlau-Cohen, G. S. Engel, J. Wen, R. E. Blankenship, and G. R. Fleming, "Visualization of excitonic structure in the Fenna-Matthews-Olson photosynthetic complex by polarization-dependent two-dimensional electronic spectroscopy," *Biophysical journal*, vol. 95, no. 2, pp. 847–856, 2008.

[152] D. C. Arnett, C. Moser, P. Dutton, and N. Scherer, "The first events in photosynthesis: electronic coupling and energy transfer dynamics in the photosynthetic reaction center from rhodobacter sphaeroides," *The Journal of Physical Chemistry B*, vol. 103, no. 11, pp. 2014–2032, 1999.

[153] J. Pan, S. Lin, and N. W. Woodbury, "Bacteriochlorophyll excited-state quenching pathways in bacterial reaction centers with the primary donor oxidized," *The Journal of Physical Chemistry B*, vol. 116, no. 6, pp. 2014–2022, 2012.

[154] L. Huang, N. Ponomarenko, G. P. Wiederrecht, and D. M. Tiede, "Cofactor-specific photochemical function resolved by ultrafast spectroscopy in photosynthetic reaction center crystals," *Proceedings of the National Academy of Sciences*, vol. 109, no. 13, pp. 4851–4856, 2012.

[155] R. M. Hochstrasser, "Two-dimensional IR-spectroscopy: polarization anisotropy effects," *Chemical Physics*, vol. 266, no. 2, pp. 273–284, 2001.

[156] L. D. Barron, *Molecular light scattering and optical activity*. Cambridge University Press, 2004.

[157] J. Dreyer, A. M. Moran, and S. Mukamel, "Tensor components in three pulse vibrational echoes of a rigid dipeptide," *BULLETIN-KOREAN CHEMICAL SOCIETY*, vol. 24, no. 8, pp. 1091–1096, 2003.

[158] E. L. Read, G. S. Engel, T. R. Calhoun, T. Mančal, T. K. Ahn, R. E. Blankenship, and G. R. Fleming, "Cross-peak-specific two-dimensional electronic spectroscopy," *Proceedings of the National Academy of Sciences*, vol. 104, no. 36, pp. 14203–14208, 2007.

[159] X. J. Jordanides, G. D. Scholes, W. A. Shapley, J. R. Reimers, and G. R. Fleming, "Electronic couplings and energy transfer dynamics in the oxidized primary electron donor of the bacterial reaction center," *The Journal of Physical Chemistry B*, vol. 108, no. 5, pp. 1753–1765, 2004.

[160] T. Brixner, J. Stenger, H. M. Vaswani, M. Cho, R. E. Blankenship, and G. R. Fleming, "Two-dimensional spectroscopy of electronic couplings in photosynthesis," *Nature*, vol. 434, no. 7033, pp. 625–628, 2005.

[161] A. Ishizaki, T. R. Calhoun, G. S. Schlau-Cohen, and G. R. Fleming, "Quantum coherence and its interplay with protein environments in photosynthetic electronic energy transfer," *Physical Chemistry Chemical Physics*, vol. 12, no. 27, pp. 7319–7337, 2010.

[162] A. Ishizaki and G. R. Fleming, "Unified treatment of quantum coherent and incoherent hopping dynamics in electronic energy transfer: Reduced hierarchy equation approach," *The Journal of chemical physics*, vol. 130, no. 23, p. 234111, 2009.

[163] V. May, "Higher-order processes of excitation energy transfer in supramolecular complexes: Liouville space analysis of bridge molecule mediated transfer and direct photon exchange," *The Journal of chemical physics*, vol. 129, no. 11, p. 114109, 2008.

[164] B. Albinsson and J. Mårtensson, "Excitation energy transfer in donor–bridge–acceptor systems," *Physical Chemistry Chemical Physics*, vol. 12, no. 27, pp. 7338–7351, 2010.

[165] G. D. Scholes, "Long-range resonance energy transfer in molecular systems," *Annual review of physical chemistry*, vol. 54, no. 1, pp. 57–87, 2003.

[166] A. deWinter and S. G. Boxer, "The mechanism of triplet energy transfer from the special pair to the carotenoid in bacterial photosynthetic reaction centers," *The Journal of Physical Chemistry B*, vol. 103, no. 41, pp. 8786–8789, 1999.

[167] K. Timpmann, A. Freiberg, and V. Sundström, "Energy trapping and detrapping in the photosynthetic bacterium *Rhodopseudomonas viridis*: transfer-to-trap-limited dynamics," *Chemical physics*, vol. 194, no. 2, pp. 275–283, 1995.

[168] K. Bernhardt and H.-W. Trissl, "Escape probability and trapping mechanism in purple bacteria: revisited," *Biochimica et Biophysica Acta (BBA)-Bioenergetics*, vol. 1457, no. 1, pp. 1–17, 2000.

[169] J. Amesz and S. Neerken, "Excitation energy trapping in anoxygenic photosynthetic bacteria," *Photosynthesis research*, vol. 73, no. 1-3, pp. 73–81, 2002.

[170] M. K. Şener, J. D. Olsen, C. N. Hunter, and K. Schulten, "Atomic-level structural and functional model of a bacterial photosynthetic membrane vesicle," *Proceedings of the National Academy of Sciences*, vol. 104, no. 40, pp. 15723–15728, 2007.

[171] L. Lepetit and M. Joffre, "Two-dimensional nonlinear optics using fourier-transform spectral interferometry," *Optics letters*, vol. 21, no. 8, pp. 564–566, 1996.

[172] R. R. Ernst, G. Bodenhausen, A. Wokaun, *et al.*, *Principles of nuclear magnetic resonance in one and two dimensions*, vol. 14. Clarendon press Oxford, 1987.

[173] J. A. Myers, K. L. Lewis, P. F. Tekavec, and J. P. Ogilvie, "Two-color two-dimensional fourier transform electronic spectroscopy with a pulse-shaper," *Opt. Express*, vol. 16, pp. 17420–17428, Oct 2008.

[174] P. F. Tekavec, J. A. Myers, K. L. M. Lewis, and J. P. Ogilvie, "Two-dimensional electronic spectroscopy with a continuum probe," *Opt. Lett.*, vol. 34, pp. 1390–1392, May 2009.

[175] M. Kullmann, S. Ruetzel, J. Buback, P. Nuernberger, and T. Brixner, "Reaction dynamics of a molecular switch unveiled by coherent two-dimensional electronic spectroscopy," *Journal of the American Chemical Society*, vol. 133, no. 33, pp. 13074–13080, 2011.

[176] E. Harel and G. S. Engel, "Quantum coherence spectroscopy reveals complex dynamics in bacterial light-harvesting complex 2 (LH2)," *Proceedings of the National Academy of Sciences*, vol. 109, no. 3, pp. 706–711, 2012.

[177] H. Zheng, J. R. Caram, P. D. Dahlberg, B. S. Rolczynski, S. Viswanathan, D. S. Dolzhnikov, A. Khadivi, D. V. Talapin, and G. S. Engel, "Dispersion-free continuum two-dimensional electronic spectrometer," *Appl. Opt.*, vol. 53, pp. 1909–1917, Mar 2014.

[178] R. J. Cogdell, W. W. Parson, and M. A. Kerr, "The type, amount, location, and energy transfer properties of the carotenoid in reaction centers from rhodopseudomonas sphaeroides," *Biochimica et Biophysica Acta (BBA) - Bioenergetics*, vol. 430, no. 1, pp. 83 – 93, 1976.

[179] S. Lin, E. Katilius, A. K. W. Taguchi, and N. W. Woodbury, "Excitation energy transfer from carotenoid to bacteriochlorophyll in the photosynthetic purple bacterial reaction center of rhodobacter sphaeroides," *The Journal of Physical Chemistry B*, vol. 107, no. 50, pp. 14103–14108, 2003.

[180] Y. Jia, D. M. Jonas, T. Joo, Y. Nagasawa, M. J. Lang, and G. R. Fleming, "Observation of ultrafast energy transfer from the accessory bacteriochlorophylls to the special pair in photosynthetic reaction centers," *The Journal of Physical Chemistry*, vol. 99, no. 17, pp. 6263–6266, 1995.

[181] J. C. Vaughan, T. Hornung, T. Feurer, and K. A. Nelson, "Diffraction-based femtosecond pulse shaping with a two-dimensional spatial light modulator," *Opt. Lett.*, vol. 30, pp. 323–325, Feb 2005.

[182] J. S. Leigh Jr and P. L. Dutton, "Reaction center bacteriochlorophyll triplet states: redox potential dependence and kinetics," *Biochimica et Biophysica Acta (BBA)-Bioenergetics*, vol. 357, no. 1, pp. 67–77, 1974.

[183] P. Parot, J. Thiery, and A. Verméglio, "Charge recombination at low temperature in photosynthetic bacteria reaction centers: Evidence for two conformation states," *Biochimica et Biophysica Acta (BBA)-Bioenergetics*, vol. 893, no. 3, pp. 534–543, 1987.

[184] C. Gerotto, A. Alboresi, G. M. Giacometti, R. Bassi, and T. Morosinotto, "Coexistence of plant and algal energy dissipation mechanisms in the moss *Physcomitrella patens*," *New Phytologist*, vol. 196, no. 3, pp. 763–773, 2012.

[185] E. Giuffra, D. Cugini, R. Croce, and R. Bassi, "Reconstitution and Pigment-Binding Properties of Recombinant CP29," *European journal of biochemistry*, vol. 238, no. 1, pp. 112–120, 1996.

[186] M. Crimi, D. Dorra, C. S. Bösinger, E. Giuffra, A. R. Holzwarth, and R. Bassi, "Time-resolved fluorescence analysis of the recombinant photosystem II antenna complex CP29," *European Journal of Biochemistry*, vol. 268, no. 2, pp. 260–267, 2001.

[187] N. Liguori, L. Roy, M. Opacic, G. Durand, and R. Croce, "Regulation of Light Harvesting in the Green Alga *Chlamydomonas reinhardtii*: The C-Terminus of LHCSR is the Knob of a Dimmer Switch.," *Journal of the American Chemical Society*, vol. 135, no. 49, p. 18339, 2013.

[188] A. A. Pascal, Z. Liu, K. Broess, B. van Oort, H. van Amerongen, C. Wang, P. Horton, B. Robert, W. Chang, and A. Ruban, "Molecular basis of photoprotection and control of photosynthetic light-harvesting," *Nature*, vol. 436, no. 7047, pp. 134–137, 2005.

[189] I. Moya, M. Silvestri, O. Vallon, G. Cinque, and R. Bassi, "Time-resolved fluorescence analysis of the photosystem II antenna proteins in detergent micelles and liposomes," *Biochemistry*, vol. 40, no. 42, pp. 12552–12561, 2001.

[190] K. Gundermann and C. Büchel, "Factors determining the fluorescence yield of fucoxanthin-chlorophyll complexes (FCP) involved in non-photochemical quenching in diatoms," *Biochimica et Biophysica Acta (BBA)-Bioenergetics*, vol. 1817, no. 7, pp. 1044–1052, 2012.

[191] C. A. Wraight and A. R. Crofts, "Energy-dependent quenching of chlorophyll a fluorescence in isolated chloroplasts," *European Journal of Biochemistry*, vol. 17, no. 2, pp. 319–327, 1970.

[192] K. Petrou, E. Belgio, and A. V. Ruban, "pH sensitivity of chlorophyll fluorescence quenching is determined by the detergent/protein ratio and the state of LHCII aggregation," *Biochimica et Biophysica Acta (BBA)-Bioenergetics*, 2013.

[193] G. Beddard and G. Porter, "Concentration quenching in chlorophyll," *Nature*, vol. 260, pp. 366–367, 1976.

[194] Y.-C. Cheng, T. K. Ahn, T. J. Avenson, D. Zigmantas, K. K. Niyogi, M. Ballottari, R. Bassi, and G. R. Fleming, "Kinetic modeling of charge-transfer quenching in the CP29 minor complex," *The Journal of Physical Chemistry B*, vol. 112, no. 42, pp. 13418–13423, 2008.

[195] E. Formaggio, G. Cinque, and R. Bassi, "Functional architecture of the major light-harvesting complex from higher plants," *Journal of Molecular Biology*, vol. 314, no. 5, pp. 1157 – 1166, 2001.

[196] D. Gust, T. A. Moore, and A. L. Moore, "Solar fuels via artificial photosynthesis," *Accounts of chemical research*, vol. 42, no. 12, pp. 1890–1898, 2009.

[197] G. D. Scholes, G. R. Fleming, A. Olaya-Castro, and R. van Grondelle, "Lessons from nature about solar light harvesting," *Nature chemistry*, vol. 3, no. 10, pp. 763–774, 2011.

[198] W. Sakamoto, "Protein degradation machineries in plastids," *Annu. Rev. Plant Biol.*, vol. 57, pp. 599–621, 2006.

[199] P. J. Nixon, F. Michoux, J. Yu, M. Boehm, and J. Komenda, "Recent advances in understanding the assembly and repair of photosystem ii," *Annals of botany*, vol. 106, no. 1, pp. 1–16, 2010.

[200] D. M. Guldi, "Fullerene–porphyrin architectures; photosynthetic antenna and reaction center models," *Chemical Society Reviews*, vol. 31, no. 1, pp. 22–36, 2002.

[201] Y. Terazono, G. Kodis, P. A. Liddell, V. Garg, T. A. Moore, A. L. Moore, and D. Gust, "Multiantenna artificial photosynthetic reaction center complex," *The Journal of Physical Chemistry B*, vol. 113, no. 20, pp. 7147–7155, 2009.

[202] V. Garg, G. Kodis, P. A. Liddell, Y. Terazono, T. A. Moore, A. L. Moore, and D. Gust, "Artificial photosynthetic reaction center with a coumarin-based antenna system," *The Journal of Physical Chemistry B*, vol. 117, no. 38, pp. 11299–11308, 2013.

[203] S. Kuhri, G. Charalambidis, P. A. Angaridis, T. Lazarides, G. Pagona, N. Tagmatarchis, A. G. Coutsolelos, and D. M. Guldi, "A new approach for the photosynthetic antennareaction center complex with a model organized around an s-triazine linker," *Chemistry A European Journal*, vol. 20, no. 7, pp. 2049–2057, 2014.

[204] R. E. Blankenship, D. M. Tiede, J. Barber, G. W. Brudvig, G. Fleming, M. Ghirardi, M. Gunner, W. Junge, D. M. Kramer, A. Melis, *et al.*, "Comparing photosynthetic and photovoltaic efficiencies and recognizing the potential for improvement," *Science*, vol. 332, no. 6031, pp. 805–809, 2011.

[205] M. Müller, P. Jahns, and A. Holzwarth, "Femtosecond transient absorption spectroscopy on the light-adaptation of living plants," *EPJ Web of Conferences*, vol. 41, p. 08006, 2013.

[206] P. D. Dahlberg, A. F. Fidler, J. R. Caram, P. D. Long, and G. S. Engel, "Energy Transfer Observed in Live Cells Using Two-Dimensional Electronic Spectroscopy," *The Journal of Physical Chemistry Letters*, vol. 4, no. 21, pp. 3636–3640, 2013.

[207] K. Amarnath, J. Zaks, S. D. Park, K. K. Niyogi, and G. R. Fleming, "Fluorescence lifetime snapshots reveal two rapidly reversible mechanisms of photoprotection in live cells of chlamydomonas reinhardtii," *Proceedings of the National Academy of Sciences*, vol. 109, no. 22, pp. 8405–8410, 2012.

[208] K. K. Niyogi, A. R. Grossman, and O. Björkman, "Arabidopsis mutants define a central role for the xanthophyll cycle in the regulation of photosynthetic energy conversion," *The Plant Cell Online*, vol. 10, no. 7, pp. 1121–1134, 1998.

[209] X.-P. Li, O. Björkman, C. Shih, A. R. Grossman, M. Rosenquist, S. Jansson, and K. K. Niyogi, "A pigment-binding protein essential for regulation of photosynthetic light harvesting," *Nature*, vol. 403, no. 6768, pp. 391–395, 2000.

[210] M. Havaux and K. K. Niyogi, "The violaxanthin cycle protects plants from photooxidative damage by more than one mechanism," *Proceedings of the National Academy of Sciences*, vol. 96, no. 15, pp. 8762–8767, 1999.

[211] T. J. Avenson, T. K. Ahn, K. K. Niyogi, M. Ballottari, R. Bassi, and G. R. Fleming, "Lutein can act as a switchable charge transfer quencher in the cp26 light-harvesting complex," *Journal of biological chemistry*, vol. 284, no. 5, pp. 2830–2835, 2009.